Université des Sciences et Technologies de Lille
Ecole Doctorale Sciences Pour l'Ingénieur

# Uni-travelling carrier photodiodes and metal mesh filters based on sub-wavelength apertures for THz applications

# THESE

présentée à l'Université des Sciences et Technologies de Lille le 16 décembre 2013

pour obtenir le titre de

## Docteur de l'Université

(Spécialité Micro et nano technologies, acoustique et télécommunication)

Par Fabio Pavanello

**Composition du jury**

| | |
|---|---|
| *Président:* | M. Gilles Dambrine |
| *Directeur de thèse:* | M. Jean-François Lampin |
| *Rapporteurs:* | M. Alfredo de Rossi |
| | M. Dries Van Thourhout |
| *Examinateurs:* | M. Cyril Renaud |
| | M. Roland Teissier |
| | M. Xavier Wallart |
| | M. Mohammed Zaknoune |

Institut d'Électronique, de Microélectronique et de Nanotechnologies – UMR 8520

 

To my family...



 

There are only two possible outcomes:
if the result confirms the hypothesis,
then you've made a measurement.
If the result is contrary to the hypothesis,
then you've made a discovery.

Ci sono soltanto due possibili conclusioni:
se il risultato conferma l'ipotesi,
allora hai appena fatto una misura.
Se il risultato è contrario alle ipotesi,
allora hai fatto una scoperta.

E. Fermi

# Acknowledgements

This work and this experience at IEMN would have not been possible without the help and the support of my parents throughout my academic path. I have learnt several things from them, especially those that are not clearly visible, but inconsciously form your character day by day. They deserve the first thanks for all of their efforts during these last 27 years...

I would like to thank Dr. Alfredo de Rossi at Thales Research and Technology and Dr. Dries Van Thourhout at Ghent University/IMEC for having accepted to evaluate this work and to provide a report of the manuscript. I would like to thank also Dr. Cyril Renaud at University College London (UCL), Dr. Roland Teissier at the Institut d'Électronique du Sud (IES) and Dr. Gilles Dambrine, Dr. Xavier Wallart and Dr. Mohammed Zaknoune all at IEMN for having accepted to evaluate this work.

I would like to thank again Dr. Xavier Wallart for having accepted me in his group and for the discussions and the fabrication, jointly with M. Christophe Coinon, of the epitaxial structures. The performances achieved in this work are with no doubt related to the high quality of the structures, from which everything starts.

I would like to thank my supervisor, Dr. Jean-François Lampin, for having accepted to supervise this work. His passion for research and his deep and spread knowledge on several fields have been an example during the whole duration of the Ph.D work. His advices and the careful reading of the manuscript have been fundamental to achieve and to valorize the results contained into it.

I would like to thank again Dr. Mohammed Zaknoune for the training in the clean-room and his long expertise on device fabrication which he kindly shared with me. The results obtained would have not been possible in any other way. Moreover, his daily good humor and our discussions, scientifical or not, especially at FT have been really helpful throughout this period.

I would like to thank Dr. Guillaume Ducournau for the several measurements performed during the whole work. His explanations of the different characterization techniques and his availability to always test devices have been a strong help to the final form of the manuscript.

I would like to thank Dr. Emilien Peytavit for the several discussions, the advices for the fabrication of the mesh filters and the development of the bench, jointly with Dr. Guillaume Ducournau and Dr. Jean-François Lampin, for measuring on-wafer photodiodes. Furthermore, I have learnt a lot from him concerning French culture and customs.

I would like to thank Dr. Mathias Vanwolleghem for the good humor he brought



 

from the Institut d'Électronique Fondamentale (IEF) in Paris or, maybe better, from the city of Gent in Belgium. Our discussions and his help with my next position have been really valuable for my future path.

I would like to immensely thank the ensemble of engineers in the clean-room and in the characterization center which helped me with their work, their trainings and their precise knowledge of the different machines and technological processes to obtain these results. I am really grateful to all of them.

I would like to thank Dr. Frédéric Garet and Ph.D student Mohan-Babu Kuppam for the measurement of the mesh filters at the University of Savoie.

I would like to thank Dr. Pascale Roy for the measurements of the mesh filters at the synchrotron source Soleil in Paris.

I would like to thank all the Ph.D students and researchers which I have met during these three years for their friendship and the time spent discussing, playing squash, volleyball or simply drinking good beers.

I would like to thank Dr. Stefano Giordano for having introduced me to the theoretical techniques for the modelization of composite materials. Even though I did not have time to treat these aspects in the manuscript, our collaboration has been particularly fruitful. The time spent developing models and applying them in multiple situations helped me understanding deeper some sub-branches of electromagnetisms.

Special thanks go to my office collegue, Philipp Latzel, with whom I have shared the MITEPHO project at IEMN. Difficult to find the words to express how his presence in the same office has influenced my work. The huge quantity of scientifical discussions ranging from quantum physics to semiconductor physics, passing through mathematics and programming have been extremely valuable for my personal growth and for the achieved results. Our international dinners have been definitely something which I will miss.

Finally, I want to address my largest thanks to the person that has changed my life the most, my future wife Jenya. Her daily presence has made my life thousand times happier than what I could barely imagine. Her incredibly contagious and constant optimism in everything has been my strongest motivation in giving the best from myself. I leave for a new experience being aware that this time, from the beginning, we will be together facing new challenges.



 

# Abstract

The increasing interest in the THz region (0.1-10 THz) for applications like imaging, spectroscopy and wireless communications is leading to a strong development of devices for the generation and detection of THz waves. Uni-travelling carrier photodiodes (UTC-PDs) are one of the main sources due to their broadband behavior (0-3 THz), room temperature operation, driving wavelength of 1.55 $\mu$m and compactness. Their main drawback comes from the low output RF powers at high frequencies (order of $\mu$W at 1 THz). A technique to increase their RF powers consists in using higher optical driving powers. However, this solution may lead to their failure because of heating, especially in case of unwanted absorption. In the first part of the thesis an electrical contact based on sub-wavelength apertures has been developed to reduce this issue. This solution has been shown valuable under multiple aspects. It provides good electrical, optical and thermal properties, while leading to an easier process in terms of fabrication and characterization with respect to previous works. A second drawback of UTC-PDs is due to their non-linear behavior which leads to a noise at low frequency because of the broad spectrum of the driving optical signals. This issue is critical for measurements at high frequencies with incoherent detectors due to the low RF powers to be detected. In the second part of the thesis a high-transparency broadband high-pass mesh filter has been developed on a novel low-loss dielectric material to filter-out this noise. The developed process can be exploited in other free-space devices like metamaterials due to the remarkable properties of this dielectric at THz frequencies.



 

# Résumé

Le grand intérêt des fréquences THz (0.1-10 THz) pour l'imagerie, la spectroscopie et les communications sans fils a conduit à un important développement de dispositifs pour la génération et la détection d'ondes THz. Les photodiodes à transport unipolaire font partie des principales sources grâce à leur comportement large bande (0-3 THz), leur fonctionnement à température ambiante, leur longueur d'opération à 1.55 $\mu$m et leur taille compacte. Le plus grand inconvénient est la leur faible puissance RF générée à haute fréquence (ordre du $\mu$W à 1 THz). Une technique pour l'augmenter consiste à utiliser des puissances optiques en entrée plus élevées. Par contre, cette solution peut conduire à leur destruction due à l'échauffement, surtout en cas d'absorption non voulue. Dans la première partie de la thèse un contact électrique basé sur un réseau sub-longueur d'onde a été développé pour réduire ce problème. Cette solution donne des bonnes propriétés électriques, optiques et thermiques avec un procédé plus simple en termes de fabrication et caractérisation par rapport aux travaux précédents. Un deuxième inconvénient est relié à leur caractère non-linéaire qui conduit à un bruit à basse fréquence à cause du large spectre des sources optiques. Ce problème est critique dans le cas de mesures à haute fréquence avec des détecteurs incohérentes car les puissances RF sont très faibles. Dans la deuxième partie de la thèse un filtre passe-haut avec une haute transparence et large bande a été développé sur un diélectrique avec faible pertes aux fréquences THz. Le procédé développé peut être utilisé pour des dispositifs en espace libre grâce aux propriétés optique du diélectrique.

# Sommario

L'interesse crescente alle frequenze THz (0.1-10 THz) per applicazioni come l'imaging, la spettroscopia e le comunicazioni senza fili sta conducendo a un forte sviluppo di dispositivi per la generazione e la rivelazione di onde a queste frequenze. I fotodiodi a trasporto unipolare sono una delle principali sorgenti grazie alla loro accordabilità su una larga banda (0-3 THz), il loro funzionamento a temperatura ambiente, la lunghezza d'onda di operazione a 1.55 $\mu$m e la loro compattezza. Il principale svantaggio é legato alle potenze RF generate (ordine del $\mu$W a 1 THz). Una tecnica per aumentarle consiste nell'adoperare potenze ottiche in ingresso più elevate. Tuttavia, questa soluzione puó portare alla loro distruzione a causa del riscaldamento, specialmente nel caso in cui vi sia dell'assorbimento della potenza ottica in altre regioni al di fuori della zona attiva. In una prima parte della tesi, un contatto elettrico basato su una matrice di aperture con dimensione inferiore alla lunghezza d'onda é stato sviluppato per ridurre l'assorbimento non voluto. Questa soluzione conduce a delle buone proprietà elettriche, ottiche e termiche utilizzando un processo di fabbricazione e caratterizzazione più semplice rispetto a lavori precedenti. Un secondo inconveniente é associato alla non-linearità del fotodiodo che puó portare ad un rumore a bassa frequenza a causa del largo spettro delle sorgenti ottiche utilizzate. Questa situazione é critica nel caso di misure ad alta frequenza con dei rivelatori incoerenti a causa delle basse potenze RF da misurare. In una seconda parte della tesi un filtro passa-alto con una trasparenza elevata e una larga banda passante é stato sviluppato su un dielettrico con basse perdite a frequenze THz. Il processo sviluppato puó essere utilizzato per dei dispositivi free-space grazie alle proprietà ottiche del dielettrico.



 

# Introduction

Different approaches exist to generate electromagnetic radiation in the range 0.1 - 10 THz commonly defined as the THz region. Several applications have shown a strong interest at these frequencies like imaging, spectroscopy and wireless communications. However, there is still no compact, tunable, easy to modulate and powerful source operating at room temperature (RT) able to cover this region.

In the optical approach, the main limitation is associated with the difficulty to have a stable, tunable, low energy transition. The main reason comes from the fact that is extremely difficult to freely tune optical sources due to the discrete character of the optical transitions in simple quantum structures (atoms, molecules...). Another reason is associated to the thermal disorder of the system which makes very difficult to achieve lasing operation. At RT the thermal energy is represented by a value of around 25 meV, quite high compared to the energies associated to the region of interest (1 THz corresponds to 4.1 meV). Some techniques can be employed to partially get rid of these problems like operating at lower temperatures or using engineered transitions. On the other side, in the electronic approach, the main problems arise from carrier transit times inside semiconductor devices and from capacitive effects, intrinsic in the operation of devices. The shrinkage of the dimensions in semiconductor technology has brought to the possibility of reducing these effects using ballistic transport phenomena and lowering the capacitances.

In order to overcome some of these problems a mixing of the two approaches has been exploited. In fact, the coupling of the optical properties of semiconductors within electronic devices has led to a new approach belonging to the so-called world of optoelectronics. In particular, uni-travelling carrier photodiodes (UTC-PDs), a modified version of the more common p-i-n PDs, have shown a strong potential due to their broadband character (0-3 THz), RT operation, driving wavelength at 1.55 $\mu$m and compactness. The broadband character is fundamental in applications like spectroscopy to achieve high spectral purity or wireless communications to have a large modulation bandwidth (higher bit data rates). Operation at RT is very important in practical industrial applications rather than in laboratory environments where cryogenic bulky systems can be afford. Moreover, the availability of well-developed fibered devices at 1.55 $\mu$m for telecommunications like laser sources, amplifiers and modulators makes their integration with UTC-PDs easier.

However, a first drawback of these devices is their low RF generated powers, especially above 1 THz (order of $\mu$W). Far from the saturation, a simple solution consists in increasing the optical driving power achieving higher photocurrents and consequent higher RF output powers. Nonetheless, a crucial issue that has to be taken into account is the thermal heating, in particular for back-side illumination and small device areas due to unwanted optical absorption in metal contacts. This effect may lead to the failure of the device, even far from the saturation, as already observed in previous Ph.D work on UTC-PDs. To improve this aspect an electrical contact based on sub-wavelength apertures has been developed. This approach has been proven valuable from the electrical, optical and thermal point of view, while simplifying the fabrication process and enabling their "on-wafer" characterization. A second drawback of UTC-PDs is intrinsic in their operating principle which exploits the non-linearity (with respect to the electric field) of the absorption in semiconductors. However, at high frequencies (low RF powers) and for incoherent detectors, a low frequency background noise related to the non-zero linewidth of the driving sources may be comparable to the RF signal to be detected. To partially get rid of this noise, a high-pass mesh filter has been conceived with high transparency over a large band of frequencies above 1.5 THz.

The thesis is structured in four chapters and followed by a conclusions and perspectives section. The first chapter will provide an introduction to PDs and UTC-PDs, an overview of their state-of-the-art and of the other sources working in the THz region. The second and third chapters will be addressed to the first problem introduced above. In particular, the second chapter will show that back-side illumination cannot be efficiently exploited (for high cut-off frequencies) to solve this problem and that a front-side configuration has to be adopted. A treatment of sub-wavelength apertures based on the coupled mode theory will be introduced and quasi-analytical calculations supported by complementary finite element simulations will be used to design the top-contact of UTC-PDs. In the third chapter the fabrication process, the characterization and the analysis of the measurements will be illustrated. The fourth chapter is addressed to the second presented drawback of UTC-PDs. It will report the design, fabrication and characterization of the mesh filter. In particular, it will be shown that the conceived process may be employed for a wide wariety of free-space devices like metamaterials or photonic band gap structures thanks to the possibility of cascading multiple elements in 2.5D structures and to the remarkable properties of the dielectric material used at THz frequencies.

# Contents

# Chapter 1

# High-speed photodiodes as valuable THz sources

In what follows, the physics of p-n and p-i-n photodiodes (PDs) will be briefly recalled. Then, uni-travelling carrier PDs (UTC-PDs) will be introduced by showing their state of the art within the THz community and the work performed previously within the EPIPHY/THz photonics group at IEMN as the starting point of this thesis. Finally, a short survey of other THz sources will be presented mentioning their main advantages and disadvantages.

## 1.1 Semiconductor junctions as photodetectors

The basic concepts of p-n and p-i-n PDs will be given here. Some useful notations will be introduced and the main aspects that have to be taken into consideration for the design of PDs will be given. The provided knowledge will be useful in the next section to better understand the behavior of UTC-PDs. At the end, in a straightforward way the main reasons that brought to the invention of UTC-PDs will be explained.

### 1.1.1 Basic principles of p-n and p-i-n photodiodes

The p-n junction, discovered as an alternating current rectifier by Ohl at Bell labs in 1939, has been promptly indicated by the same Ohl as a light-sensitive electric device and considered as the first solar cell prototype [1, 2]. It is essentially composed by a p-type and an n-type semiconductors in physical contact. Here, for simplicity a homojunction is considered (same semiconductor materials) in GaAs. However, similar conclusions would be obtained in the case of a heterojunction with some differences that will be discussed further on. The choice of using GaAs in this introductory part is dictated by its properties and by its relative simplicity and similarity with the active material used in UTC-PDs. The band diagrams and electric fields reported in this thesis are computed by Nextnano++, a simulation software that calculates quantum-mechanically the band structure of the materials and then applies drift-diffusion and Poisson equations to the system to obtain the electric potential and other useful parameters that will be introduced later on [3].

Once a p-type and an n-type semiconductors are in physical contact, a flux of carriers is established at their interface due to a different chemical potential (i.e. different carrier concentrations in sign and/or value) to bring the system at the thermodynamical equilibrium. The equilibrium is reached when the quasi-Fermi levels $E_{F_p}$ and $E_{F_n}$ of the p-type and n-type regions respectively are aligned as schematically represented in Fig.1.1 where the band diagram and the electric field normal to the junction interface are depicted. The vacuum level $E_0$ before the contact is at the same level in both the semiconductors due to the sharing of the same environment, while after the contact $E_0$ follows the profile of the conduction band (CB) and valence band (VB) in order to keep constant the electronic affinity $q\chi$ proper of each semiconductor. This equilibrium is achieved thanks to a redistribution of the charges within the structure, in particular at the interface a depleted region (width of 10-100 nm) is created, meaning that a net charge consisting of ion impurities is present, whereas far from the interface the p-type and n-type regions are neutral. The net charge flow has the effect of establishing a built-in electric field (order of tens of kV/cm) and a potential barrier $V_{bi}$ to achieve a dynamic equilibrium at the interface. This electric field can be used to separate charges of different signs and to accelerate them towards the respective p-type and n-type regions depending on their nature. Electron-hole pairs can be created by EM radiation absorption at the condition that the energy of the radiation is larger than the energy gap $E_g$ of the semiconductor. This is the only theoretical limitation to obtain a photocurrent at the ohmic contacts of the PD. However, technological constraints associated to the choice of the materials and to their fabrication processes can limit the efficiency and they have to be taken into consideration.

#### 1.1.1.1 Efficient absorption in photodiodes

In order to have an efficient absorption process at energies just above $E_g$, it is imperative to have a semiconductor with a direct band gap. This means that the top of VB and the bottom of CB coincide in the k-vector space. This requirement is fundamental because in



 

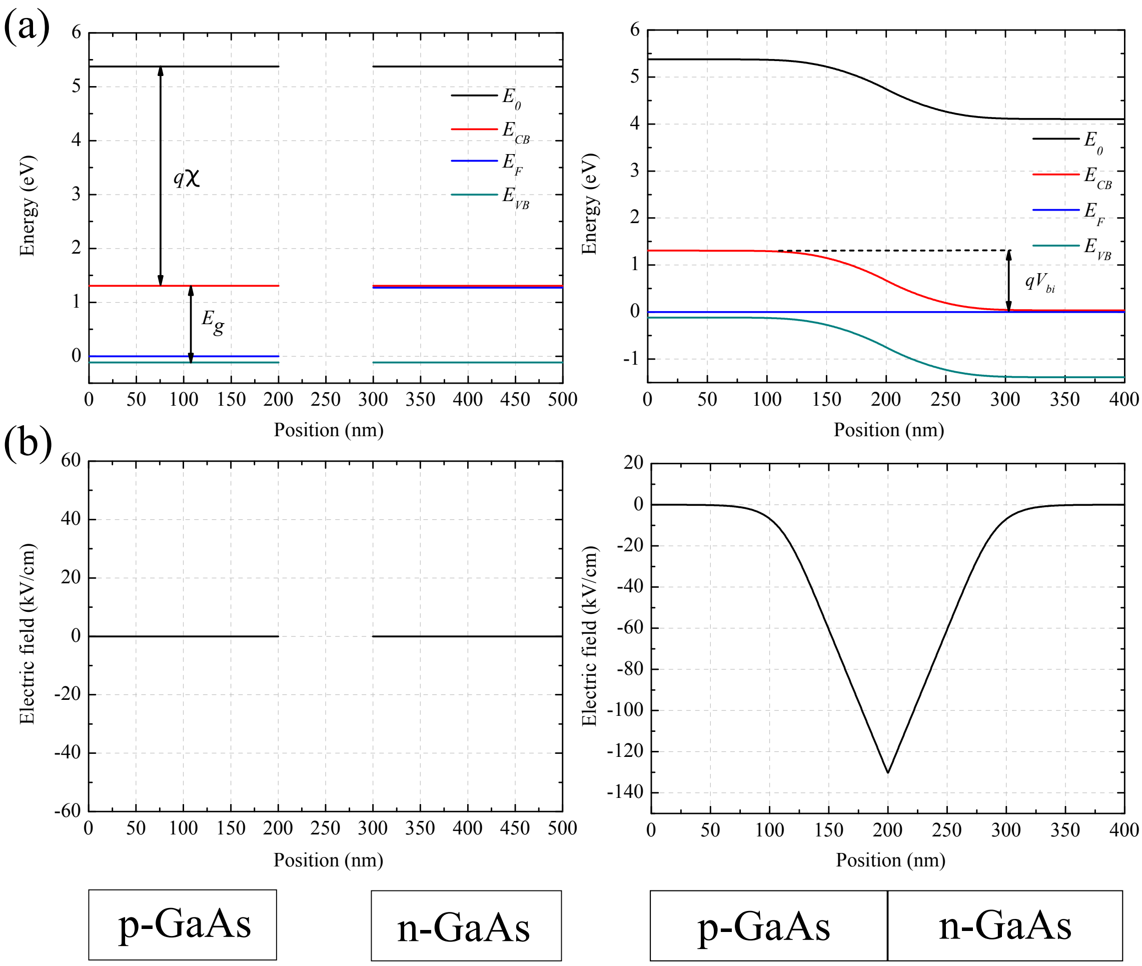


Fig. 1.1: (a) Band diagram and (b) electric field before and after contact of a p-GaAs and n-GaAs layers with doping concentration of $10^{17}$ cm$^{-3}$.

an absorption process, schematically represented in Fig.1.2, the photon carries a momentum $k = 2\pi/\lambda$, with $\lambda$ the photon wavelength, that is negligible compared to the lattice phonon momentum (in the order of $\pm\pi/a$ with $a$ the lattice constant)[4]. The probability of absorption is much higher for a direct band gap material than for an indirect band gap one at energies just above their respective $E_g$ due to the fact that the momentum conservation is preserved in the first case without the need of an intermediate particle in the process like a phonon [4]. Secondly, the crystalline quality of the semiconductors is a key issue because defects reduce the efficiency of the PD and shorten the average lifetime before recombination (carrier lifetime) decreasing the collection efficiency at the metallic contacts [5]. This second consideration is always valid in DC or low-frequency operation mode, while at high frequencies (compared to the device frequency response neglecting carrier lifetime) it can be more useful to avoid long recombination times by locally introducing defects to reduce the response delay of the device and increase its frequency range of operation as it will be seen below. The condition of thermodynamical equilibrium can

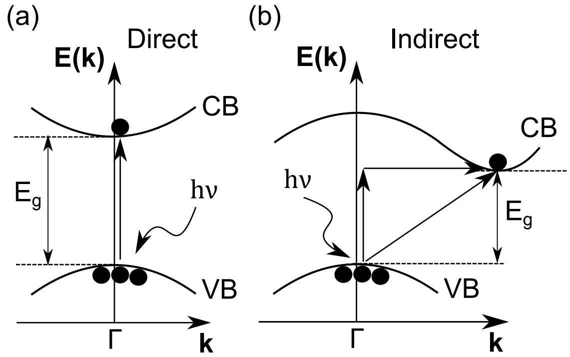


Fig. 1.2: Absorption processes for a direct and an indirect band gap materials.

be broken (apart from photogenerating carriers) by the application of a voltage at one of the PD's ohmic contacts. In particular, a negative applied voltage at the p-side increases the potential barrier resulting in a higher electric field, while a positive applied voltage at the p-side decreases the barrier and results in a lower electric field. This behavior is macroscopically represented by the static response of a photodiode represented in Fig. 1.3 and described by

$$I = I_S(e^{qV/k_BT} - 1) - I_{ph} \tag{1.1}$$

where $I_S$ is the reverse-bias saturation current or dark current, $q$ is the elementary charge ($1.6 \cdot 10^{-19}$ C), $k_B$ is the Boltzmann constant ($1.38 \cdot 10^{-23}$ J/K), $T$ is the temperature in Kelvin and $I_{ph}$ is the generated photocurrent.

One of the main parameters of PDs is the external quantum efficiency that indicates how efficiently the photons energy is converted in electrical current and it is given by [5]

$$\eta_{ext} = \frac{I_{ph}}{q}\frac{h\nu}{P_{opt}} \tag{1.2}$$

where $P_{opt}$ is the impinging power (also called optical power due to its frequency usually close to the light frequency range) and $h\nu$ is the photon energy with $h$ the Planck constant ($6.62 \cdot 10^{-34}$ J·s) and $\nu$ the photon frequency. $I_{ph}$ depends principally on the absorption constant $\alpha(\nu)$ of the semiconductor and the width $w$ of the absorption region. It is worth to notice that, at equivalent $\alpha(\nu)$, technological characteristics, photo-carriers response and $P_{opt}$, the efficiency will be higher for a PD working with a smaller $E_g$ due to a higher

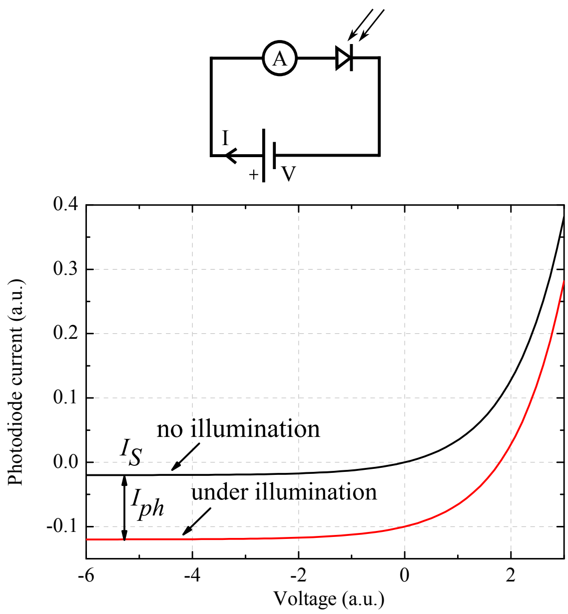


Fig. 1.3: Static I-V characteristic of a photodiode with no illumination (dark condition) and under illumination. Above the graph is illustrated the notation for the current and voltage signs.

number of photons impinging at constant $P_{opt}$. A quantity which is more used in practical applications is the responsivity $R$ measured in A/W. This quantity is connected to the external quantum efficiency by

$$R = \frac{I_{ph}}{P_{opt}} = \eta_{ext}\frac{q}{h\nu} \tag{1.3}$$

Eq. 1.3 takes into account not only how efficiently the process of carriers photogeneration and collection happens, but also how much energy is involved in the process. In particular, by considering two devices with same $\eta_{ext}$, the one operating at a larger wavelength will achieve higher photocurrents. Another parameter which is related to the external quantum efficiency is the internal quantum efficiency $\eta_{int}$ that indicates how efficiently the absorbed light in the semiconductor is converted into current and it is related to $\eta_{ext}$ in the following way

$$\eta_{int} = \frac{\eta_{ext}}{(1-R)(1-e^{-\alpha(\nu)w})} \tag{1.4}$$

where $(1-R)$ represents the transmitted optical power with $R$ the reflection coefficient at the PD surface and $(1-e^{-\alpha(\nu)w})$ the fraction of absorbed power according to the Lambert-Beer law [6]. In the case of GaAs (direct band gap), the absorption coefficient $\alpha(E = h\nu = 1.43\text{ eV})$ is $\approx 10^4$ cm$^{-1}$ and thus the ideal depletion region width $d$ would be



 

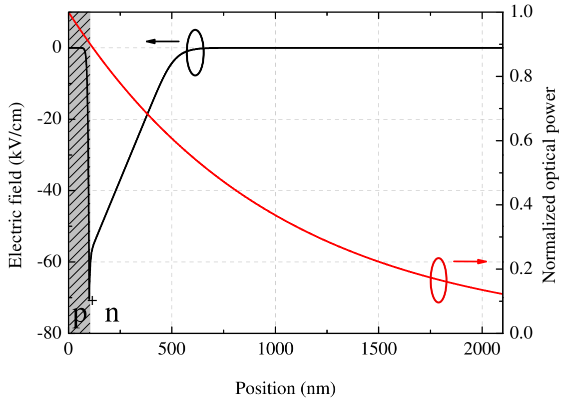


Fig. 1.4: The electric field and the decay of the normalized optical power $P_{opt}$ within the p$^+$-n abrupt junction. The GaAs homojunction presents a p$^+$-type region doped at $10^{18}$ cm$^{-3}$ (shaded) and an n-type region doped at $10^{16}$ cm$^{-3}$. An absorption $\alpha$ = $10^4$ cm$^{-1}$ has been used to plot $P_{opt}(x)/P_{opt}(0) = e^{-\alpha x}$.

of around 2-3 $\mu$m. However, in the p-n junction above, $d$ is nearly 200 nm and, under the depletion approximation (no free carriers in the depletion region and an abrupt fall of the net charge outside of it), it is given by [5]

$$d = \sqrt{\frac{2\epsilon_s}{q}\frac{N_a + N_d}{N_a N_d}(V_{bi} - V_a)} \tag{1.5}$$

where $\epsilon_s$ is the semiconductor permittivity, $N_a$ and $N_d$ are the doping concentrations of the p-type and n-type regions and $V_a$ is the applied voltage refered to the p-contact. From Eq. (1.5) it can be observed that $d$ can be increased using lower doping levels or by applying a higher reverse voltage. The drawback of decreasing the doping levels is mainly associated to the specific contact resistance $\rho_c$ (in units of $\Omega$m$^2$) at the interface metal/semiconductor defined as $\left(\frac{\partial V}{\partial J}\right)_{V=0}$ with $J$ the current density in $A$/m$^2$. Low doping levels increase $\rho_c$ and can lead to a non-ohmic behavior depending on the chosen metal for the contact [5]. An asymmetry in the doping levels is sufficient to increase $d$ (see Eq. 1.5) and to have a low $\rho_c$ for both the regions. For example, in the case of GaAs, it is possible to have maximal p-type doping levels ($N_a \approx 10^{20}$ cm$^{-3}$) higher than n-type ones ($N_d \approx 10^{18} - 10^{19}$ cm$^{-3}$) to achieve a low $\rho_c$ (order of $10^{-7}$ $\Omega$cm$^2$) [7]. However, the reduction of the doping level is not sufficient to cover the whole absorption region due to a minimal doping ($10^{16}$ - $10^{17}$ cm$^{-3}$) to have a low $\rho_c$ and thus, photocarriers will be generated outside the depletion region and minoritary photo-carriers will diffuse into the depletion region and then accelerate towards the metallic contacts. The carriers diffusion coefficient is one of the most important issues for the response speed of homojunction PDs and it is related to their mobility by the Einstein relations [5]

$$D_{e,h} = \frac{\mu_{e,h} k_B T}{q} \tag{1.6}$$

where $D_{e,h}$ and $\mu_{e,h}$ are the diffusion and the mobility coefficients of electrons/holes. Generally, for III-V semiconductors, the mobility of electrons is much larger than that one of holes and so, in terms of efficiency and response speed, it is more favorable to have higher optical power and consequent photogeneration in regions (Fig. 1.4 shaded) where the electrons are minoritary as they diffuse faster than minoritary holes in the opposite region [8]. In the case of GaAs, the mobility of minoritary electrons in a p-doped matrix at $10^{17}$ cm$^{-3}$ is nearly 2000 cm$^2$V$^{-1}$s$^{-1}$, while for minoritary holes in an n-doped matrix at $10^{17}$ cm$^{-3}$ is roughly 100 cm$^2$V$^{-1}$s$^{-1}$ [9]. Such a low value for the diffusion coefficient (minoritary holes) underline that it is essential to avoid this phenomenon, particularly holes diffusion, in the device for high-speed operation. A good solution seems to be a structure with a highly p-doped region and a slightly n-doped one (p$^+$-n) in fact, as it can be seen in Fig. 1.4, the depletion width can be increased to around 500 nm using different doping levels, while the asymmetry guarantees a low specific contact resistance for the p-type and n-type regions and, at the same time, a better diffusion of the photo-carriers generated in the p$^+$-type region. The structure in Fig. 1.4 is quite large compared to the depletion width to underline the decay of the optical power and the impossibility of covering the whole absorption region. In reality, this structure would be reduced to a width of 600-700 nm to avoid the creation of holes within the n-type region improving

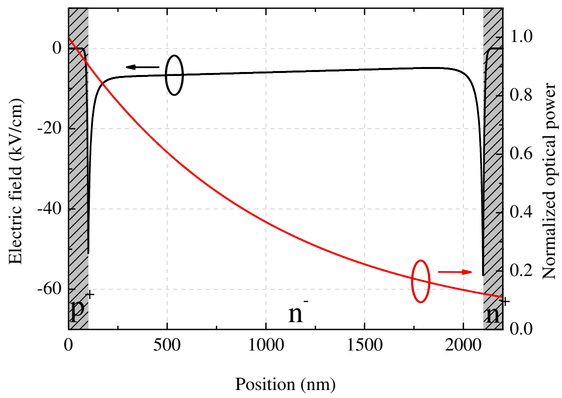


Fig. 1.5: The electric field and the decay of the normalized optical power $P_{opt}$ within the p-i-n junction. The GaAs homojunction presents a p$^+$-type region doped at $10^{18}$ cm$^{-3}$ (shaded), an nid region with n-type concentration of $10^{15}$ cm$^{-3}$ an n$^+$-type region doped at $10^{18}$ cm$^{-3}$ (shaded). The red curve is equivalent to the curve for the p$^+$-n junction of Fig. 1.4.



 

the response speed, but decreasing the responsivity. The kink in the electric field at the junction interface is due to the presence of free carriers (holes) within the depletion region (for high differences in doping levels the depletion approximation is no more valid).

For what concerns the increase of the depletion width by a reverse applied voltage, the main problem comes from the junction breakdown due to avalanche and/or tunneling effects for values higher than the critical electric field depending on the impurities concentration and the material. For GaAs doped at $10^{17}$ cm$^{-3}$ the critical electric field is roughly $7 \cdot 10^5$ V/cm [5].

The p$^+$-n structure presents obvious limitations related to the correlation between depletion and absorption regions. In fact, it is fundamental to dope the n-type region to have a low $\rho_c$ but, even using a low doping level ($10^{16}$ cm$^{-3}$), it is not possible to make the depletion region covering the absorption one. A solution proposed by J. Nishizawa *et al.* in 1950 is to modify the initial p-n structure by adding an intrinsic region sandwiched between the p-type and n-type regions, here for simplicity of the same material of the doped regions [10]. Due to the intrinsic or, in reality, very low doping level ($10^{14} - 10^{15}$ cm$^{-3}$) called also non intentionally doped (nid) level, the intrinsic region will be completely depleted. In this case, $N_a$ and $N_d$ can be kept high ($10^{18} - 10^{19}$ cm$^{-3}$) to have a low series resistance, a low $\rho_c$ and a high electric field in the intrinsic region. In Fig. 1.5 the electric field and the decay of the normalized optical power for a p-i-n structure in GaAs are represented. An intrisic region can increase $d$ of nearly its width and thus, for identical doping concentrations, it can be larger than for a p-n junction. It is important to notice that impurities cannot be freely introduced within the semiconductor matrix and thus, above a certain doping level threshold, a further increase of $d$ will have as a consequence a decrease of the built-in electric field. A thicker depleted region can be used not only to increase the absorption within the device, but also to improve (for proper design parameters) the device response speed as it will be shown below. Such a structure still presents the absorption of carriers within the highly doped regions and, even if they have been reduced compared to the previous structure, they remain a limitation for the device response.

#### 1.1.1.2 The InP/InGaAs system for 1.55 $\mu$m wavelength

The previous issue can be solved by having a look to the graph in Fig. 1.6 that shows how the composition of ternary materials affects $E_g$ and the lattice constant $a$. Devices like PDs, as already said above, need to have extremely high crystalline quality in order to reduce defects leading to non-radiative recombinations. Such a quality is related to several parameters, but the most important one is certainly the lattice constant of a material. Through the theory of elesticity applied to periodic structures as semiconductors

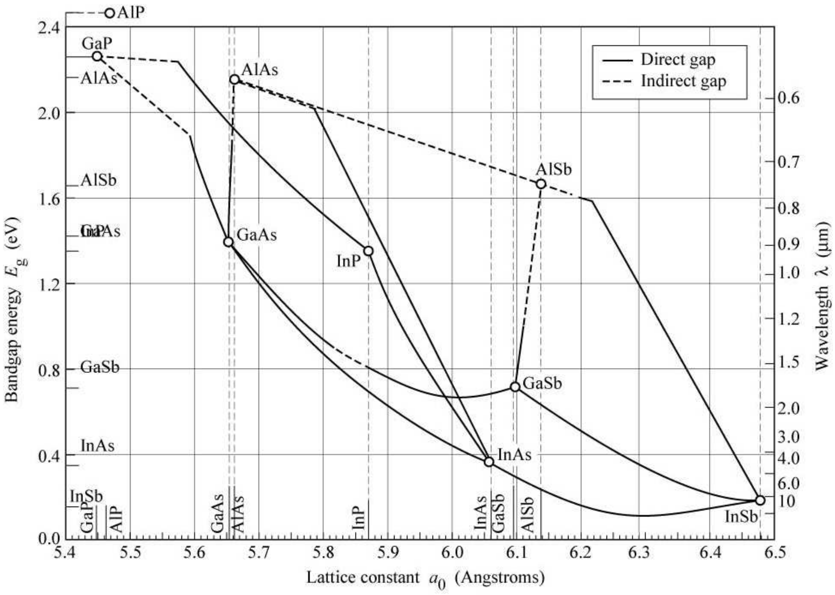


Fig. 1.6: $E_g$ vs lattice constant for the principal III-V semiconductors and related alloys, from Ref. [11].

are, it is possible to define a parameter called the critical thickness $t_{crit}$ that represents the maximal thickness to which a certain material can be grown on top of another in a strained situation. Above this value the grown material relaxes introducing defects like dislocations within the structure and reducing the overall crystalline quality. In case the grown material has the same $a$ of the underneath material, then $t_{crit}$ theoretically tends to infinity, while if the latter is different then a trade-off has to be found by taking into account the lattice mismatch. As it can be observed in Fig. 1.6 there exist some combinations of semiconductors that are suitable to be grown lattice-matched (LM). For ex. InP/$In_{0.53}Ga_{0.47}As$ is one of the most used heterostructures due to the fact that it can be grown using InP as substrate (which is one of the most conventional substrate material for photonic devices at 1.55 $\mu$m thanks to its high crystalline quality) and to the fact that it satisfies the LM condition [12]. Moreover, $In_{0.53}Ga_{0.47}As$ (or equivalently LM-InGaAs) has an $E_g = 0.75$ eV and a direct band gap (see Fig. 1.6) and this is technologically relevant because it absorbs at 1.55 $\mu$m (0.8 eV) that corresponds to the wavelength associated to the third window of optical fibers. This window is the most transparent one for fiber-guided signal propagation (attenuation less than 0.3 dB/km) and it is also refered as the telecom window due to its wide-spread use in telecommunications. Due to these properties of the InGaAs/InP system, a huge variety of components have been developed like lasers, amplifiers, polarizers, beam splitters, isolators or circulators working at 1.55 $\mu$m. The band diagram for a p-i-n structure based on this system is reported in Fig. 1.7. The main differences with respect to the previous GaAs homojunction are the fact that in this case there is no more absorption at the excitation wavelength (1.55 $\mu$m) in the undepleted regions thanks to heterojunctions and that there are CB and VB discontinuities at the borders of the depleted region. These discontinuities can be a limiting factor under certain conditions because they can act as traps for the carriers depending on their kinetical energy [13].

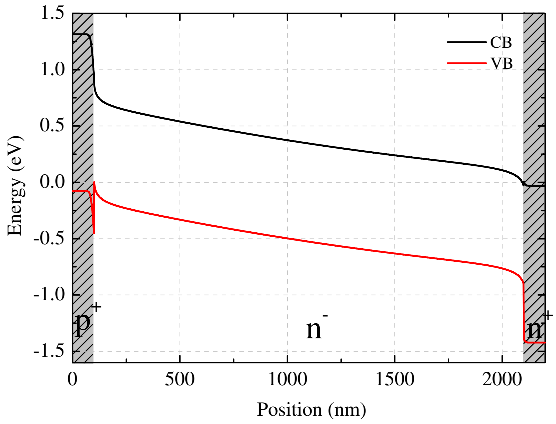


Fig. 1.7: Band diagram of a p-i-n heterojunction with same dimensions and doping levels as before, but p+ and n+ layers in InP (shaded) and intrinsic layer in $In_{0.53}Ga_{0.47}As$. The discontinuities of CB/VB at the p+/i (n+/i) interfaces act as barriers for the electrons (holes).

### 1.1.2 Response speed of p-n and p-i-n photodiodes

The equivalent circuit of a PD charged over a load without any packaging (no further capacitance) and bonding wires (no further resistance and inductance) is schematically represented in Fig. 1.8. The PD can be modeled as a current generator with a resistor and a capacitor in parallel modeling an intrinsic resistance $R_i$ and an intrinsic capacitance $C_i$ proper of the junction (depleted region) and two resistors in series modeling the resistance $R_S$ of the undepleted regions of the PD plus contact resistances ($\rho_c^{n,p}/\Sigma$ with $\Sigma$ the PD area) and a load resistance $R_L$. $R_i$ and $C_i$ are voltage-dependent and $R_i$ is usually in the order of 1-100 M$\Omega$ in the photoconductive mode (negative bias region according to the convention of Fig. 1.3) and can be neglected, while $C_i$ has to be taken into account and, in the photoconductive mode (no diffusion capacitance) under the depletion approximation,



 

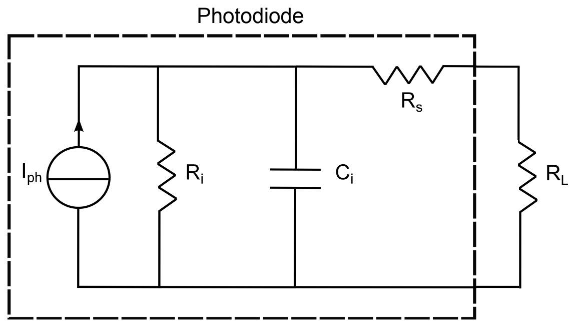


Fig. 1.8: Equivalent circuit model of a PD charged over a load $R_L$ without packaging.

is given by [5]

$$C_j = \frac{\epsilon_s \Sigma}{d} \tag{1.7}$$

Here, it can be observed that the capacitance can be decreased in the case of a p-i-n structure by comparison of Fig. 1.4 and 1.5. Even though Eq. 1.7 is only valid under the depletion approximation, it gives a good approximated value of $C_j$ for the structures discussed before. The response speed of PDs is limited by two main factors: the $RC$ charge time and the transit time $\tau_t^{e,h}$ of the carriers within the depleted region. These two limiting factors are common to many other devices like transistors, Schottky diodes, photoconductors etc. [5]. Regarding the first factor, the p-i-n structure is with no doubt superior to the p$^+$-n one in fact, recalling that for the p$^+$-n structure above $d \approx 500$ nm and for the p-i-n one $d = 2$ $\mu$m, it can be adfirmed that $C_j$ will be roughly four times higher for the abrupt junction compared to the p-i-n structure at same $\Sigma$. However, this decrease in $C_j$ is at the expenses of a higher $\tau_t^{e,h}$ given by [4]

$$\tau_t^{e,h} = \frac{v_{e/h}(F)}{d} \tag{1.8}$$

where $v_{e/h}(F)$ are the electron/hole velocities depending on the electric field $F$ within the depleted region. Here, devices with a cylindrical symmetry around the normal to the junction interface are being considered and thus $F$ coincides with the axial and sole component of the electric field ($F = \|\mathbf{F}\|$). The velocity of electrons and holes are largely different in semiconductors for low fields (order of kV/cm), in fact $v_{e/h}(F) = \mu_{e/h}(F)F$ with $\mu_{e/h}(F)$ the mobilities of electrons/holes depending on $F$ [4]. In the semi-classical model of the transport $\mu_{e/h}(F)$ is given by [4]

$$\mu_{e/h}(F) = q\frac{\tau(F)}{m^*_{e/h}(F)} \tag{1.9}$$

where $\tau(F)$ is the average scattering time between two collision processes and $m^*_{e/h}(F)$ is the effective mass related to the band structure of the semiconductor, both depending on



 

$F$ (the * is used to indicate that these parameters have to be calculated considering the band structure of the semiconductor). In particular, for high electric fields the velocity does not increase anymore and, depending on the material, it can even decrease showing a differential negative mobility. This effect can be observed in Fig. 1.9 where the electron velocity reaches a maximum for GaAs and it decreases saturating for higher fields to a value of nearly $10^7$ cm/s. The reason for this decrease is related to the band structure of GaAs, in fact due to the availability of other valleys in CB, the carriers that acquire sufficient energy can be transferred to other valleys with a different $m_e^*$. The saturation

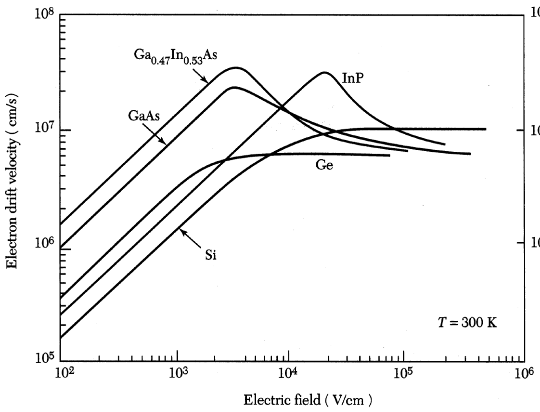


Fig. 1.9: Electron drift velocity as a function of the electric field for several semiconductors, from Ref. [5].

of the velocity is instead associated to the scattering within the lattice and the impurities modeled by $\tau(F)$. Even though electrons can attain with relatively low fields (3-3.5 kV/cm for GaAs) high velocities due to their low effective mass ($m_e^* = 0.063\ m_0$ with the electron mass $m_0 = 9.1 \cdot 10^{-31}$ kg for GaAs), holes have a much larger effective mass ($m_h^* = 0.51$ $m_0$ for heavy holes in GaAs) and their saturation velocity ($10^7$ cm/s) is reached for electric fields of 50-60 kV/cm [14]. Thus, it is important to have a high electric field in the depleted region to reduce $\tau_t^h$ by operating in the photoconductive mode or by choosing large doping level differences. The relative RF output power for a wide-band p-i-n PD illuminated far from the saturation by a modulated signal at a frequency $f$ can be described as [15]

$$P_{rel}(\nu) = \frac{1}{(1 + (\frac{\nu}{BW_{RC}})^2)(1 + (\frac{\nu}{BW_{TR}})^2)} \tag{1.10}$$

where $BW_{RC} = \frac{1}{2\pi RC}$ and $BW_{TR} \approx \frac{3.5}{2\pi\tau_t^h}$ are the charge and transit time related bandwidths [15]. For the p-i-n InP/InGaAs-based structure considered before, $BW_{RC} = 517$ GHz for an active area $\Sigma = 100\ \mu\text{m}^2$, an overall resistance of 50 $\Omega$ and a static relative permittivity of $In_{0.53}Ga_{0.47}As$ equal to 13.94 [8]. This high value of $BW_{RC}$ is due to the fact that the thickness of the depleted region is $d = 2$ $\mu$m to wholly absorb the impinging optical power. However, $BW_{TR} \approx 3.3$ GHz using a hole saturation velocity for slightly n-doped $In_{0.53}Ga_{0.47}As$ at room temperature (RT) estimated at $4.8{\cdot}10^6$ cm/s above 54 kV/cm [16] and considering to have an applied voltage sufficient to have such electric field. These simple calculations bring to the conclusion that $d$ has to be reduced to optimize the response speed of p-i-n PDs. This choice has the following implications:

- It is not possible to absorb the whole optical power in one trip, but some strategies can be used to partially overcome this drawback.
- The capacitance increases, but the diode surface could be reduced to compensate for it being aware that the optical power density will be higher to keep the same external efficiency.
- The electric field in the intrinsic region is higher, thus permitting to apply lower bias levels.

However, the design freedom degrees are strongly limited by the fact that $d$ has to be reduced affecting both $BW_{RC}$ and $\eta_{ext}$ and, even having $d = 100$ nm and saturation velocity for holes, $BW_{TR} = 264$ GHz, but $BW_{RC}$ has been reduced by a factor 20 and the absorbed $P_{opt}$ to 10%. Furthermore, high values of the electric field cannot be maintained within the depletion region due to carriers accumulation and consequent saturation as it will be explained better in the next subsection. So far, all the reasonings have been done by considering a vertical (compared to the epitaxial structure direction of growth) illumination, though p-i-n guided structures can be exploited to remove the restriction on the responsivity and the thickness of the depletion region. However, other issues arise related to the area of the structures (which contributes to the capacitance), to the illumination ease, to the fabrication etc. These structures will be discussed later on in the state-of-the-art section underlining their principal advantages and disadvantages.

### 1.1.3 Limitations of the p-i-n structure

P-i-n PDs have been introduced to obtain a faster response that means for ex. to be able to follow a modulated optical signal at higher frequencies without smoothing of the signal. Practically, this turns out to be processing larger amounts of data in a telecommunication system. They show also a better $\eta_{ext}$ due to their larger absorption width $w$ compared to $p^+$-n and p-n junctions. However, holes response is largely slower than electrons one due to their different effective masses and, even though holes can reach high saturation velocities, they need high electric fields for it. From these considerations it looks quite inefficient to provide further energy to the system under the application of a bias, because as already seen electrons do not increase their velocity, but dissipate the acquired energy from the electric field by scattering and thus heating the device. As seen in the previous subsection, the depletion region cannot be decreased without an increase of the capacitance, thus affecting negatively $BW_{RC}$ and $\eta_{ext}$. Moreover, p-i-n PDs have a relatively low saturation threshold that arises mainly from space charge effects due to the fact that, once the pairs are separated in the depletion region, the positive and negative clouds tend to attract eachother and to create an electric field that screens the starting built-in electric field and leads to an accumulation of the photo-carriers in the depletion region which brings the PD in a saturation mode [17, 18]. Such a phenomenon can be observed in Fig. 1.10 where the simulated electric field and corresponding charge carrier densities are plotted for a p-i-n InP/InGaAs based PD. The electric field reduces considerably due to the space charge effect and leads to an accumulation of the carriers at the borders of the intrinsic region. It is then highly important under drift transport conditions to have carriers with high mobilities for relatively low electric fields to be able to separate them as fast as possible. This issue is associated to the intrinsic operation of all PDs, but the coincidence of the

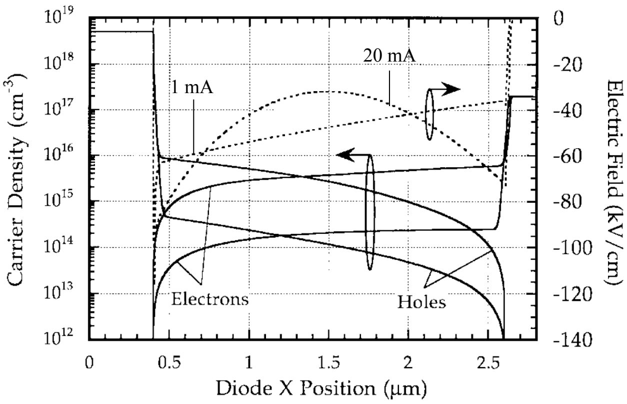


Fig. 1.10: Electric field and charge carrier densities of a p-i-n PD 2.2-$\mu$m-long under different non-modulated illuminations and photocurrents of 1 (lower electrons and holes curves) and 20 mA (upper electrons and holes curves) with a bias of -10 V, from Ref. [17].

absorption and acceleration regions with consequent contribution of the holes to the drift current leads to a low saturation threshold. In the next section a structure that partially gets rid of these problems by exploiting two separated regions for the absorption and the acceleration overcoming the inertia of holes and reaching higher saturation values will be presented.

## 1.2 A different approach: the uni-travelling carrier photodiode

In this section an approach to improve the response time of PDs will be illustrated and a few techniques will be shown to use them not just for the detection, but also for the generation of radiation from DC to a few THz. Finally, the state-of-the-art regarding the THz generation by PDs will be presented within the THz community and the EPIPHY/THz photonics group at IEMN.

### 1.2.1 Epitaxial structure and suitable materials

In order to overcome the major problem in the response speed of p-i-n structures i.e. the response of holes, it is necessary to avoid their drift within the depleted region. This means that they have to be created in a region where their response is collective like the one of electrons in a metal. Such a mechanism can be achieved by strongly p-type doping a region which will correspond to the absorbing one of the previous cases. However, as it has been seen before, a heavily doped region does not allow a high electric field to be established in. This means that electrons will reply within a diffusion time in this region and then they will be accelerated as usual in a collection region. These considerations are at the basis of the uni-travelling carrier PDs invented at NTT laboratories (Japan) by Ishibashi and co-workers in 1996 [19]. In Fig. 1.11 the proposed structure based on the InP/InGaAs system by Ishibashi and co-workers is reported. The photo-generation takes place in the region called light absorption layer that is heavily p-type doped (around $10^{18}$ $cm^{-3}$) InGaAs (close to the LM condition to InP). This layer can present a gradient in doping or composition in order to enable a quasi-electric field in it. As already said, the holes will respond in a collective way and will diffuse towards the diffusion barrier layer and then collected at the metallic contact (dashed layer). The diffusion barrier is introduced to avoid electrons to diffuse towards the p-type contact and is based on p-type doped ($10^{18}$-$10^{19}$ $cm^{-3}$) $In_{0.73}Ga_{0.27}As_{0.6}P_{0.4}$ (or other high $E_g$ quaternary material combinations) LM to InP. The carrier collecting layer has the function to accelerate the electrons towards the n-type contact and is based on nid InP to achieve high electric fields thanks to its depleted nature once in contact with the light absorption layer. Due to its low doping, it is necessary to insert a heavily n-type doped ($10^{18}$-$10^{19}$ $cm^{-3}$) InP layer (right-handed black layer) next to it to achieve a low contact resistance at the interface with the metallic



 

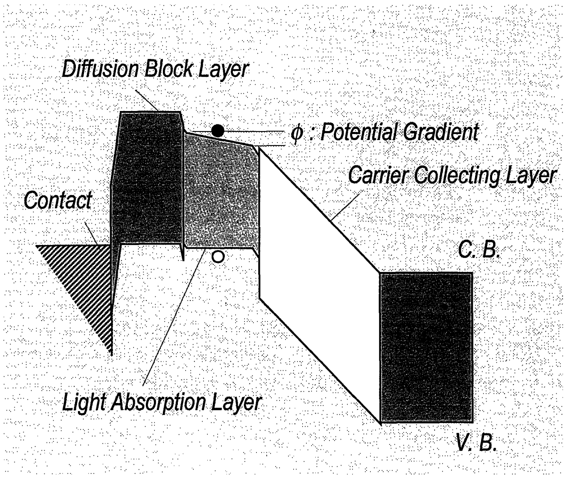


Fig. 1.11: Epitaxial structure proposed by Ishibashi and co-workers, from Ref. [19].

contact. Other possible systems have been considered like the AlGaAs/GaAs or Ge/Si ones with operation wavelengths at 830 nm and 1.55 $\mu$m, but since now they present lower performances compared to the InP/InGaAs system [20, 21].

### 1.2.2 Uni-travelling carrier photodiodes as THz sources

There are basically two different operation modes to employ UTC-PDs as THz sources, the continuous wave and the pulsed regimes. However, due to their response properties, particularly their lower RF powers at high frequencies (above 1-2 THz) compared to other sources like photoconductors, the continuous wave regime is usually the preferred one for their use. This regime has a strong potential for THz applications like imaging or telecommunications which do not forcely need to work above 1 THz.

#### 1.2.2.1 Small-signal operation mode

The approach that follows has been developed by Ishibashi and co-workers and is based on the model reported in Fig. 1.12 [19]. The starting point of the analysis are the current



 

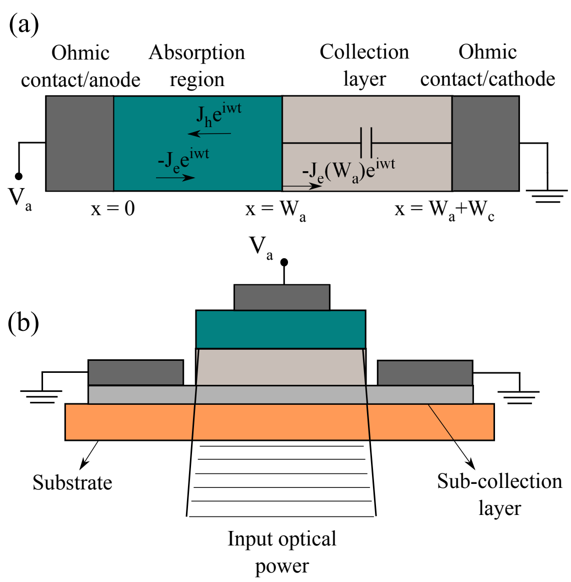


Fig. 1.12: (a) Model for the analysis of the UTC-PD frequency response, from Ref. [19]. (b) Typical UTC-PD device design with back-side illumination.

continuity, drift-diffusion and Poisson equations given by

$$J_e + J_h + \epsilon_s \frac{\partial F_{sc}}{\partial t} = const \tag{1.11}$$

$$\frac{\partial n}{\partial t} = G - \frac{n}{\tau} + \frac{1}{q}\frac{\partial J_e}{\partial x} = G - \frac{n}{\tau} + \frac{\partial}{\partial x}\left[\mu_e n(F_0 + F_{sc}) + D_e \frac{\partial n}{\partial x}\right] \tag{1.12}$$

$$\frac{\partial p}{\partial t} = G - \frac{p}{\tau} - \frac{1}{q}\frac{\partial J_h}{\partial x} = G - \frac{p}{\tau} - \frac{\partial}{\partial x}\left[\mu_h (p + p_0) F_{sc} - D_h \frac{\partial p}{\partial x}\right] \tag{1.13}$$

$$\frac{\partial F_{sc}}{\partial x} = \frac{q}{\epsilon_s}(p - n) \tag{1.14}$$

where $F_{sc}$ is the induced electric field by the electron and hole currents (space charge effects), $G$ is the homogeneous carrier generation rate, $n$ and $p$ are the photo-generated minority electrons and holes, $\tau$ is the electron-hole recombination time and $F_0$ and $p_0$ are the quasi-field and doping hole density within the absorption region. The approximations of the analysis are the following:

1. $F_0$ is not considered.
2. $J_h(x = W_a) = 0$.
3. $p$ is small compared to $p_0$ (low injection regime).
4. The non-linear terms in $nF_{sc}$ and $pF_{sc}$ are neglected.



 

5. The diode is short-circuited - no load resistance.

6. The resistance and the capacitance of the absorption region are negligible.

7. $J_e(x=0)=0$.

8. The diffusion current is limited by the thermionic-emission process.

In the treatment of Ishibashi the quasi-electric field $F_0$ at point (1) was not considered due to the complexity of the problem, however it is possible to take it into account in an approximated way on the final result for the photocurrent. Feiginov has considered it in his derivation where he removed also the condition on the hole current $J_h$ equal to zero at the interface absorption/collection region (see point (2)) [22]. This last approximation is valid for frequencies low compared to the inverse of the transit time within the collection region [22]. The analysis of Ishibashi is simpler than Feiginov's one and remains useful to understand the physics behind these devices holding in many practical cases of interest.

The total photocurrent within the diode can be obtained by integration of Eq. 1.11 over the diode length $W = W_a + W_c$ as

$$J_{ph} = \frac{1}{W}\int_0^W \left(J_e + J_h + \frac{\partial F_{sc}}{\partial t}\right) dx \tag{1.15}$$

where in a short-circuited condition the integral of the electric field over the diode length is zero, while in the case of a load resistance $R_L$ and an excitation signal proportional to $e^{i\omega t}$ with $\omega$ the angular frequency and $t$ the time, a factor $\frac{1}{1+i\omega R_L C}$, analogously to Eq. 1.10, multiplies the short-circuited solution for the photocurrent in the frequency domain [22]. This integral can be splitted into two parts: one associated to $J_e + J_h$ over the absorption region and another one associated to $J_e$ over the collection region by using the approximation at point (2) and (5) leading to

$$J_{ph} = \frac{1}{W}\int_0^{W_a} (J_e + J_h)\, dx + \frac{1}{W}\int_{W_a}^{W} J_e dx \tag{1.16}$$

As already said, the absorption region is highly doped and, for a concentration $p_0 = 10^{18}$ cm$^{-3}$ and low injection levels, the photo-generated holes are negligible from a point of view of the current and the hole current can be written as

$$J_h = q\mu_h p F_{sc} \tag{1.17}$$

Then, deriving Eq. 1.11 for $x$ and using Eq. 1.17 it is possible to obtain the following expression in the absorption region

$$J_e + J_h = J_e(W_a)\left[1 - \frac{i\omega\tau_r}{1+i\omega\tau_r}\left(1 - \frac{J_e}{J_e(W_a)}\right)\right] \tag{1.18}$$



 

where $\tau_r = \epsilon_s/(q\mu_h p_0)$ is the dielectric relaxation time. For $p_0 = 10^{18}$ cm$^{-3}$ it is approximately 30 fs corresponding to characteristic frequencies of nearly 30 THz. Here, it can be observed that, for $\omega < 1/\tau_r$, the current is given just by $J_e(W_a)$, while for $\omega >> 1/\tau_r$ the hole conduction current is negligible. Eq. 1.18 has been obtained by using as boundary conditions the values of $J_e(W_a)$ and $J_h(W_a) = 0$. In what follows the approximation $\omega < 1/\tau_r$ will be adopted and thus the problem simplifies because it reduces to find $J_e(W_a)$. Using the approximations at points (1), (4) and (7) Eq. 1.12 can be linearized and, in a stair-case, re-written as

$$D_e \frac{\partial^2 n}{\partial x^2} - \frac{n}{\tau} + G = 0 \tag{1.19}$$

where the drift term has not been included in agreement with the approximation at point (1). This second order differential equation has a simple solution of the form

$$n(x) = C_1 e^{m_1 x} + C_2 e^{m_2 x} + G/\tau \tag{1.20}$$

where $m_{1/2}$ are $\pm 1/(\sqrt{D_e \tau})$ and $C_1$, $C_2$ are two constants to be found by applying appropriate boundary conditions. A small perturbation varying like $e^{i\omega t}$ can be introduced and taken into account by substituting as usual $\tau$ with $\tau/(1 + i\omega\tau)$ and considering each variable with the same dependence. The boundary conditions that are more reasonable to avoid an underestimation or an overestimation of the photocurrent are

$$J_e(x = 0) = qD_e \left.\frac{\partial n}{\partial x}\right|_{x=0} = 0 \tag{1.21}$$

$$J_e(x = W_a) = qD_e \left.\frac{\partial n}{\partial x}\right|_{x=W_a} = -qv_{th} n(W_a) \tag{1.22}$$

where $v_{th}$ is the thermionic emission velocity equal to $\sqrt{\frac{2k_B T}{\pi m_e^*}}$. Here, again the drift term of the current is not considered. Eq. 1.21 refers to the fact that the current is related only to the holes at the interface absorption/anode region and applying this first condition (Eq. 1.21) to Eq. 1.20, the relation $C_1 = C_2$ is obtained. $C_1$ can be found by applying Eq. 1.22 to Eq. 1.20. An approximation of Eq. 1.20 to its second order Taylor series (justified for absorption regions of few hundreds of nm) gives

$$J_e(W_a, \omega) = -\frac{qGW_a}{1 + (W_a/v_{th} + W_a^2/2D_e)/\tau + j\omega(W_a/v_{th} + {W_a}^2/2D_e)} \tag{1.23}$$

The total current in the absorption region $J_e^{abs}(\omega)$ is given by Eq. 1.23 multiplied by its contribution $W_a/W$ to the whole diode length. The recombination lifetime $\tau$ in p-type $In_{0.53}Ga_{0.47}As$ is roughly 100 ps [19], much larger than the time required to the electrons to be swept out from the absorption region. Thus, for small absorption region thicknesses (few hundreds of nm), it can be neglected. Here, an effective transit time in the absorption region $\tau_a$ can be introduced equal to the diffusion time $W_a^2/2D_e$ plus the correction factor $W_a/v_{th}$ which accounts for a finite $v_{th}$ [19] and, for an absorption region of 150 nm, can be estimated to 2.4 ps by using $\mu_e = 5000$ cm$^2$·V$^{-1}$s$^{-1}$ and $v_{th} = 1 \cdot 10^7$ cm/s [19, 22]. In the case of a quasi-electric field the diffusion time can be modified in $\tau_a = W_a/v_d$ with $v_d = \mu_e F_0$ for $v_d >> v_{th}$ [22]. In Fig. 1.13 it can be observed the role played by the potential within the absorption region to shift the electron density towards the collection region and consequently decreasing $\tau_a$. The electron current in the collection region under

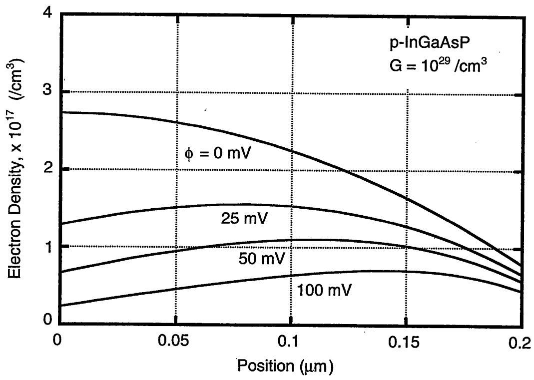


Fig. 1.13: Effect of a potential drop over the electron density within a 0.2-$\mu m$-thick absorption region in InGaAsP, from Ref. [19].

small-signal analysis can be obtained by integrating the time dependence $e^{i\omega t}$ of the current during the transit time $\tau_t = W_c/v_{sat}$ with $v_{sat}$ the saturation speed of the electrons in the collection region. By multiplying this transfert function for the injected current previously calculated gives

$$J_e^{coll}(\omega) = \frac{W_c}{W} J_e(W_a) \frac{\sin(\omega\tau_t/2)}{\omega\tau_t/2} e^{-i\omega\tau_t/2} \tag{1.24}$$

This expression is quite different from that of Eq. 1.10 due to the fact that the current is injected from one side of the collection region and consequently the drift time is the same for all the carriers. By using Eq. 1.23 with the above approximations, Eq. 1.24 and by multiplying for the factor related to the $RC$ charge time, the final expression for the total photocurrent is

$$J_{ph} = -\frac{qGW_a}{1+i\omega\tau_a} \frac{\sin(\omega\tau_t/2)}{\omega\tau_t/2} e^{-i\omega\tau_t/2} \frac{1}{1+i\omega\tau_{RC}} \tag{1.25}$$

The RF averaged output power can be easily found by

$$P_{RF} = \frac{1}{2} |J_{ph}\Sigma|^2 R_L \tag{1.26}$$



 

where the factor 1/2 comes from the time average of the square of the photocurrent $J_{ph}e^{i\omega t}$. There are three characteristic times that govern the UTC-PD response before saturation differently from p-i-n PDs where only the transit time and the RC charge time are involved. This aspect has to be taken into consideration during the epitaxial design, in particular for the optimal frequency range of operation.

#### 1.2.2.2 Continuous wave regime: photomixing principles

In 1947 Forrester and co-workers proposed to use optical signals at different frequencies in the visible range to generate a beating note [23]. The beating note signal could be generated by the superposition of these signals in a non-linear device that satisfies two basic conditions:

- The non-linear process has to be proportional to the optical electric field averaged over a time much shorter than the inverse of the beating frequency.
- The characteristic time of the device response to this process has to be much shorter than the inverse of the beating frequency.

These two conditions are fundamental to be able to detect the beating note related to the modulation of the non-linear process. The absorption in a semiconductor for example is a typical non-linear process and, in the case of two co-linear lasers signals at frequencies $\nu_1$ (pulsation $\omega_1 = 2\pi\nu_1$) and $\nu_2$ (pulsation $\omega_2 = 2\pi\nu_2$), the generation rate at a point $\mathbf{r}$ can be expressed as [24]

$$G(\boldsymbol{r}, t) = \alpha \frac{(F_1 \cos(\omega_1 t) + F_2 \cos(\omega_2 t + \phi))^2}{Zh\nu} \tag{1.27}$$

with $\alpha$ the absorption coefficient, $F_1$ and $F_2$ the amplitudes of the electric fields evaluated in $\boldsymbol{r}$, $\phi$ the phase difference between the two lasers signals, $Z$ the intrinsic impedance of the semiconductor equal to $\sqrt{\frac{\mu_r}{\epsilon_r}}Z_0$ with $\mu_r$, $\epsilon_r$ and $Z_0$ the relative permeability, permittivity and vacuum impedance ($\approx 377\ \Omega$), respectively and $h\nu$ the average photon optical energy. Eq. 1.27 can be developed further to obtain

$$\begin{aligned} G(\boldsymbol{r}, t) = {} & \alpha \frac{\left(F_1{}^2(1 + \cos(2\omega_1 t))/2 + F_2{}^2(1 + \cos(2\omega_2 t + 2\phi))/2\right)}{Zh\nu} + \\ & + \alpha \frac{(F_1 F_2 \cos((\omega_1 - \omega_2)t - \phi) + F_1 F_2 \cos((\omega_1 + \omega_2)t + \phi))}{Zh\nu} \end{aligned} \tag{1.28}$$

By averaging Eq. 1.28 over an optical period ($\approx 5$ fs at 1.55 $\mu$m), that means to implicitly assert that the non-linear device cannot respond within the optical carrier period, as is the case of any electronic device due to the $RC$ charge time, leads to

$$G(\boldsymbol{r}, t) = \alpha \frac{\left(I_1 + I_2 + 2\sqrt{I_1 I_2}\cos\left((\omega_1 - \omega_2)t - \phi\right)\right)}{h\nu} \tag{1.29}$$

with $I_{1/2} = {F_{1/2}}^2/2Z$ the average optical intensities. It can be easily proved that the difference frequency term is maximum for $I_1 = I_2$ given a fixed amount of total intensity $I = I_1 + I_2$.

In 1955 Forrester and co-workers have firstly demonstrated experimentally photomixing of two Zeeman spectral lines by atomic transitions in a photo-cathode at 10 GHz [25]. In the '60s, the advent of lasers has boosted the technique of photomixing. Generation of mm-wave frequencies by photomixing using semiconductor absorption as non-linear phenomenon has been proved for the first time in bulk semiconductors by DiDomenico and co-workers in 1962 using the axial modes of a ruby laser [26]. After the demonstration of Brown in 1993, photomixing has been commonly used as a continuous wave (CW) method to generate THz radiation [24, 27]. High-purity and stable laser sources can be employed to achieve analogous properties in the THz range due to the fact that the photomixing effect intrinsically reflects the quality of the input sources [28].

### 1.2.2.3 Pulsed regime

Another solution to generate THz radiation consists in employing short optical pulses ($\leq$ ps) around a certain frequency. The reason is that their Fourier transform spectra can have a broad extension of several THz. Roughly its extension goes as $1/\tau_p$ with $\tau_p$ the pulse time extension.

The current technology is able to produce laser chains with a pulse time extension lower than 100 fs and wide wavelength coverage [29]. In practice, the limiting factor on the spectral extension of the THz generated radiation is the bandwidth of the device which is illuminated by fs pulses. The slower the device is, the weaker the response will be at high frequency. In Fig. 1.14 (a) it is reported an example of UTC-PD pulse response. The pulse at 1.55 $\mu$m had a full width at half maximum (FWHM) of 280 fs and the resulting spectra of the photocurrent a FWHM of 0.97 ps. By Fourier transform it is possible to directly obtain the frequency response of the UTC-PD as shown in Fig. 1.14(b). However, under strong optical powers, saturation problems can be observed which may limit the use of UTC-PDs in this regime [30]. In the last chapter a technique called terahertz-time-domain (TDS) spectroscopy based on the generation and detection of broadband THz signals obtained in the pulsed regime will be presented.



 

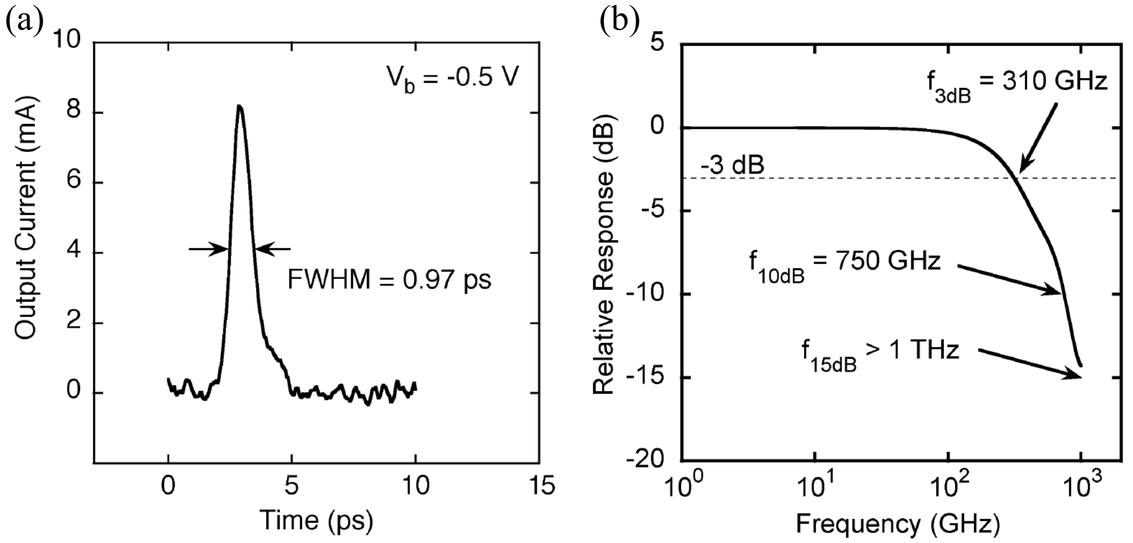


Fig. 1.14: (a) Response of a UTC-PD with a 5 $\mu$m area, a 230-$\mu$m-thick collection and a 30-nm-thick absorption regions. (b) Fourier transform of the photocurrent underlying the cut-off frequency at 310 GHz, from Ref. [15].

### 1.2.3 State of the art within the THz community

Since the invention of UTC-PDs many efforts have been done to achieve higher output powers, efficiencies and cut-off frequencies [27, 31]. The main limitations to accomplish these objectives are basically:

- The saturation under high injection regime.
- The thermal failure related to the power absorbed actively and passively.
- The intrinsic bandwidth.
- The coupling between the input power and the active region.
- The coupling between the RF power and the antenna.

Higher levels of saturation have been shown for UTC-PDs compared to standard p-i-n PDs due to different electron and hole density distributions within the structure [19]. Particularly, it has been demonstrated an improvement in the saturation current by using an n-type doping in the collection region ($5{\cdot}10^{16}$ cm$^{-3}$) to compensate for space charge effects through partial screening of the negative charge flowing in the collection region by the positive ionized atoms [32]. This effect, which is well-known in heterojunction bipolar transistors (HBT) under the name of Kirk effect, was also predicted by drift-diffusion simulations in the original patent of Ishibashi as reported in Fig. 1.15 [33, 34]. Moreover, quaternary materials like InGaAsP or AlGaInAs with a larger energy gap than $In_{0.53}Ga_{0.47}As$ can be used to efficiently smooth the CB discontinuity between absorption and collection regions as shown in Fig. 1.16 [35].

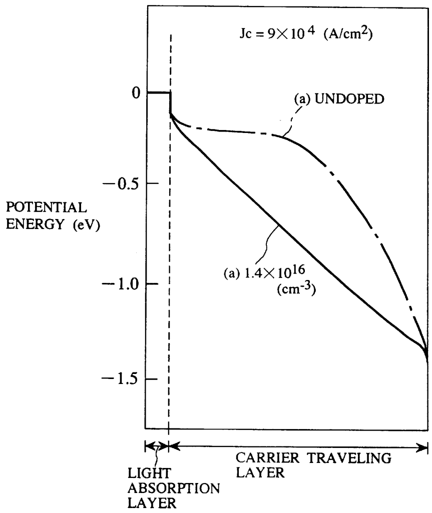


Fig. 1.15: Influence of the doping in the collection region to maintain a high electric field under strong illumination (equivalent photocurrent of $9{\cdot}10^4$ A/cm$^2$) [34].

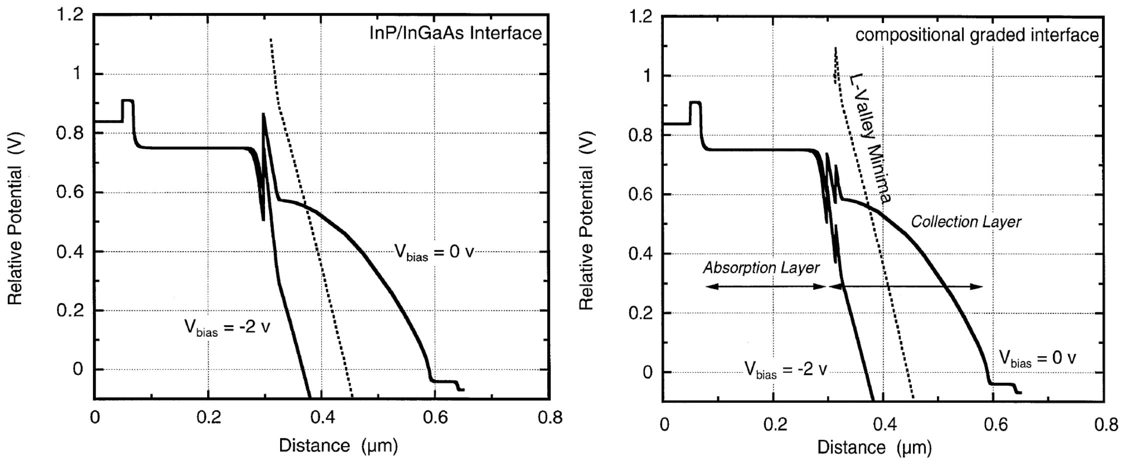


Fig. 1.16: Role of a quaternary (InGaAsP) doped material between the absorption and collection region to smooth the CB discontinuity [35].



 

Heat dissipation is a key issue in the operation of UTC-PDs, in fact it has been often proved to be one of the main limiting reasons to achieve higher output powers [22, 36, 30]. The energy balance in a PD can be written as [37]

$$P_{diss} + P_{RF} = P_{bias} + P_{opt}^{abs} \tag{1.30}$$

where the first term at the left member is the sum of the Joule dissipated power in the whole structure and the RF power dissipated in the load and the first term at the right member is the power provided by the generator ($I^{DC}V_b$), while the second term $P_{opt}^{abs}$ is the optical power absorbed in the active region and potentially in other parts of the PD like the metal ohmic contacts or in other epitaxial layers as in the case of the previous Ph.D thesis on UTC-PDs within the EPIPHY/THz photonics group [30]. As it can be observed in Fig. 1.17, the burnt-out of a PD appears principally (without unwanted absorption) in the intrinsic region, no matter which type of PD is. However, UTC-PDs have shown a better power dissipation compared to standard p-i-n PDs, achieving for example a dissipated power of 240 mW instead of 160 mW in the case of a p-i-n PD at equivalent conditions and geometries due to the better conductivity of InP (roughly 10 times) compared to InGaAs [36]. To improve the heat dissipation, several ways have been considered like using larger diode surfaces or using non-uniformely-doped collection regions to keep a low capacitance and a low transit time leading to saturation currents as high as 120 mA with dissipated powers of 480 mW at 20 GHz and bandwidths as high as 35 GHz [38]. Other

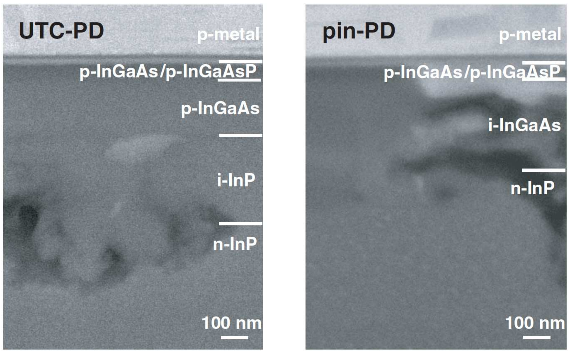


Fig. 1.17: SEM images of the thermal failure of a UTC-PD and a p-i-n PD. The black part is a vacancy due to the melting of the semiconductor, from Ref. [36].

methods rely on heat sinking directly on the chip through pads, flip-chip techniques to bond the UTC-PD on a substrate with a better conductivity like AlN or by using ballistic transport to increase the collection region width. These techniques employed all together have led to a saturation current of 37 mA with a bandwidth larger than 110 GHz [39].



 

UTC-PDs bandwidth is certainly the point on which there has been more work done. In fact, notwithstanding the analysis previously seen about the UTC-PD response, no words have been spent discussing the way UTC-PDs can be illuminated. Such an issue is quite critical due to the fact that UTC-PDs for THz radiation have absorption regions often between 30 to 150 nm to keep a low diffusion/drift time in this region. A quasi-electric field can be used, as already discussed before, to accelerate them, but even in this case it is not possible to have more than a voltage drop of few tens of mV in the whole absorption region. The reason is that the doping or the compositional gradient cannot be freely tuned. In the first case, high doping levels lead to a low-efficiency photo-generation process due to a faster recombination of the pairs, while on the other side a low doping level makes the holes responding as in a p-i-n PD. In the second case, the composition can be varied, but the effect of the strain has to be taken into account and, if too far from the LM condition, it can lead to a relaxation of the whole structure.

The coupling between the input power and the active region is strongly correlated to the intrinsic bandwidth of the UTC-PD. The most common way of illuminating UTC-PDs is the back-side configuration that consists in focusing the 1.55 $\mu$m power through the transparent and polished InP substrate. An anti-reflection coating can be added to the substrate to avoid the Fresnel reflection at the InP/air interface (around 30%). In such a configuration the advantage is the covering of the top mesa with a thick metal contact or a high-reflection coating to make the light passing through the active region twice. Front-side illumination can be exploited by making an optical transparent window at the top contact or by focusing the beam through a mirror at the bottom of the substrate as reported in Fig. 1.18. While, the back-side configuration has the disadvantage of being more difficult to be achieved due to the fact that the device is located opposite to the incoming beam, the front-side illumination is less efficient because the light experiences the absorption region only once in the case of an optical window or twice, but with reflection losses at the top contact surface, in the case of light focusing through a bottom mirror (see Fig. 1.18). To increase the efficiency, without reducing the bandwidth related to the absorption region, edge illumination has been investigated. In Fig. 1.19 is reported a design to illuminate UTC-PDs through a refracting-facet to increase the optical path in the active region by having an impinging angle different from 90° [41]. This design has led to UTC-PDs with responsivities as high as 1 A/W for a 452 nm-thick absorption region. Other edge illumination techniques consist in waveguiding the optical power through the epitaxial structure [31]. The active region can be designed to guide the light through a waveguiding section or to have light evanescently coupled into it thanks to a neighbouring waveguiding section [42, 43]. In the second situation the evanescent coupling has the



 

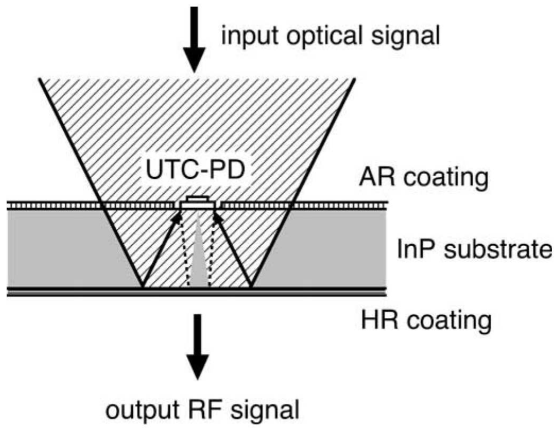


Fig. 1.18: Front-side illumination through a high-reflecting coating at the bottom of the substrate, from Ref. [40].

effect of increasing the saturation current of the PD due to the smaller amount of light absorbed per unit length compared to the first situation. This approach, reported in Fig. 1.20, has been adopted for distributed photodiodes like traveling wave (TW) UTC-PDs which have shown record powers of 2.4 mW at 150 GHz and of 1 mW at 200 GHz. The advantages of this design are the possibility to reduce the absorption region width and to achieve responsivities as high as 0.53 A/W for a 120 nm-thick absorption region [44]. The main drawbacks of this configuration are related to the alignment of the optical fiber to the tapered waveguide that is quite critical and to the higher complexity of the structure design due to a phase matching condition to fulfill between the optical and the RF powers and to the evanescent optical coupling [45, 46].

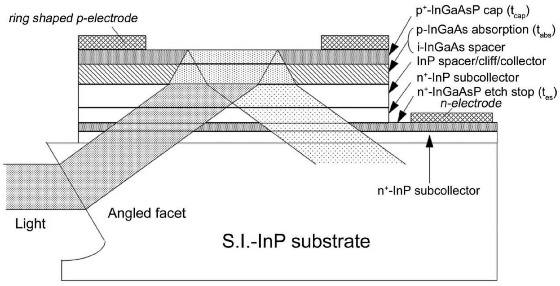


Fig. 1.19: Edge illumination by exploiting a refracting-angled-facet, from Ref. [47].

Another aspect correlated to the bandwidth of the device is the choice of the antenna. Resonant antennas coupled with impedance-matching circuits show higher radiating RF



 

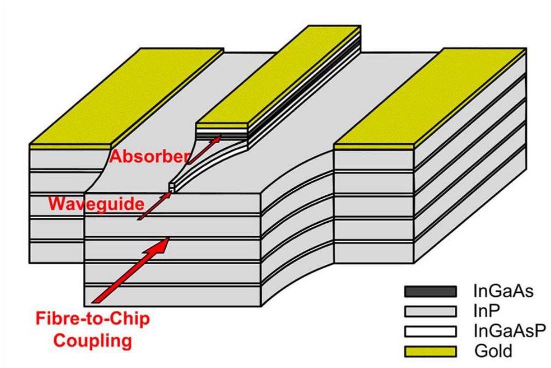


Fig. 1.20: Design employed by the University College London for TW UTC-PDs, from Ref. [44].

powers than broadband antennas for a specific designed frequency range by suppressing partially or completely (depending on the resonant antenna impedance and the matching circuit) the $RC$ limitation [48]. Record powers of 148 $\mu$W at 457 GHz and of 24 $\mu$W at 914 GHz have been demonstrated for TW UTC-PDs with resonant slot antennas [49]. Finally, arrays of UTC-PDs can be considered to increase the output power by wise configuration of the network and radiating elements. A module composed by two laterally illuminated UTC-PDs connected by a quarter wavelength T-line has shown a 1.2 mW record power at 300 GHz [50].

UTC-PDs fabricated in the previous Ph.D thesis in the EPIPHY/THz photonics group have produced RF powers of 1.1 $\mu$W at 940 GHz and of 0.27 $\mu$W at 1.36 THz for a 2-$\mu$-diameter device integrated with an ultra broadband TEM horn antenna which will be presented in the third chapter [30]. Higher RF powers are potentially achievable on narrow frequency ranges by employing resonant antennas.

## 1.3 Survey of other THz sources

In this section other sources to generate THz radiation will be briefly introduced. In particular, their advantages and disadvantages will be underlined in terms of applications without going into the details of their operation.

### 1.3.1 Optical domain

The main optical sources in the THz/far-infrared region are based on molecular lasers, quantum cascade lasers (QCLs) and non-linear optical materials.



 

#### 1.3.1.1 Molecular lasers

Molecular lasers have been used since 1964 when Crocker employed water vapours to generate radiation in the far-infrared region [51]. The basic principle of these lasers is to induce molecules in an excited state of their roto-vibrational energy spectrum by means of an electrical discharge or by optical pumping. The reason for which this type of transitions are employed is that the energies involved in the process of stimulated emission are compatible to the photon energies associated to the far infrared spectrum. This is also the reason for which atoms are generally not used as their electronic energy spectrum has characteristic energies in the order of the eV (1 eV corresponds to 241.8 THz) for the first atomic levels (s orbitals). Other higher levels may be used for heavy atoms, but the excitation of these levels can bring to the ionization of the atom which may become useless for the lasing process having shifted transition lines. In Tab. 1.1 the main lines covered by molecular lasers are shown depending on the different gas used, their output powers and their operation regime. The main advantage of molecular lasers is that they

Table 1.1: A few far-infrared lines of molecular gas lasers

| Gas type | $\lambda(\mu m)$ | Regime | Output power | Pumping | Ref. |
|---|---|---|---|---|---|
| $CO_2$-$N_2$-He | 10.6 | Pulsed | 0.5 MW | Discharge | [52] |
| $H_2O$ | 28 | CW | 230 mW | Discharge | [53] |
| $NH_3$ | 58 | Pulsed | 20 W | Optical | [54] |
| $D_2O$ | 66 | Pulsed | 28 kW | Optical | [55] |
| $H_2O$ | 118.6 | CW | 50 mW | Discharge | [56] |
| $CH_3OH$ | 118.8 | CW | 1.25 W | Optical | [52] |
| HCN | 337 | CW | 20 mW | Discharge | [57] |
| $CH_3F$ | 496 | Pulsed | 1 MW | Optical | [58] |

are extremely powerful as illustrated by the output powers reported in Tab. 1.1, but they lack of tunability which makes them difficult to use for applications where the tuning of the source is fundamental like in broadband THz spectroscopy or communications. Moreover, they are generally bulky and require usually high electrical or optical powers to be operated.

#### 1.3.1.2 Quantum cascade lasers

QCLs have been invented in 1994 at Bell Labs by F. Capasso and co-workers [59, 60]. Their principle is based on the original idea of Kazarinov and Suris to obtain amplified emission using electronic transitions from subbands of a multi-quantum well structure under the application of an intense electric field [61]. In Fig. 1.21 it is reported the band diagram of a QCL stage showing the process of electron recycling and photon emission.



 

In particular, electrons from the injector are made tunneling by an electric field in the quantum-wells active region where, for currents higher than a threshold current to achieve population inversion like in a common laser, they are induced to transit in a lower level by stimulated emission and then tunnelling in the energetically lower injector to restart the mechanisms.

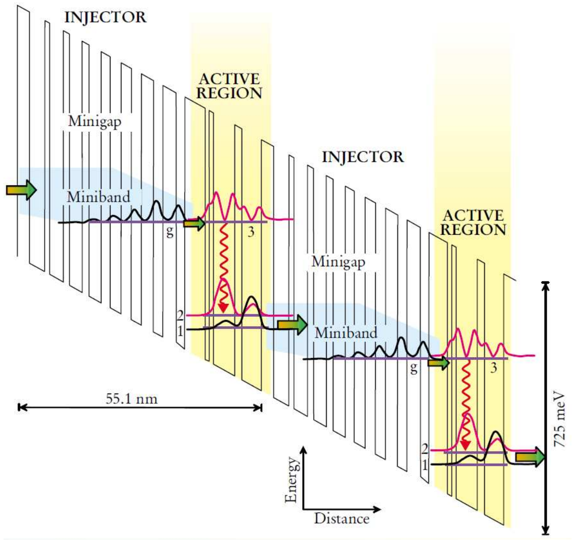


Fig. 1.21: Band diagram of a QCL stage showing the principal key features [62].

These lasers can be designed to operate at a particular wavelength by changing the width of the quantum wells and can achieve powers as high as 5.1 W under CW regime and RT operation at 4.9 $\mu$m [63]. At THz frequencies, their major drawbacks are the low operation temperature for THz frequencies and their relatively poor tuning range compared to other sources like photomixers. To date, a maximal operation temperature of 200 K has been obtained for THz QCL with lasing tunable frequencies from 2.6 to 2.85 THz by increasing the bias (Stark effect) [64]. The lowest lasing frequency achieved with the GaAs/AlGaAs system is of 950 GHz by using a magnetic field of 12 T and cryogenic temperatures up to 57 K [65]. These achievements have been obtained by design schemes for the active regions such as the bound-to-continuum or the resonant-phonon ones [66]. Regardless their drawbacks, QCLs are compact and can present multiple wavelength emission by employing superlattices or larger quantum wells widths [67, 68].



 

#### 1.3.1.3 Non-linear-based optical methods

Non-linear-based methods rely on materials presenting a non-linear polarization dependence from the applied electric field. In particular, the polarization vector of any material can be written under certain assumption as a power series of the applied electric field [69]:

$$\boldsymbol{P(t)} = \epsilon_0(\chi^{(1)}\boldsymbol{F(t)} + \chi^{(2)}\boldsymbol{F(t)}\cdot\boldsymbol{F(t)} + \chi^{(3)}\boldsymbol{F(t)}\cdot\boldsymbol{F(t)}\cdot\boldsymbol{F(t)} + ...) \quad (1.31)$$

where $\chi^{(i)}$ is the non-linear susceptibility tensor of order $i$. Recalling that the polarization vector is the dipole moment per unit volume in a material, it is straightforward to conclude that an applied time-varying field can induce a radiative process with a different time-varying dependence. In the particular case of a monochromatic electric field impinging on a material with a $\chi^{(2)}$ value different from zero, a second-order harmonic generation process can be achieved. Franken and co-workers firstly demonstrated second harmonic generation (SHG) of light at a wavelength of 347.2 nm (864 THz) from a Ruby laser (wavelength of 694.3 nm) using a quartz crystal as non-linear medium [70]. For parametric effects the main constraints associated to the THz generation come from the low $\chi^{(2)}$ values, the phase-matching condition, parasitic effects like SHG in difference or sum frequency generation and the damage-threshold value of crystals [69]. In particular, materials with an anisotropy in their crystalline structure like noncentrosymmetric crystals ($LiNbO_3$, $LiIO_3$, GaP, GaAs) are commonly employed with values for their non-linear susceptibility ($\chi^{(2)}$) in the order of $10^{-11}$, $10^{-12}$ m/V [71]. To overcome the phase-mismatch due to the normal dispersion of the refractive index at different frequencies, periodically $\chi^{(2)}$-inverted structures have been conceived [72]. The most common nonlinear processes are the sum-frequency generation (of which second-harmonic generation is a special case) $\nu_1 + \nu_2 = \nu_3$ and the difference-frequency generation $\nu_1 - \nu_2 = \nu_3$ with $\nu_1$ and $\nu_2$ the input frequencies and $\nu_3$ the output one. Peak powers as high as 23.4 mW have been achieved at 1 THz by pumping at 1.55 $\mu$m periodically $\chi^{(2)}$-inverted structures like GaP [73]. Such material is very interesting for the THz domain due to its low absorption at THz frequencies compared to $LiNbO_3$ for ex. (about ten times smaller) [73]. The main advantages of nonlinear methods are related to the high powers that can be generated, to the quite large tunability of the process (phase-matching condition to satisfy) and to the RT operation. The main drawbacks are the bulky nature of these systems (due to the high-power lasers used), the quite low efficiency related to the Manley-Rowe limit (analogous to the energy conservation principle) and the pulsed-regime operation (due to the high peak electric fields) [69]. However, recently a CW power of 0.5 mW has been produced at 1 THz by a two-lines tuneable vertical external cavity surface emitting laser coupled to a $LiNbO_3$:Mg crystal placed in the external cavity [74].

### 1.3.2 Electronic domain

In the electronic domain the main sources for THz generation are backward oscillators, transistors-based oscillating circuits, varactor multipliers and tunneling resonant diodes. Contrarily to optical sources, electronic ones cover mostly the low part of the THz region, up to a few THz.

#### 1.3.2.1 Backward oscillators

These free electron-based sources have been invented independently by B. Epzstein and R. Kompfner in the 50's and are based on traveling-wave tube theory [75, 76]. Other free electron sources of THz radiation are gyrotrons, free electron lasers, synchrotrons and klystrons [77]. Their working principle is based on the injection of an electrons flux in a vacuum tube with a voltage-controlled velocity (a few kV) along the tube. Fluctuations of the electrons movement along of a slow-wave periodical transmission line (similar to microwave bandpass filter) generate radiation which can sum up if a synchronous condition is satisfied between the periodicity of the transmission line and the phase of the electron beam. The generated radiation moving in the opposite direction of the electron flux (negative group velocity) can be tuned by changing the applied voltage and thus the electron velocity [78, 79]. The spectrum that can be covered with different designs is roughly from 30 GHz to 1.2 THz [77]. The main advantages of this source are the relatively wide tunability, the high output powers that can be achieved in the THz region (1-100 mW) and the RT operation. However, they are generally bulky, requiring strong magnetic and electric fields and are produced currently only in a few places in US and Russia [77].

#### 1.3.2.2 Transistors-based oscillating circuits

Transistors, discovered in the late 40's at Bell Labs by Bardeen, Shockley and Brattain as current amplifiers, have improved their performances constantly during the last decades [80, 81, 82, 83]. Different topologies have been developed depending on the needs of the applications like heterojunction bipolar transistors (HBTs), field effect transistors, metal-oxide-semiconductor transistors or high-electron mobility transistors to cite just a few.

These devices have experienced throughout their development an increase of their working frequencies represented by the figures-of-merit $\nu_t$ and $\nu_{max}$ where $\nu_t$ is the transition frequency at which the current gain is unitary and $\nu_{max}$ is the maximum oscillation frequency at which the power gain is unitary [84]. Record values of $\nu_{max}$ = 1.15 THz and of $\nu_t$ = 521 GHz have been achieved on InP/InGaAs/InP double HBT structures [85]. Oscillators based on InP/InGaAs/InP HBT and InP HEMT have shown record oscillation frequencies of 311 and 346 GHz [86, 87]. Losses at mm frequencies and dimensions shrinkage (sub-$\mu$m) for higher operation frequencies limit their theoretical potential through lowering resonant factor qualities increasing parasitic effects.

Other approaches have been investigated like using transistors in frequency-multiplication chains driven below their cut-off frequency and generating higher harmonics of the main signal by multiplication in non-linear elements like varactor diodes. This technique allows to obtain sources at frequencies well above 300 GHz with powers that can be as high as 1 mW at 0.9 THz, 50 $\mu$W at 2 THz and 18 $\mu$W at 2.6 THz [88]. The main advantages of transistor-based sources are their compactness, RT operation, possibility to deliver high output powers (depending on the band) [88]. The main drawbacks are the relatively low tuning range of roughly 10% their central frequency due to the matching circuitry and to the phase noise output that has to be considered (it increases with the order of the harmonic).

#### 1.3.2.3 Resonant tunneling diodes

Resonant tunneling in semiconductor heterostructures has been observed for the first time in 1974 at IBM Labs where Chang and co-workers measured peaks in the current response by varying the bias of a sandwiched GaAlAs/GaAs/GaAlAs structure as shown in Fig. 1.23 [90]. The principle is related to the resonant character of the transmission of electrons when their energy is aligned with the energy of a quantum well level which permits by tunneling to overcome the barrier and to obtain a larger current. The characteristic reported in Fig. 1.23 shows that there



 

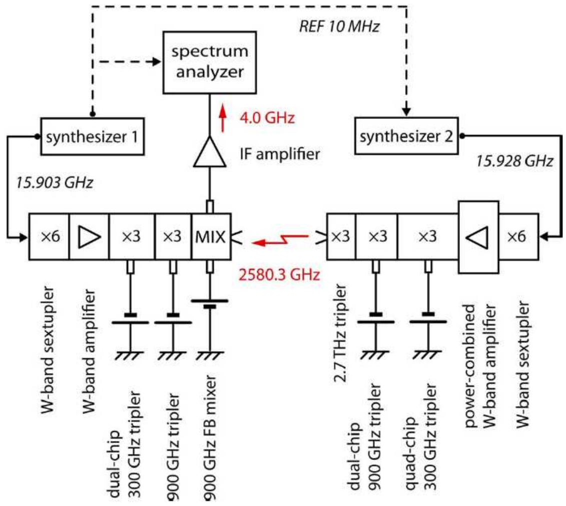


Fig. 1.22: Oscillator scheme at 2.58 THz based on frequency multiplication chains and mixers [89].

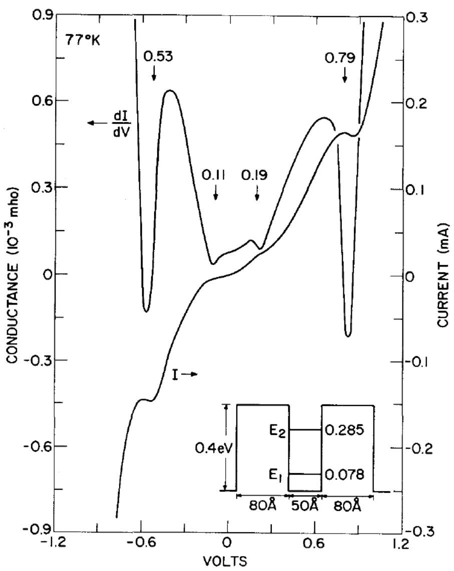


Fig. 1.23: Conductance and current response as a function of the applied bias to a GaAlAs/GaAs/GaAlAs structure, from Ref. [90].

are regions of the applied voltage where the structure has a negative differential conductance ($dI/dV < 0$). This effect has been used in oscillators feeedback loops to obtain the currently highest frequency active electronic semiconductor device by operating the RTD at the edge of one of its current peaks [91]. Powers of 7 $\mu$W have been achieved at 1.04 THz and of 10 $\mu$W in the 0.9-1 THz range by carefully designing the heterostructure, in particular minimizing the resonant tunneling time and the transit time in the collection region [92].

The main advantages of these sources are their compactness, their relatively high powers at THz frequencies (powers of $\mu$W for spectroscopic applications are often sufficient) and their RT operation. Due to their resonant character the tuning range is only in the order of few percents [92].

### 1.3.3 Optoelectronic domain

Here, a brief introduction to photoconductors is given, focusing on their main characteristics compared to UTC-PDs.

#### 1.3.3.1 Short lifetime photoconductors

Brown and co-workers in 1995 have employed photoconductors with short carrier lifetime (sub-ps) and high dark-resistivity ($10^6$ $\Omega\cdot$cm) like low-temperature-grown (LTG) GaAs to generate tunable THz radiation up to 3.8 THz [93]. Their working principle is based on photomixing as UTC-PD's one with the major difference that the carriers, once photogenerated, are accelerated by an externally applied electric field. GaAs-based photoconductors operate at a wavelength of 800 nm and are front-illuminated with interdigitated electrodes or semitransparent contacts [94, 95]. The front illumination is usually needed for these devices due to the absorption of GaAs substrates at 800 nm. Other systems based on InGaAs have been considered to illuminate these devices at 1.55 $\mu$m taking advantage of all the benefits already discussed related to this wavelength of operation. However, they have shown lower performances compared to standard LTG-GaAs photoconductors [96]. Their frequency response is associated to the carriers lifetime (sub-ps) which is the time between their creation and subsequent recombination and to the $RC$ time constant. Recently, on-wafer measured powers of 1.2 mW at 50 GHz and of 0.35 mW at 305 GHz have been obtained with a Fabry-Pérot cavity embedded LTG-GaAs photoconductors and of 2 $\mu$W at 1 THz with resonant antennas and interdigitated contact designs [94]. Cut-off frequencies as high as 700 GHz can be obtained by this type of devices in interdigitated designs [95]. Their advantages are the compactness, the broadband character and the RT operation. The main drawbacks come from the low power generated above 1 THz (sub-$\mu$W) and the need of sources at 800 nm which are less conventional and more expensive than those at 1.55 $\mu$m.

### 1.3.4 Role of uni-travelling carrier photodiodes in the THz domain

UTC-PDs are with no doubt a valuable source in the THz domain due to their several features, in particular RT operation and broadband operation. In Fig. 1.24 their impact in the THz region compared to other THz sources is shown. Even though their generated powers are lower than those from other sources more adapted in the optical domain or in the electronic domain, they are a good compromise for all those applications demanding a large tunability like spectroscopy of a wide variety of species, where no precise target has to be detected or telecommunications with a high bit-rate without the need of using expensive and bulky cryogenic systems. The only other sources able to cover a similar band in the THz region are frequency-multipliers chains but, as already discussed before, they do not have a large tunability differently from UTC-PDs.

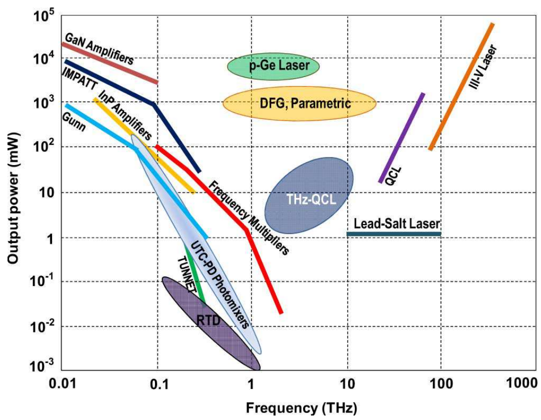


Fig. 1.24: Output powers of the main sources in the THz region. THz QCLs operate at cryogenic temperatures. The power reported for THz QCLs and II-V lasers are peak powers. Gunn, TUNNET and IMPATT are diode-based sources, from Ref. [97].



 

# Bibliography


[1] Russel S. Ohl, *American patent 2402661* (1946)

[2] Russel S. Ohl, *American patent 2402662* (1946)

[3] http://www.nextnano.de/

[4] Neil W. Ashcroft and David N. Mermin, *Solid state physics* (Harcourt college publishers, 1976)

[5] Simon S. Sze, *Semiconductor devices - Physics and technology 2nd edition* (John Wiley & Sons and Inc, 2001)

[6] Eugene Hecht, *Optics (4th edition)* (Addison-Wesley, 2002)

[7] A. G. Baca, F. Ren, J. C. Zolper, R. D. Briggs, and S. J. Pearton, *A survey of ohmic contacts to III-V compound semiconductors*, Thin Solid Films **308-309**, 599 (1997)

[8] Sadao Adachi, *Physical properties of III-V semiconductor compounds: InP, InAs, GaAs, GaP, InGaAs and InGaAsP* (John Wiley & Sons, 1992)

[9] J. R. Lowney, H. S. Bennett, *Majority and minority electron and hole mobilities in heavily doped GaAs*, J. Appl. Phys. **69**, 7102 (1991)

[10] J. Nishizawa, Y. Watanabe, *Japanese patent 205068* (1950)

[11] E. Fred Shubert, *Light-emitting diodes* (Cambridge University Press, 2002)

[12] T. P. Pearsall, M. Piskorski, A. Brochet, and J. Chevrier, *A Ga0.47In0.53As/InP heterophotodiode with reduced dark current*, IEEE J. Quant. Electron. **17**, 255 (1981)

[13] Y.-L. Huang, C.-K. Sun, *Nonlinear saturation behaviors of high-speed p-i-n photodetectors*, J. Lightwave Technol. **18**, 203 (2000)

[14] V. L. Dalal, *Hole velocity in p-GaAs*, Appl. Phys. Lett. **16**, 489 (1970)

[15] H. Ito, S. Kodama, Y. Muramoto, T. Furuta, T. Nagatsuma, and T. Ishibashi, *High-speed and high-output InP-InGaAs unitravelling-carrier photodiodes*, IEEE J. Sel. Topics Quant. Elect. **10**, 709 (2004)

[16] P. Hill, J. Schlafer, W. Powazinik, M. Urban, E. Eichen, and R. Olshansky, *Measurement of hole velocity in n-type InGaAs*, Appl. Phys. Lett. **50**, 1260 (1987)

[17] K. J. Williams, R. D. Esman, R. B. Wilson, and J. D. Kulick, *Differences in p-side and n-side Illuminated p-i-n photodiode nonlinearities*, IEEE Photonic. Tech. Lett.. **10**, 132 (1998)

[18] P. Liu, K. J. Williams, M. Y. Frankel, and R. D. Esman, *Saturation characteristics of fast photodetectors*, IEEE Trans. Microwave Theory Techniques **7**, 1297 (1999)

[19] T. Ishibashi, S. Kodama, N. Shimizu, and T. Furuta, *High-speed response of uni-travelling-carrier photodiodes*, Jpn. J. Appl. Phys. **36**, 6263 (1997)

[20] J.-W. Shi, Y-T. Li, C.-L. Pan, M.L. Lin, and Y.S. Wu, *Bandwidth enhancement phenomenon of a high-speed GaAs-AlGaAs based unitravelling carrier photodiode with an optimally designed absorption layer at an 830nm wavelength*, Appl. Phys. Lett. **89**, 053512 (2006)

[21] M. Piels, A. Ramaswamy, and J. E. Bowers, *A germanium on silicon unitravelling carrier photodiode*, in *Proceedings of the IEEE Photonics conference* (2011)

[22] M. N. Feiginov, *Analysis of limitations of terahertz p-i-n uni-traveling-carrier photodiodes*, J. Appl. Phys. **102**, 084510 (2007)

[23] A. T. Forrester, W. E. Parkins, and E. Gerjuoy, *On the possibility of observing beat frequencies between lines in the visible spectrum*, Phys. Rev. **72**, 728 (1947)

[24] E.R. Brown, *THz generation by photomixing in ultrafast photoconductors*, Int. J. High Speed Electron Syst. **13**, 497 (2003)

[25] A.T. Forrester, R. A. Gudmundsen, and P. O. Johnson, *Photoelectric mixing of incoherent light*, Phys. Rev. **99**, 1691 (1955)

[26] M. DiDomenico, R. H. Pantell, O. Svelto, and J. N. Weaver, *Optical frequency mixing in bulk semiconductors*, Appl. Phys. Lett. **1**, 77 (1962)

[27] S. Preu, *Tunable and continuous-wave Terahertz photomixer sources and applications*, J. Appl. Phys. **109**, 061301 (2011)

[28] G. Ducournau, P. Szriftgiser, T. Akalin, A. Beck, D. Bacquet, E. Peytavit, and J.F. Lampin, *Highly coherent terahertz wave generation with a dual-frequency Brillouin fiber laser and a 1.55 $\mu$m photomixer*, Opt. Lett. **36**, 2044 (2011)

[29] Claude Rulliere, *Femtosecond laser pulses: principles and experiments* (Springer, 2005)

[30] A. Beck, *Réalisation et charactérisation de photodiodes á transport unipolaire pour la génération d'ondes terahertz*, Ph.D Dissertation - University of Lille I (2008)

[31] T.Nagatsuma, H.Ito, and T.Ishibashi, *High-power RF photodiodes and their applications*, Laser & Photon. Rev. **3**, 123 (2008)

[32] N. Li, X. Li, S. Demiguel, X. Zheng, J. C. Campbell, D. A. Tulchinsky, K. J. Williams, T. D. Isshiki, G. S. Kinsey, and R. Sudharsansan, *High-saturation-current charge-compensated InGaAs-InP uni-traveling-carrier photodiode*, IEEE Photonic Tech. Lett. **16**, 864 (2004)

[33] P. J. Zampardi, D.-S. Pan, *Delay of Kirk effect due to collector current spreading in heterojunction bipolar transistors*, IEEE Electron Device Letters **17**, 470 (1996)

[34] Tadao Ishibashi, Tomofumi Furuta, Naofumi Shimizu, Koichi Nagata, Yutaka Matsuoka, and Masaaki Tomizawa, *American patent 5818096* (1998)

[35] T. Ishibashi, T. Furuta, H. Fushimi, S. Kodama, H. Ito, T. Nagatsuma, N. Shimizu, and Y. Miyamoto, *InP/InGaAs uni-traveling-carrier photodiodes*, IEICE Trans. Elecron. **E83-C**, 938 (2000)

[36] T. Yasui, T. Furuta, T. Ishibashi, and H. Ito, *Comparison of power dissipation tolerance of InP/InGaAs UTC-PDs and pin PDs*, IEICE Electron. Expr. **9**, 1 (2003)

[37] K. J. Williams and R. D. Esman, *Design considerations for high-current photodetectors*, J. Lightwave Technol. **17**, 1443 (1999)

[38] M. Chtioui, A. Enard, D. Carpentier, S. Bernard, B. Rousseau, F. Lelarge, F. Pommereau, and M. Achouche, *High-performance uni-traveling-carrier photodiodes with a new collector design*, IEEE Photonic. Tech. Lett. **20**, 1163 (2008)

[39] J.-W. Shi, F.-M. Kuo, C.-J. Wu, C.L. Chang, C.-Y. Liu, C.Y. Chen, and J.-I. Chyi, *Extremely high saturation current-bandwidth product performance of a near-ballistic uni-traveling-carrier photodiode with a flip-chip bonding structure*, IEEE J. Quant. Electron. **46**, 80 (2010)

[40] H. Ito, T. Furuta, F. Nakajima, K. Yoshino, and T. Ishibashi, *Photonic generation of continuous THz wave using uni-traveling-carrier photodiode*, IEEE J. Lightwave Tech. **23**, 4016 (2005)

[41] K. Kato, *Ultrawide-band/high frequency photodetectors*, IEEE Trans. Microwave Theory Techniques **47**, 1265 (1999)

[42] K. Kato, A. Kozen, Y. Muramoto, Y. Itaya, T. Nagatsuma, and M. Yaite, *110-GHz 50-% efficiency mushroom-mesa waveguide p-i-n photodiode for a 1.55 μm wavelength*, IEEE Photonic. Tech. Lett. **6**, 719 (1994)

[43] G. Unterborsch, A. Umbach, D. Trommer, and G. G. Mekonnen, *70 GHz long-wavelength photodetector*, in *Proceedings of European conference on optical communications* (1997)

[44] E. Rouvalis, C. C. Renaud, D. G. Moodie, M. J. Robertson, and A. J. Seeds, *Continuous wave terahertz generation from ultra-fast InP-based photodiodes*, IEEE Trans. Microwave Theory Techniques **60**, 509 (2012)

[45] K. S. Giboney, M. J. W. Rodwell, and J. Bowers, *Traveling-wave photodetector theory*, IEEE Trans. Microwave Theory Techniques **45**, 1310 (1997)

[46] J.-W. Shi, F.-M. Kuo, and M.-Z. Chou, *A linear cascade near-ballistic uni-traveling-carrier photodiodes with extremely high saturation-current bandwidth product (6825mA-GHz and 75mA/91GHz) under a 50ohm load*, in *Proceedings of the National Fiber Optic Engineers Conference* (2010)

[47] Y. Muramoto, H. Fukano, and T. Furuta, *A polarization-independent refracting-facet uni-traveling-carrier photodiode with high efficiency and large bandwidth*, J. Lightwave Technol. **24**, 3830 (2006)

[48] Simon Ramo et al., *Fields and waves in communication electronics - Third edition* (John Wiley & Sons, Inc., 1994)

[49] E. Rouvalis, C. C. Renaud, D. G. Moodie, M. J. Robertson, and A. Seeds, *Traveling-wave uni-traveling carrier photodiodes for continuous wave THz generation*, Opt. Exp. **18**, 11105 (2010)

[50] H.-J. Song, K. Ajito, Y. Muramoto, A. Wakatsuki, T. Nagatsuma, and N. Kukutsu, *Uni-travelling-carrier photodiode module generating 300 GHz power greater than 1 mW*, IEEE Microwave Wireless Compon. Lett. **22**, 363 (2012)

[51] A. Crocker, H. A. Gebbie, M. F. Kimmitt, and L. E. X. Mathias, *Stimulated emission in the far infra-red*, Nature **201**, 250 (1964)

[52] J. Farhoomand and H. M. Pickett, *Stable 1.25 watts CW far infrared laser radiation at the 119 $\mu$m methanol line*, Int. J. Infrared Millimiter Waves **8**, 441 (1987)

[53] P. Belland, *High power operation of a CW 28 $\mu$m water vapor laser*, Opt. Commun. **44**, 388 (1983)

[54] H. R. Fetterman, H. R. Schlossberg, and J. Waldman, *Submillimeter lasers optically pumped off resonance*, Opt. Commun. **6**, 158 (1972)

[55] T. K. Plant, L. A. Newman, E. J. Danielewicz, T. A. DeTemple, and P. D. Coleman, *High power optically pumped far infrared lasers*, IEEE Trans. Microwave Theory Techniques **22**, 988 (1974)

[56] P. Belland, *Waveguide CW 118.6 $\mu$m H2O laser*, Appl. Phys. B **27**, 123 (1982)

[57] P. Belland and D. Veron, *A compact cw HCN laser with high stability and power output*, Opt. Commun. **9**, 146 (1973)

[58] D. E. Evans, L. E. Sharp, B. W. James, W. A. Peebles, *Far-infrared superradiant laser action in methyl fluoride*, Appl. Phys. Lett. **26**, 630 (1975)

[59] J. Faist, F. Capasso, D. L. Sivco, C. Sirtori, A. L. Hutchinson and, A. Y. Cho, *Quantum cascade laser*, Science **264**, 553 (1994)

[60] F. Capasso, A. Y. Cho, J. Faist, A. Hutchinson, S. Luryi, C. Sirtori, and D. L. Sivco, *American patent 5457709* (1995)

[61] R. F. Kazarinov and R. A. Suris, *Possibility of amplification of electromagnetic waves in a semiconductor with a superlattice*, Sov. Phys. Semicond. **5**, 707 (1971)

[62] F. Capasso, C. Gmachl, D. L. Sivco, and A. Y. Cho, *Quantum cascade lasers*, Phys. Today May 34 (2002)

[63] Y. Bai, N. Bandyopadhyay, S. Tsao, S. Slivken, and M. Razeghi, *Room temperature quantum cascade lasers with 27 % wall plug efficiency*, Appl. Phys. Lett. **98**, 181102 (2011)

[64] S. Fathololoumi, E. Dupont, C. W. I. Chan, Z. R. Wasilewski, S. R. Lafranboise, D. Ban, A. Matyas, C. Jirauschek, Q. Hu, and H. C. Liu, *Terahertz quantum cascade lasers operating up to 200 K with optimized oscillator strength and improved injection tunneling*, Opt. Exp. **20**, 3866 (2012)

[65] G. Scalari, C. Walther, M. Fisher, R. Terazzi, H. Beere, D. Ritchie, and J. Faist, *THz and sub-THz quantum cascade lasers*, Laser & Photon. Rev. **3**, 45 (2009)

[66] P. Dean, M. Salih, S. P. Khanna, L. H. Li, N. K. Saat, A. Valavanis, A. Burnett, J. E. Cunningham, A. G. Davies, E. H. Linfield, *Resonant-phonon depopulation terahertz quantum cascade lasers and their application in spectroscopic imaging*, Semicond. Sci. Technol. **27**, 094004 (2012)

[67] A. Tredicucci, C. Gmachl, F. Capasso, D. L. Sivco, A. L. Hutchinson, and A. Y. Cho, *A multiwavelength semiconductor laser*, Nature **396**, 350 (1998)

[68] G. Scalari, L. Sirigu, R. Terazzi, C. Walther, M. Amanti, M. Giovannini, N. Hoyler, and J. Faist, *Multi-wavelength operation and vertical emission in THz quantum-cascade lasers*, J. Appl. Phys. **101**, 081726 (2007)

[69] Robert W. Boyd, *Nonlinear optics* (Academic press, 2008)

[70] P. A. Franken, A. E. Hill, C. W. Peters, and G. Weinreich, *Generation of optical harmonics*, Phys. Rev. Lett. **7**, 118 (1961)

[71] M. M. Choy, R. L. Byer, *Accurate second-order susceptibility measurements of visible and infrared nonlinear crystals*, Phys. Rev. B **14**, 1693 (1976)

[72] J. A. Armstrong, N. Bloembergen, J. Ducuing, and P. S. Pershan, *Interactions between light waves in a nonlinear dielectric*, Phys. Rev. **127**, 1918 (1962)

[73] I. Tomita, H. Suzuki, R. Rungsawang, Y. Ueno, and K. Ajito, *Analysis of power enhancement of terahertz waves in periodically inverted GaP pumped at 1.55 $\mu m$*, Phys. Stat. Sol. **204**, 1221 (2007)

[74] M. Scheller, J. M. Yarborough, J. V. Moloney, M. Fallahi, M. Koch and, S. W. Koch, *Room temperature continuous wave milliwatt terahertz source*, Opt. Exp. **18**, 27112 (2010)

[75] Bernard Epsztein, *French patent 1035379* (1959)

[76] Rudolf Kompfner and Calvin F. Quate, *American patent 2955223* (1960)

[77] G. P. Gallerano and S. Biedron, *Overview of terahertz radiation sources*, in *Proceedings of the 2004 FEL Conference* (2004)

[78] R. Warnercke, and P. Guenard, *Some recent work in France on new types of valves for the highest radio frequencies*, in *Radio Section* (1953)

[79] R. Kompfner, *Traveling-wave tubes*, Rep. Prog. Phys. **15**, 275 (1952)

[80] J. Bardeen and W.H. Brattain, *American patent 2524034* (1950)

[81] W. Shockley, *American patent 2569347* (1951)

[82] W. F. Brinkman, D. E. Haggan, and W. Troutman, *A history of the invention of the transistor and where it will lead us*, IEEE J. Sol. State Circ. **32**, 1858 (1997)

[83] C. A. Mack, *Fifty years of Moore's law*, IEEE Trans. Semicond. Manufact. **24**, 202 (2011)

[84] Frank Schwierz and Juin J. Liou, *Modern microwave transistors: theory, design and performance* (Wiley, New Jersey, 2003)

[85] M. Urteaga, R. Pierson, P. Rowell, V. Jain, E. Lobisser, and M. J. W. Rodwell, *130 nm InP DHBTs with ft > 0.52 THz and fmax > 1.1 THz*, in *69th Annual Device Research Conference (DRC), 2011 - 20-22 June* (2011)

[86] V. Radisic, D. Sawdai, D. Scott, W. R. Deal, L. Dang, D. Li, J. Chen, A. Fung, L. Samoska, T. Gaier, and R. Lai, *Demonstration of a 311-GHz fundamental oscillator using InP HBT technology*, IEEE Trans. Microwave Theory Techniques **55**, 2329 (2007)

[87] V. Radisic, X. B. Mei, W. R. Deal, W. Yoshida, P. H. Liu, J. Uyeda, M. Barsky, L. Samoska, A. Fung, T. Gaier, and R. Lai, *Demonstration of sub-millimiter wave fundamental oscillators using 35-nm InP HEMT technology*, IEEE Microw. Wireless Compon. Lett. **17**, 223 (2007)

[88] A. Maestrini, I. Mehdi, J. V. Siles, R. Lin, C. Lee, G. Chattopadhyay, J. Pearson, and P. Siegel, *Frequency tunable electronic sources working at room temperature in the 1 to 3 THz*, in *Proc. of SPIE Vol. 8496 84960F-1* (2012)

[89] A. Maestrini, I. Mehdi, J. V. Siles, J. S. Ward, R. Lin, B. Thomas, C. Lee, J. Gill, G. Chattopadhyay, E. Schlecht, J. Pearson, and P. Siegel, *Design and characterization of a room temperature all-solid-state electronic source tunable from 2.48 to 2.75 THz*, IEEE Trans. Terahertz Sci. Technol. **2**, 177 (2012)

[90] L. L. Chang and L. Esaki, and R. Tsu, *Resonant tunneling in semiconductor double barriers*, Appl. Phys. Lett. **24**, 593 (1974)

[91] M. Feiginov, C. Sydlo, O. Cojocari, and P. Meissner, *Resonant-tunneling-diode oscillators operating at frequencies above 1.1 THz*, Appl. Phys. Lett. **99**, 233506 (2011)

[92] S. Suzuki, M. Asada, A. Teranishi, H. Sugiyama and, H. Yokoyama, *Fundamental oscillation of resonant tunneling diodes above 1 THz at room temperature*, Appl. Phys.Lett. **97**, 242102 (2010)

[93] E. R. Brown, K. A. McIntosh, K. B. Nichols, and C. L. Dennis, *Photomixing up to 3.8 THz in low-temperature-grown GaAs*, Appl. Phys. Lett. **66**, 285 (1995)

[94] S. M. Duffy, S. Verghese, K. A. McIntosh, A. Jackson, A. C. Gossard, and S. Matsuura, *Accurate modeling of dual dipole and slot elements used with photomixers for coherent terahertz output power*, IEEE Trans. Microwave Theory Techniques **49**, 1032 (2001)

[95] E. Peytavit, S. Arscott, D. Lippens, G. Mouret, S. Matton, P. Masselin, R. Boquet, J. F. Lampin, L. Desplanque, and F. Mollot, *Terahertz frequency difference from vertically integrated low-temperature-grown GaAs photodetector*, Appl. Phys. Lett. **81**, 1174 (2002)

[96] M. Sukhotin, E. R. Brown, A. C. Gossard, D. Driscoll, M. Hanson, P. Maker, and R. Muller, *Photmixing and photoconductors measurements on ErAs/InGaAs at 1.55 $\mu m$*, Appl. Phys. Lett. **82**, 3116 (2003)

[97] G. Chattopadhyay, *Technology, capabilities, and performance of low power Terahertz sources*, IEEE Trans. Terahertz Sci. Technol. **1**, 33 (2011)

# Chapter 2

# Investigation of a low resistance, low absorption and thermally stable top-contact

Heat management is a critical issue in the operation of UTC-PDs driven under high optical powers. For the previous devices fabricated within the EPIPHY/THz Photonics group, heating has been proven the major cause of their failure. In the first part of the chapter, it will be presented an investigation of several metallic contacts over highly p-doped InGaAs layers to achieve a low specific contact resistance, a high reflectance at the interface between the metallic contact and the p-doped InGaAs layer and a good thermal stability for back-side illuminated UTC-PDs. In the second part, an alternative contact design will be introduced for front-side configurations in order to achieve a lower optical absorption at the metallic contact, a high transmittance, a good thermal stability and a low specific contact and series resistance.

## 2.1 Top-contact for back-side illuminated devices

In this section a survey of several metals of interest over highly p-doped InGaAs layers is presented. The aim is to find a suitable p-type ohmic contact with good electrical, thermal and optical properties.



 

### 2.1.1 Optical issues

As already underlined in the first chapter, illumination of UTC-PDs is one of the key aspects for their operation. The possibility of having light reflection at the top-contact increases the effective absorption region thickness without degrading the travelling time into it. Furthermore, due to the high optical powers employed (hundreds of mW) to generate large photocurrents (current densities of few hundreds of kA/cm$^2$), the top-contact may also absorb a large part of this power. For high-speed PDs the absorption region thickness has to be in the order of 100-150 nm to reduce the diffusion/drift time into it. The percentage of the absorbed light into the active region is roughly 10% for a width of 100 nm. This value is close to the absorbed power ratio by the best contact choice from an optical point of view: Au/$In_{0.53}Ga_{0.47}As$. However, such a contact has some drawbacks, in particular associated to the Au diffusion into InGaAs for high temperatures (above 250 °C) [1]. A strong heating of the PD can bring to the fusion of the metallic contact and its consequent destruction as it can be observed in the SEM picture of Fig. 2.1 for the UTC-PD fabricated in the previous thesis. In that case, the Ti/Pt/Au (20/40/600

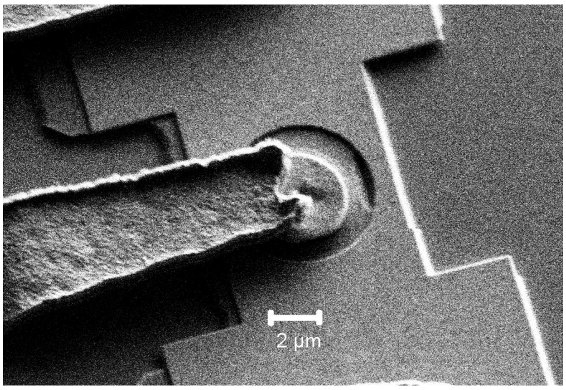


Fig. 2.1: SEM image of a UTC-PD fabricated in the previous thesis after destruction by a high injected optical power, from Ref. [2].

nm) top-contact employed over p-type $In_{0.53}Ga_{0.47}As$ was chosen to achieve good electrical properties, thermal stability and adhesion without consideration of the optical aspects. The reflectance associated to the composite contact is nearly 30% (calculated by a transfer matrix method [3]), while the remaining 70% is absorbed within few tens of nm from the InGaAs surface. In what follows other potential candidates as metallic contacts will be illustrated by presenting their different optical properties and, in the next subsection, their electrical properties over highly doped $In_{0.53}Ga_{0.47}As$.

#### 2.1.1.1 Choice of the metallic contacts

The choice of the metallic contacts has been done by considering their optical, electrical and thermal properties, and how these properties influence UTC-PDs' response. In particular, it should be noted that a contact with a high reflectivity could be more efficient than one with a low specific contact resistance because the increase in the external efficiency could compensate the fact of having a lower cut-off frequency due to the increase of the charge time $RC$. A parameter $\Gamma$ that represents the influence of contacts with different reflectivity and specific contact resistance can be defined in the following way

$$\Gamma = ((1 + Re^{-\alpha d})(1 - e^{-\alpha d}))^2 \frac{1}{1 + (2\pi\nu(R_L + R_S)C)^2} \tag{2.1}$$

where $R$ is the reflectance value and $R_S$ is the series resistance related to the contact, all the other parameters have been defined previously in chapter 1. The first squared term in parenthesis accounts for the Lambert-Beer law, while the latter for the $RC$ charge time. In Fig. 2.2 this parameter is plotted by considering an absorption width of 150 nm, a load resistance of 50 Ω and a capacitance of 11 fF on the overall response. These values are typical for high-frequency UTC-PDs. As it can be seen, for lower frequencies, it is preferable to have a higher reflectivity than a lower series resistance, while at higher frequencies the resistance related to the contact predominates the behavior. Furthermore, regarding the maximal RF power that can be generated, the possibility of absorbing less optical power is advantageous for driving UTC-PDs under higher input optical powers. However, it is worth to underline that a high contact resistance heats up the device for large photocurrents due to Joule effect and generates a drop voltage which obliges to increase the reverse bias voltage.

In Tab. 2.1 are reported the calculated reflectance values of several metals of interest over InP. The values have been calculated according to the Fresnel formula [4]

$$R = \left| \frac{\tilde{n}_s - \tilde{n}_m}{\tilde{n}_s + \tilde{n}_m} \right|^2 \tag{2.2}$$



 

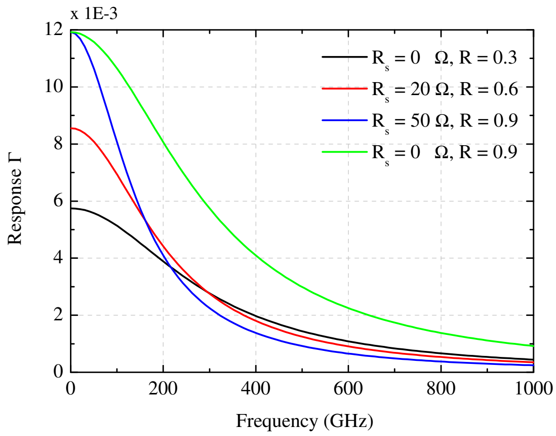


Fig. 2.2: Combined effect of the reflection at the metal contact and its resistance on the response of UTC-PDs.

Table 2.1: Optical properties of the most attractive metals and their reflectance value $R$ over InP and $In_{0.53}Ga_{0.47}As$.

| Metal | $n$ | $k$ | $R$ on InP (%) | $R$ on $In_{0.53}Ga_{0.47}As$ (%) | Wavelength ($\mu$m) | Ref. |
|---|---|---|---|---|---|---|
| Aluminum (Al) | 1.44 | 15.96 | 93.4 | 90.1 | 1.55 | [7] |
| Chrome (Cr) | 4.13 | 5.03 | 33.5 | 28.5 | 1.59 | [7] |
| Molibdenum (Mo) | 1.64 | 7.35 | 73.1 | 67.6 | 1.51 | [8] |
| Gold (Au) | 0.56 | 11.21 | 94.9 | 90.8 | 1.49 | [9] |
| Nickel (Ni) | 3.38 | 6.82 | 52.2 | 46.7 | 1.55 | [7] |
| Palladium (Pd) | 3.35 | 8.06 | 60.6 | 55.1 | 1.55 | [7] |
| Platinum (Pt) | 5.31 | 7.04 | 44.7 | 39.3 | 1.55 | [7] |
| Silver (Ag) | 0.15 | 11.85 | 96.2 | 91.5 | 1.61 | [9] |
| Titanium (Ti) | 4.04 | 3.82 | 23.2 | 19.0 | 1.55 | [7] |
| Tungsten (W) | 2.12 | 5.00 | 49.4 | 44.3 | 1.51 | [7] |

where $\tilde{n}_s$ and $\tilde{n}_m$ are the complex refractive indices for the semiconductor and the metal, respectively. The complex refractive indices of the different metals have been found in the literature to select firstly the potential candidates as metallic contacts. Even though in UTC-PDs the contact interface is with p-type InGaAs ($\tilde{n} = 3.55 - i0.12$), it is interesting to evaluate the reflectance also over InP ($\tilde{n} = 3.15$) due to the fact that the absorption region is much thinner than the wavelength. However, these two values do not change strongly as it can be seen in Tab. 2.1 [5, 6].

Here, we observe that only four metals present reflectance values higher than 70% for the InP case. Even though Au cannot be considered as a potential candidate due to its well-known diffusion in InGaAs as already discussed [1], no relevant information have been found regarding the other three metals (Al, Mo, Ag) on their diffusion or electrical properties over p-type InGaAs. However, Pd, Ti and Pt are known to be metals that form good electrical contacts over p-type InGaAs [10, 11]. Thus it may be worthy to investigate also these metals to obtain specific values for the final devices.

### 2.1.2 Contact resistance issues

In the first chapter, UTC-PDs have been modeled as current generators with a shunt capacitance and a series resistance (see Fig. 1.8). This resistance is actually associated to the proper resistance of the metal sheet and to the contact resistance at the interface between the metal and the semiconductor. This second contribution comes from the fact that the electrons/holes are located in the CB/VB and not at the Fermi level like the electrons in a metal. At the equilibrium, the bands bend in order to have the Fermi level aligned in both the materials and the vacuum level continuous across the interface. Band bending has a macroscopical effect on the electrical properties of the junction and two main behaviors on the I-V characteristic can be observed, namely Schottky-like and ohmic-like. Schottky-like contacts present an electrical characteristic analogous to that one of a diode, while ohmic-like ones behave electrically almost like a resistance. This second behavior is sought for UTC-PDs operation because the majority carriers in the semiconductor and the electrons in the metal have to move freely accross the junction for an opportune applied voltage without leading to voltage drops across the interfaces perturbing the device operation [12].

Three main mechanisms can be distinguished for the conduction through a metal/semiconductor interface, namely thermionic emission, thermionic-field emission (tunneling assisted) and field emission (pure tunneling). The transition between these different mechanisms can be observed schematically in Fig. 2.3. The ratio $k_BT/E_{00}$ with $E_{00} = (qh/4\pi)(N_s/m^*\epsilon_s\epsilon_0)^{1/2}$, with $N_s$ the doping level of the semiconductor, are responsible for the type of conduction mechanism [12]. In fact, for low doping levels (large depletion width regions and $k_BT/E_{00} >> 1$), in order to have an ohmic contact the thermal energy has to be sufficient to let the majority carriers overcome the barrier ($\rho_c \propto exp(q\phi_b/k_BT)$) [13]. For higher doping levels, apart from the thermionic emission, there is a contribution to the conduction current associated to the quantum tunneling[1] across the barrier and, for even higher doping levels ($k_BT/E_{00} << 1$), this contribution is predominant and the mechanism becomes purely tunneling leading, in the case of ohmic contacts, to $\rho_c \propto exp(q\phi_b/E_{00})$ [13]. Ohmic contacts can be obtained generally in three ways:

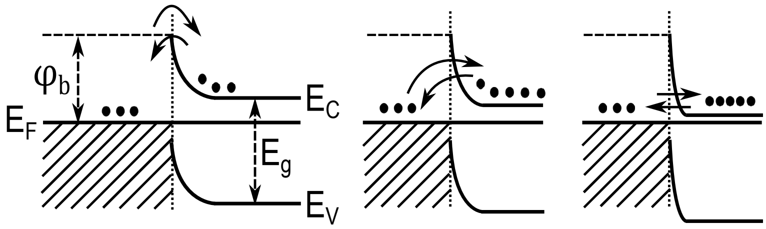


Fig. 2.3: Three different regimes of conduction depending on the doping level. From left to right: low, intermediate and high doping level for an n-semiconductor in depletion mode ($W_m < W_s$).

1. Choosing a metal with a work function $W_m = E_0 - E_F$ larger/lower than the work function $W_s = E_0 - E_{F_{p/n}}$ of the p-type/n-type semiconductor (accumulation mode) reported in Fig. 2.4.

2. Doping the semiconductor highly enough to allow tunnelling to be predominant.

3. Annealing the contact up to the formation of suitable alloys and/or to the diffusion of species at the interface.

In practice, the surface of a semiconductor is an important and usually limiting aspect in the formation of ohmic contacts. Localized states related to the abrupt interruption of the perfect periodicity of atoms at the surface can modify the Fermi level by pinning it. Due to the covalent nature of III-V semiconductors, the way to achieve ohmic contacts in practice consists in applying points 2) and/or 3) [12]. Moreover, potential oxide at the surface can deteriorate the properties of the contact by inibition of the tunneling phenomenon. It has been experimentally found that Pt, Pd and Ti present good values of $\rho_c$ for moderate dopings over p-type InGaAs

[1]Tunneling is a phenomenon typical of quantum mechanics consisting in the possibility for a particle (like an electron) to overcome a barrier whose energy is superior to the particle's energy [14].



 

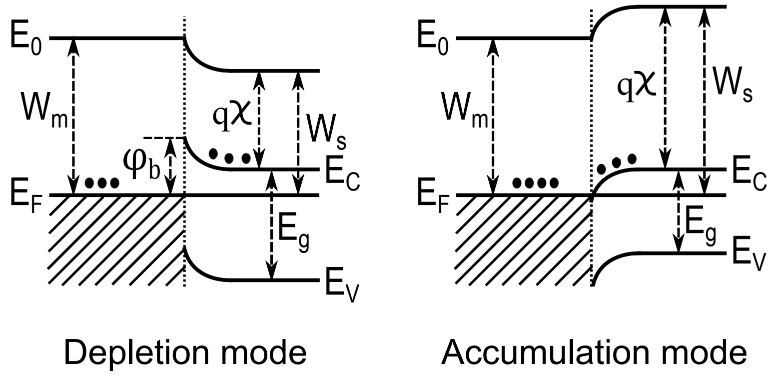


Fig. 2.4: Depletion and accumulation modes for an n-type semiconductor.

[11, 15, 16, 17, 10]. In particular, Ti contacts over p-type InGaAs have been obtained in the region $10^{-7}$-$10^{-8}$ $\Omega/\mathrm{cm}^2$ for doping levels close to $1{\cdot}10^{20}$ $\mathrm{cm}^{-3}$ with opportune annealing temperatures [18, 19]. However, even though Pt is not a common solution as first layer over p-type InGaAs, values of $\rho_c$ in the low $10^{-6}$ $\Omega/\mathrm{cm}^2$ have been obtained for doping levels of $4{\cdot}10^{19}$ $\mathrm{cm}^{-3}$ and annealing temperatures of 500°C in case of Pt/Ti/Pt/Au contacts [11]. In particular, the Pt/Ti/Pt/Au and the Pd/Ti/Pt/Au contacts have been shown in Ref. [11] to be superior in terms of $\rho_c$ to the more common Ti/Pt/Au contact over a large range of annealing temperatures and doping levels over p-type InGaAs.

#### 2.1.2.1 Fabrication

To study the electrical properties of the different metals an epitaxial structure from previous UTC-PDs epitaxial layers has been used. For what regards the electrical properties, the key part of the structure is the top-layer, in particular its doping level and composition. The relevant properties of the top-layer are a Be doping level of $8 \cdot 10^{19}$ $\mathrm{cm}^{-3}$ and a LM composition of $In_{0.53}Ga_{0.47}As$ over InP.

The fabrication consists in two principal steps. The first one (isolation) is the etching of a region all around the sample's surface where the metal will be deposited. This is necessary to avoid edge currents during the measurements. The second one consists in the deposition of metal pads inside the regions rounded by the isolation step as illustrated in Fig. 2.5. Patterns are transferred to samples by a technique called e-beam lithography. The principle consists in depositing by spin-coating (a technique to fabricate thin polymeric layers of controlled thickness) a resist sensitive to impinging high energy (acceleration voltage of 100 kV) electrons (Fig. 2.6 step 1). Then, the polymeric properties of the resist are modified during the patterning of the surface. After, by using an appropriate solvent, the resist is removed according to the pattern as defined during e-beam writing. Depending on the resist properties either the region that has been affected by the electron flow (positive writing) or its negative counterpart (negative writing) can be removed through a solution (Fig. 2.6 step 2). Such a resist pattern can be then used as a mask to permit the etching of the un-covered surface or to deposit metal patterns onto the sample's surface (Fig. 2.6 step 3). The main difference is that the sample is fully covered of metal deposited by e-beam evaporation instead of being etched. However, a bi-layer of resists has to be used for the metal deposition to have a suitable profile avoiding accumulation of metals at the borders of the patterns (see Fig. 2.6 step 3"). This profile is done by using resists with different sensitivity to the development process (Fig. 2.6 step 3'). The resist, after etching or metal deposition, is then removed by an appropriate solvent leading to a removal of the resist mask and, for metal deposition, unwanted metal deposited on top of it (lift-off technique). Chemical wet-etching through a solution consisting in deionized (DI) water ($H_20$), hydrogen peroxide ($H_2O_2$) and orthophosphoric acid ($H_3PO_4$) with a ratio 40:5:1 has been used to etch the InGaAs surface for a depth of around 150 nm [20]. Such a thickness is estimated sufficient to avoid contributions of edge currents in the measurements. After pattern writing and consequent development for metal deposition, the sample has been de-oxidized by a solution of sulfuric acid ($H_2SO_4$) and DI $H_20$ in ratio 1:20 to remove the oxide at the surface. Then, the sample has been clived in order to allow for different metal depositions. The metallizations, reported in the next section, have been deposited by e-beam evaporation. A flux of Ar ions (energy of 150 eV for 2 min) has been used to clean the surface from residual oxide, resist contamination and to improve metal adhesion just before metal evaporation.

#### 2.1.2.2 Measurements and analysis

Measurements of specific contact resistance have been performed using a four-wire sensing technique. This technique, illustrated schematically in Fig. 2.7, consists in applying a current between a pair of probes (force wires - A) through a current generator and in measuring the voltage drop with a second pair of probes (sensing



 

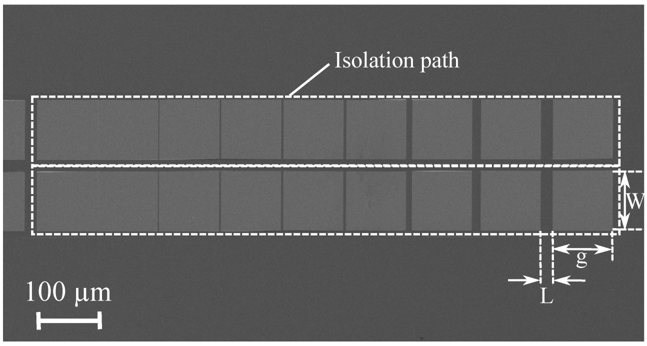


Fig. 2.5: SEM image of patterns to perform TLM measurements. The white dashed line indicates the etched border for the isolation.

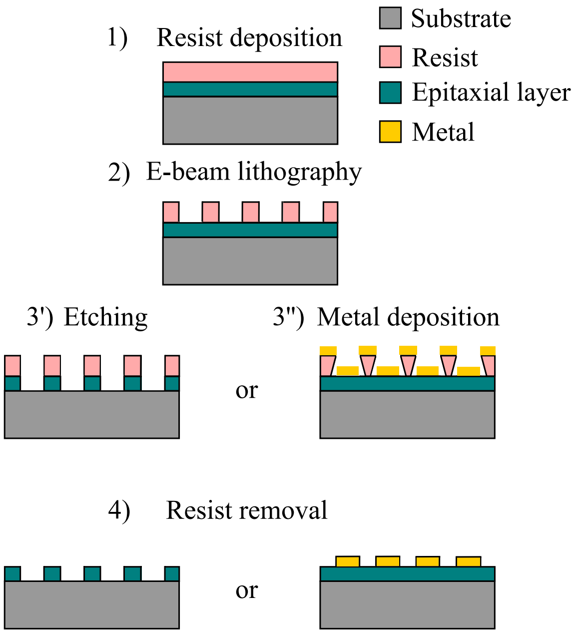


Fig. 2.6: Standard techniques used throughout the thesis to wet-etching semiconductors and depositing metal patterns.

wires - B) through a voltmeter. From the voltage drop and the current circulating, it is possible to obtain the value of the resistance $R = V/I$. The advantage of this method relies on the fact that the resistances associated to the contacts of the force wires are not measured by the sensing wires and those of the sensing wires are negligible due to the low current that passes through them (voltmeter principle). The technique used to extract the specific contact resistance of a metal/semiconductor interface is the transmission line method (TLM) [21]. It deals with the measure of the resistance between pads with different spacing lengths $L$ as shown in Fig. 2.5. By knowing $L$ and the width $W$ of the pads (see Fig. 2.5) two parameters can be obtained: the specific resistance of the underneath layer called sheet resistance $R_{\square}$ and the contact resistance value $R_c$ of the contacts as reported in the graph of Fig. 2.8 for the case of Mo. The resistance can be expressed as

$$R(L) = 2R_c + R_{\square}\frac{L}{W} \tag{2.3}$$

It is possible to show that, in the case of a lateral length $g$ for the pad superior to the transfer length $L_T$ that indicates approximately how far the current penetrates laterally below the pad, the following relation holds [22]

$$R_c = \frac{\sqrt{R_{\square}\rho_c}}{W} = \frac{R_{\square}L_T}{W} \tag{2.4}$$

where the specific contact resistance is given by

$$\rho_c = {L_T}^2 R_{\square} \tag{2.5}$$

In Tab 2.2 are reported the values measured of $\rho_c$ for the different metallizations considered. It can be noted that the best metals from the optical point of view (Al, Ag) present high specific contact resistances.

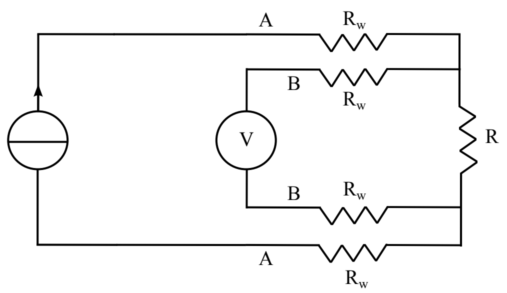


Fig. 2.7: Schematic of the 4-wire measurement technique.

In fact, if a contact surface of 7 $\mu$m$^2$ is considered, then the respective contact resistance, in the case of Ag, would be $R_c = 518.6\ \Omega$. For example, a device with a capacitance of 7.8 fF (for a 7 $\mu$m$^2$ and 100-nm-thick collector) would have a $\nu_{-3dB}$ related to the $RC$ pole of around 38.5 GHz. Values of $\rho_c$ in the order of $10^{-5}$ $\Omega$cm$^2$ cannot be accepted for high-speed PDs. A possible way to decrease the specific contact resistance is to anneal the contacts, however diffusion could dramatically



 

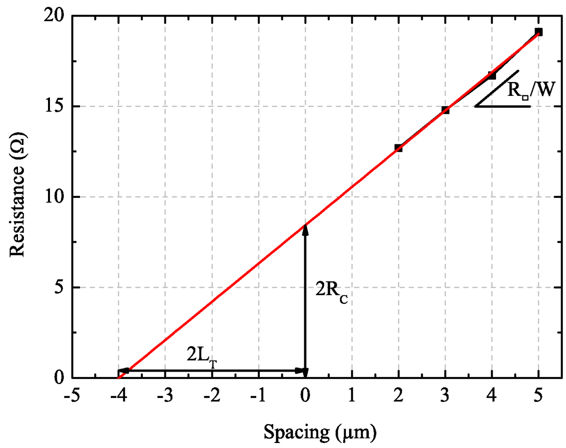


Fig. 2.8: Example of TLM measurements for the case of Mo.

Table 2.2: Specific contact resistances for the different metallizations studied.

| Metal stack | Thickness (nm) | $\rho_c$ ($\Omega$cm$^2$) | Type |
|---|---|---|---|
| Al | 300 | $9.6{\cdot}10^{-5}$ | ohmic |
| Ag | 300 | $3.6{\cdot}10^{-5}$ | ohmic |
| Mo/Pt/Au | 50/40/240 | $9.3{\cdot}10^{-6}$ | ohmic |
| Pt/Au | 10/300 | $5.3{\cdot}10^{-7}$ | ohmic |
| Ti/Pt/Au | 20/40/600 | $9.2{\cdot}10^{-7}$ | ohmic |

affect the properties of the active region underneath the anode contact and to ruin the abrupt interface and its optical properties. Pt and Ti are the only materials that present good electrical properties. However, their optical properties are not remarkable to be used as mirrors, particularly due to the optical absorption and consequent heating. In fact, a reflectance value at the interface Pt/InGaAs of 39.3% was already calculated in Tab. 2.1. This value is definetely too low for thin active regions (around 10% absorption for a 100-nm-thick region) because the majority of the optical power will be absorbed in the metal contact for back-side configurations (nearly 50% in this case). Thus, a new design needs to be found in order to avoid a strong heating of the device.



 

## 2.2 An alternative contact design for front-side illuminated configurations

In this section, a semi-transparent contact that provides low specific contact resistance, low absorption and thermal stability will be presented. This type of contact has a strong advantage in terms of illumination due to its front-side configuration. In fact, the alignment between the laser source and the device is much easier with respect to back or edge-side configurations. Even though, the response in this configuration can be lower than the one exploiting a reflection at the top-contact, it is possible by using diffraction orders to achieve high responsivities without heating up the device. Last but not least, this semi-transparent contact can be employed in resonant (Fabry-Pérot) configurations to increase further the responsivity.

### 2.2.1 Optical properties of sub-wavelength apertures

In recent years great attention from the scientific community has been spent to study and manipulate the properties of objects with features much smaller than their operation wavelength at which they work. The main reason is that new properties appear compared to the well-known ones of systems large compared to the wavelength. In particular, it has been experimentally demonstrated in 1998 by Ebbesen and co-workers that a periodic array of sub-wavelength apertures can transmit more than the unity close to the diffraction, once normalized to the aperture size, leading to the so-called extraordinary transmission (ET) phenomenon [23]. This result was not expected from previous electromagnetic (EM) theories of diffraction [24]. This discovery brought to new theoretical and computational approaches [25, 26, 27, 28]. Furthermore, several geometries of sub-wavelength arrays of apertures and particle-like shapes have found applications in sensors, photovoltaic cells, sub-wavelength optics, microscopy, bio-photonics etc. [29, 30, 31].

Arrays of apertures in a perfect electric conductor (PEC) sheet can have theoretical transmissions of 100% for suitable wavelength-depending dimensions. Even though PEC is an approximation, metals like Ag or Au behave quite similarly near optical frequencies. This aspect is crucial because it permits to employ array-based contacts achieving high transmission (low absorption) without being obliged to use a thin metal layer avoiding the light exponential decay in it. The design of the contact that will be presented in what follows has been done by considering firstly a quasi-analytical approach, the coupled-mode method (CMM), to obtain initial results for the design optimization [27]. Then, by using a software based on a finite element method (FEM), COMSOL Multiphysics, complementary results have been obtained for the final design.

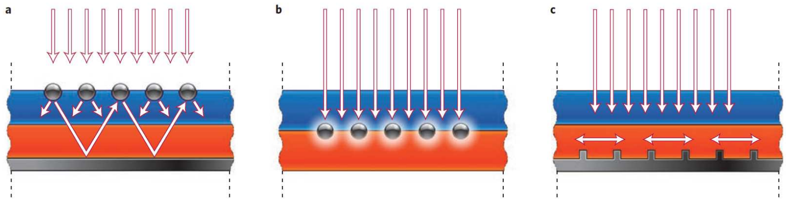


Fig. 2.9: Different mechanisms to increase the optical absorption by scattering and consequent increased optical path (a), by resonance excitation of nanoparticles (b) and by excitation of SPPs at the metal/dielectric interface (c) [31].

#### 2.2.1.1 Theoretical treatment with the coupled-mode method

A technique to treat the optical properties of arrays constituted by sub-wavelength apertures is the coupled-mode method (CMM) [27]. CMM is based on the expansion of the EM fields in eigenvalues for each region of the composite structure with the boundary conditions related to the matching of the electric and magnetic fields at the input and output interfaces. In homogenous regions the field is expanded in plane waves identified by wavevector $\mathbf{k}$ and polarization $\sigma$, while in the apertures in terms of waveguide modes. This approach can be applied to a wide range of structures as the one depicted in Fig. 2.10 under the condition that the impedance of the metal $Z_s = 1/\sqrt{\epsilon_M(\omega)}$ (within the CGS system) is high enough to consider valid surface impedance boundary conditions (SIBCs) [32]. In what follows the single-mode approximation will be introduced which accounts only for one mode (labelled with a subscript 0) propagating in the aperture. Such an approximation is particularly valid for wavelengths close to the periodic lattice period [32]. Under this condition, it can be demonstrated that the following system of equations holds

$$(G_{00} - \Sigma_0)E - G_0^V E' = I_0 \tag{2.6}$$

$$(G'_{00} - \Sigma_0)E' - G_0^V E = 0 \tag{2.7}$$



 

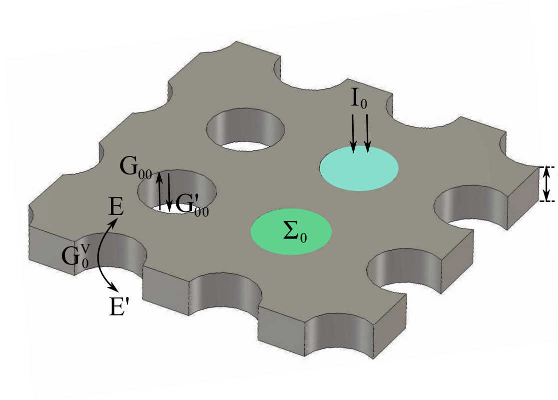


Fig. 2.10: Example of a structure that can be treated within the coupled-mode method. The parameters indicated are associated with Eqs. 2.6 and 2.7.

where $G_{00}$ and $G^{'}_{00}$ are called propagators and represent the coupling between the scattering of the waveguide mode in itself at the interface with medium 1 and 3, respectively (see Fig. 2.11). $E$ and $E^{'}$ represent the modal amplitudes of the electric fields associated to the waveguide mode at the interface with medium 1 and 3, respectively. $I_0$ is the illumination term which describes the coupling between the impinging plane wave identified by the parallel component $\boldsymbol{k_0}$ of its wavevector and polarization state $\sigma_0$ and the waveguide mode in the aperture. $G_0^V$ and $\Sigma_0$ are associated with the coupling of the electric fields and the reflection contributions at the two sides of the aperture, respectively. This set of equations is sufficient to obtain the electric field everywhere once known the modal amplitudes $E$ and $E^{'}$. This issue is the reason for which CMM is more efficient in terms of other approaches like multipoles calculations or the transfer matrix method [32].

In Fig. 2.11 are reported the different scattering processes at the two interfaces 1-2 and 2-3. In the next, the quantities without a capital letter refer to the electric field magnitudes. At the first interface the impinging plane wave ($\boldsymbol{k_\omega}$,$\sigma_0$) is partially reflected ($\rho_{12}^{\boldsymbol{k},\sigma}$) and partially transmitted into the waveguide mode of the aperture ($\tau_0^{12}$). In the aperture the wave propagates with wavevector $q_0$ (coinciding with the vacuum one for normal incidence) for a distance $h$ ($\mathrm{e}^{iq_0h}$) and then gets partially reflected back into the waveguide mode ($\rho^{23}$) and partially transmitted as a propagating plane wave into free space ($\tau_{\boldsymbol{k},\sigma}^{23}$). The reflected wave at the interface 2-3 propagates back in the hole ($\mathrm{e}^{iq_0h}$) up to the interface 2-1 where it is partially reflected back ($\rho^{21}$) and partially transmitted ($\tau_{\boldsymbol{k},\sigma}^{21}$). This process of bouncing back

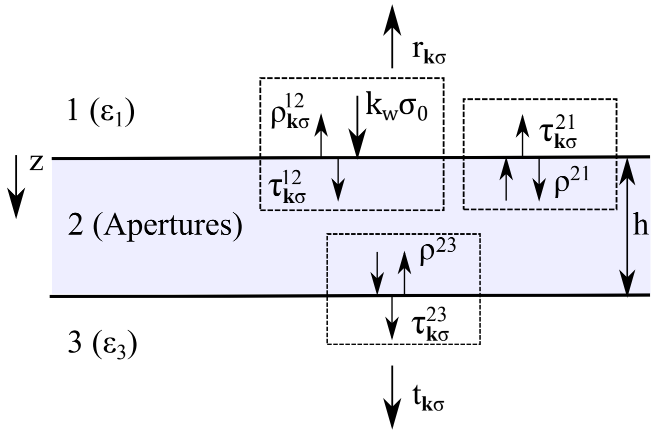


Fig. 2.11: Schematic representation of the different processes and associated parameters.

and forth is analogous to a classical Fabry-Pérot cavity. The sum of all the infinite scattering contributions at the interface 2-3 gives the transmission coefficient $t_{\boldsymbol{k},\sigma}$ as the sum of a geometrical series

$$t_{\boldsymbol{k},\sigma} = \frac{\tau_0^{12} e^{iq_0 h} \tau^{23}_{\boldsymbol{k},\sigma}}{1 - \rho^{12}\rho^{23} e^{2iq_0 h}} \tag{2.8}$$

For the reflection coefficient, due to the asimmetry in the illumination of the structure the zero-order coefficient $r_{\mathbf{0},\sigma_0}$ is given by

$$r_{\mathbf{0},\sigma_0} = r_{\boldsymbol{k_0},\sigma_0} + \frac{\tau_0^{12} e^{2iq_0 h} \rho^{23} \tau^{21}_{\mathbf{0},\sigma}}{1 - \rho^{12}\rho^{23} e^{2iq_0 h}} \tag{2.9}$$

while the general coefficient $r_{\boldsymbol{k},\sigma}$ with $\boldsymbol{k} \neq 0$ is given by

$$r_{\boldsymbol{k},\sigma} = \frac{\tau_0^{12} e^{2iq_0 h} \rho^{23} \tau^{21}_{\boldsymbol{k},\sigma}}{1 - \rho^{12}\rho^{23} e^{2iq_0 h}} \tag{2.10}$$

In order to find the total transmittance T and reflectance R, we need to sum the contributions of the different plane waves (diffraction orders) accounting for their polarization state

$$T = \sum_{\boldsymbol{k},\sigma}^{pr} Y_3^{\boldsymbol{k},\sigma} \left| t_{\boldsymbol{k},\sigma} \right|^2, R = \sum_{\boldsymbol{k},\sigma}^{pr} Y_1^{\boldsymbol{k},\sigma} \left| r_{\boldsymbol{k},\sigma} \right|^2 \tag{2.11}$$

where the sum runs over polarization states $\sigma$ and plane waves with parallel component $\boldsymbol{k} = \boldsymbol{k_0} + \boldsymbol{K_R}$ with $\boldsymbol{k_0}$ the parallel component (to the surface) of the initial impinging plane wave $\boldsymbol{k_\omega}$ and $\boldsymbol{K_R}$ a wavevector of the reciprocal lattice. $Y_3^{\boldsymbol{k},\sigma}$ is the admittance of the plane wave in medium 3 with $Y_{1/3}^{\boldsymbol{k},s} = k_z/k_\omega$ for s-polarization (TE modes) and $Y_{1/3}^{\boldsymbol{k},p} = \epsilon_{1/3}k_\omega/k_z$ for p-polarization (TM modes) where $k_\omega = 2\pi/\lambda_0$ and $k_z = \sqrt{\epsilon_{1/3}k_\omega^2 - |k|^2}$. *pr* means that the sum runs only over the propagating modes for which $k_z$ is not imaginary.

Even though this approach permits to treat general apertures, the focus will be on a specific problem consisting of an array of slits over a substrate as represented in Fig. 2.12. The reason is that an array of slits can be designed and fabricated with a certain degree of freedom and can achieve a high transmission under normal incidence for p-polarized light (see Fig. 2.12) with a covered surface that can be as high as 50% (in the considered case) of the total illuminated one. In the case studied the impinging electric field is perpendicular to the slits with parallel component (along x-axis), $k_0$, equal to zero (p-polarized). Some approximations can be used in this case to treat more easily the problem [32]:

1. Only the $TM_{00}$ mode of the slit (TEM mode) is considered in the propagation which is valid for wavelengths close to the diffraction (single-mode approximation).

2. The substrate is lossless and infinitely thick.

3. The metal grid is treated as a PEC.

The choice of the last approximation will be explained later on. For simplicity the subscript 0 will be removed for the single-mode approximation. The coefficients in Eq. 2.8 can be related to those in Eqs. 2.6 and 2.7 by matching the electric fields at the two interfaces. The coefficients $\tau^{12}$ and $\tau_{\boldsymbol{k},p}^{23}$ are given by

$$\tau^{12} = \frac{I}{G+i}, \tau_{\boldsymbol{k},p}^{23} = \frac{2i \langle \boldsymbol{k}|0\rangle}{G'+i} \tag{2.12}$$

where $I = 2iY_1^{\boldsymbol{k},p} \langle k_0|0\rangle$ with $\langle k_0|0\rangle$ the overlap integral (with the Dirac notation) between $k_0$ and the fundamental mode $TM_{00}$. The generical overlap integral $\langle \boldsymbol{k}|\alpha\rangle$ has to be evaluated in the following way

$$\langle \boldsymbol{k}|\alpha\rangle = \int d\boldsymbol{r} \, \langle \boldsymbol{k}|\boldsymbol{r}\rangle \, \langle \boldsymbol{r}|\alpha\rangle \tag{2.13}$$



 

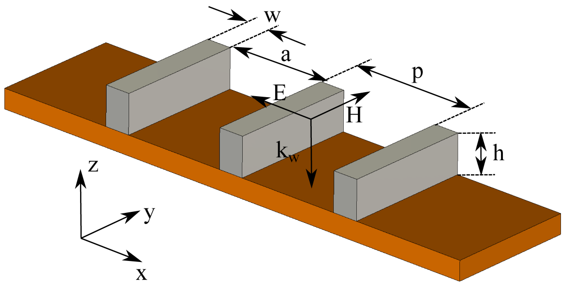


Fig. 2.12: Geometry for the contact with plane wave impinging normally to the array. The slits are infinitely long in y direction and periodic in x direction. The substrate extends to z $\rightarrow -\infty$.

where $\langle \boldsymbol{k}|\boldsymbol{r}\rangle$ and $\langle \boldsymbol{r}|\alpha\rangle$ are the plane wave $\langle \boldsymbol{k}|$ and waveguide mode $\langle \alpha|$ wavevectors evaluated in the real space. In the case of slit apertures and single-mode approximation ($\alpha = 0$) the overlap integral is equal to

$$\langle \boldsymbol{k}|0\rangle = \sqrt{\frac{a}{p}}\frac{\sin ka/2}{ka/2} \tag{2.14}$$

where $a$ and $p$ are the slit aperture's width and the lattice period, respectively (see Fig. 2.12). The propagator $G$ is given by

$$G = i\sum_{\boldsymbol{k}}\left(Y_1^{\boldsymbol{k},p}\right)|\langle 0|\boldsymbol{k}\rangle|^2 \tag{2.15}$$

where $G^{'}$ has an equivalent expression with $Y_3^{\boldsymbol{k},p}$ instead of $Y_1^{\boldsymbol{k},p}$. The coefficients $\rho^{12}$ and $\rho^{23}$ are given by

$$\rho^{12} = -\frac{G-i}{G+i}, \rho^{23} = -\frac{G^{'}-i}{G^{'}+i} \tag{2.16}$$

Finally, the coefficient $r_{\boldsymbol{k_0},\sigma_0}$ is given by [27]

$$r_{\boldsymbol{k_0},\sigma_0} = \frac{i(1-2a/p)+G}{i+G} \tag{2.17}$$

The quantities $\Sigma_0$ and $G_0^V$ of Eqs. 2.6 and 2.7 are already taken into consideration in the transmission coefficient expression (Eq. 2.8). In Fig. 2.13 is plotted the total transmittance of an array of slits within the PEC approximation for different values of the thickness $h$ of the slits. This graph has been used to firstly check that the model was implemented correctly (see Fig. 15 of ref. [32]). It can be observed that maxima appears close to the diffraction limit ($\lambda = p$) achieving 100% of transmission. In this case the total transmittance consists of diffraction orders 0 and $\pm 1$ (below $\lambda = p$). Minima are related to the divergence of the admittance $Y_{1/3}^{\boldsymbol{k},p}$ in the propagator $G \equiv G'$ for the condition $k_z = \sqrt{k_\omega^2 - |k|^2} = 0$. The channel related to the thickness of the slits couples to the one of the coherent diffraction and, depending on $h$, can provide different features in the frequency spectrum as reported in Fig. 2.13. This is strictly correlated to the Fabry-Pérot resonances within the slits according to the divergence of the transmission coefficient in Eq. 2.8 for $|\rho^{12}| = |\rho^{23}| = \mathrm{e}^{|q_0|h}$ and, for $h > p$, related to the condition $\cos k_\omega h = \pm 1$ [32]. The PEC approximation (point 4)) could be removed by considering an artificial larger size of the apertures/slits associated to the penetration depth $\delta$ of the electric field into the metal ($\delta$ = 22 nm for Au at 1.55 $\mu$m). The main change in the formulation is related to the propagator $G$ where the previous condition $k_z = 0$ is substituted by $k_z + k_\omega Z_s = 0$. This condition is formally equivalent to that one for surface plasmons propagation on a flat metal surface within the SIBCs approximation.

## 2.2.2 Design of the top-contact

Different parameters have to be taken into consideration, even for simple structures such as a 1D array of slits. Furthermore, it is worth to notice that the conceived structure has to be also feasible from a fabrication point of view. This issue adds some constraints on the freedom degrees related to the thickness of the strips and their aperture's width. In what follows a good compromise will be presented between the different design parameters.

### 2.2.2.1 Electromagnetic aspects

The geometry has been chosen to maximize the absorption in the semiconductor and to minimize that one in the contact without penalizing the responsivity, but providing a large enough surface to have a low contact resistance. It consists of a 1D array of slit apertures that, for the final device, will be short-circuited at one end in order to collect the carriers. A Pt/Au metal sequence can be used for the strips. The Pt layer (50 nm) acts as barrier for Au diffusion and decreases the specific contact resistance as already discussed before, while the Au layer lowers the series resistance



 

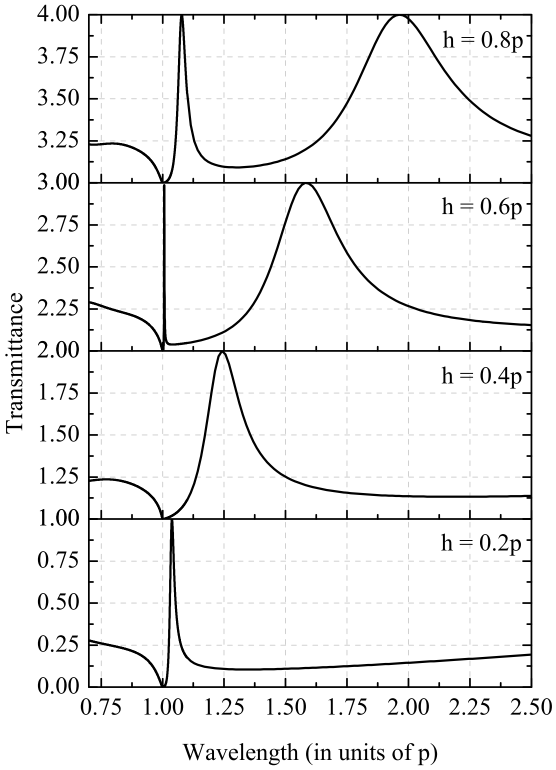


Fig. 2.13: Total transmittance under normal incidence of a 1D array of slits with aperture $a = 0.2p$ and different thicknesses $h$ as a function of the normalized wavelength in the PEC approximation with no substrate. Curves are shifted vertically by $+1$ for clarity.

and behaves similarly to a perfect metal at infrared frequencies. For this reason the treatment will be done within the PEC approximation. The results will be compared with a commercial software (COMSOL Multiphysics) based on the finite element method (FEM) [33]. The software will be employed also to evaluate with precision some aspects that cannot be treated by CMM like different types of metals forming the strip metallization, power loss density in the underneath layer (active region) for non-perfect metals and finite size of the contact. All these aspects are secondaries for the design as it will be shown later on. Moreover, they may confuse at the beginning due to the already complex physics of the system. This is the principal reason for which in the first part of the analysis only CMM is used.

The first thing to be considered is that the $In_{0.53}Ga_{0.47}As$ underneath layer (infinitely thick as approximation) presents a refractive index $\tilde{n} = 3.55 - i0.12$ different from one. Here, the imaginary part of the permittivity will be not included due to its negligible value compared to the real part for transmittance calculation. The imaginary part will be considered for the calculation of the electromagnetic power dissipated in the structure later on. The high permittivity of the substrate is a fundamental aspect because it allows to excite different surface waves (PEC approximation) or surface plasmon (SIBCs approximation) orders, while avoiding reflection of propagative diffraction orders at the interface air/array. The condition to satisfy is to have a lattice period $p$ smaller than the impinging vacuum wavelength $\lambda_0$ of illumination. The reason is that the first orders of diffraction in air appear at $\lambda_0 = p$, while in the semiconductor at $\lambda = \lambda_0/n = p$, thus it is preferable to find a vacuum wavelength in the range $[p, p{\cdot}n]$.

Two ways which could be used to realize high aspect-ratio slits with sub-$\mu$m dimensions consist in focused ion beam (FIB) and e-beam lithography techniques. However, as it will be shown in the next chapter, the FIB technique is not suitable for UTC-PDs because it damages the epitaxial layers. Thus, in what follows, the constraints associated with the e-beam lithography technique will be taken into account for the design.

In Figs. 2.14, 2.15, 2.16 and 2.17 are reported the transmittances for different slit widths $a$ as a function of the lattice period $p$ and the thickness $h$ calculated with CMM. The range for $p$ starts for all the graphs at the value $a$ for which no grid is present over the semiconductor surface and the transmittance calculated through the Fresnel formula is 68.6%. The upper limit at 1.5 $\mu$m is to avoid diffraction as already said previously. The range for $h$ starts at 0 which means an infinitely thin grid and finishes at 1 $\mu$m. The upper limit is related to the fact that problems associated to the resist deposition like inhomogeneous covering during subsequent steps of UTC-PD fabrication may appear for thick grids. Even though resist thickness may be increased to few $\mu$m, problems can arise during some fabrication steps (i.e. air-bridge) as it will be discussed in more details in the next chapter. Designs that present red regions can be argued as the best choices, but not all of them are technologically feasible. In fact, for small apertures (Fig. 2.14) $h$ should be at least 300 nm. This means to have resist patterns with an aspect-ratio of 450/50 = 9 (taking into account a factor 1.5 between the resist thickness and the metal one) which is extremely difficult to achieve in practice. The reason can be found by considering Fig. 2.18 which depicts the best configuration to achieve high-quality



 

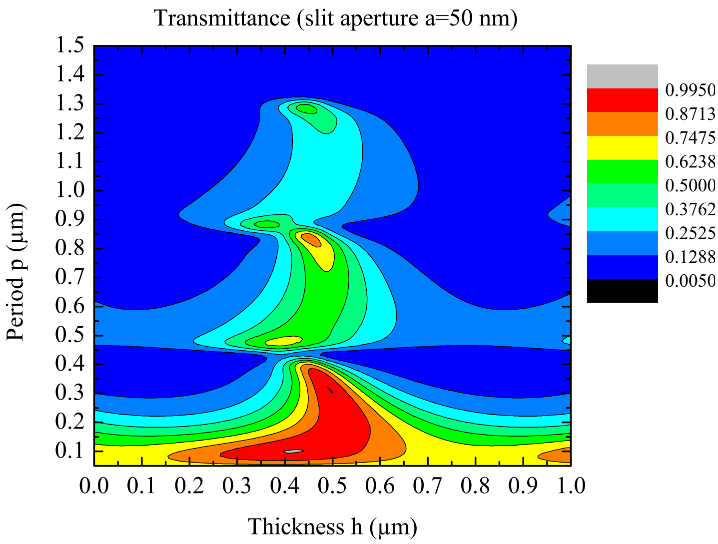


Fig. 2.14: Total transmittance at $\lambda = 1.55$ $\mu$m of a 1D array of slits with aperture $a = 50$ nm as a function of $h$ and $p$.

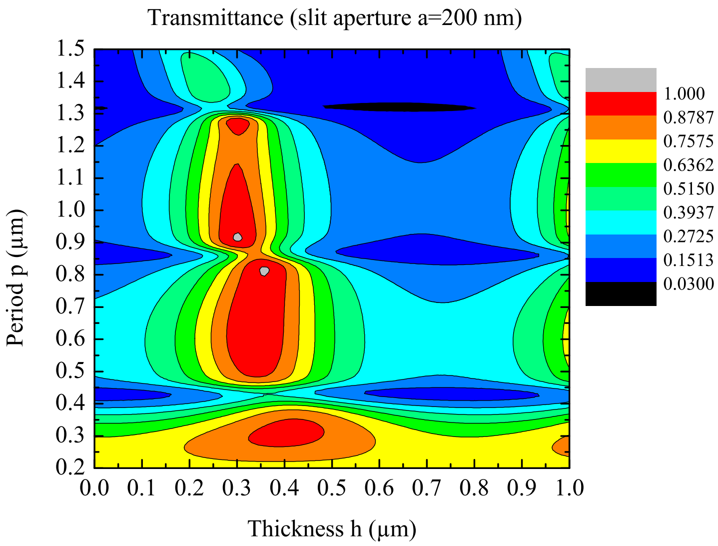


Fig. 2.15: Total transmittance at $\lambda = 1.55$ $\mu$m of a 1D array of slits with aperture $a = 200$ nm as a function of $h$ and $p$.

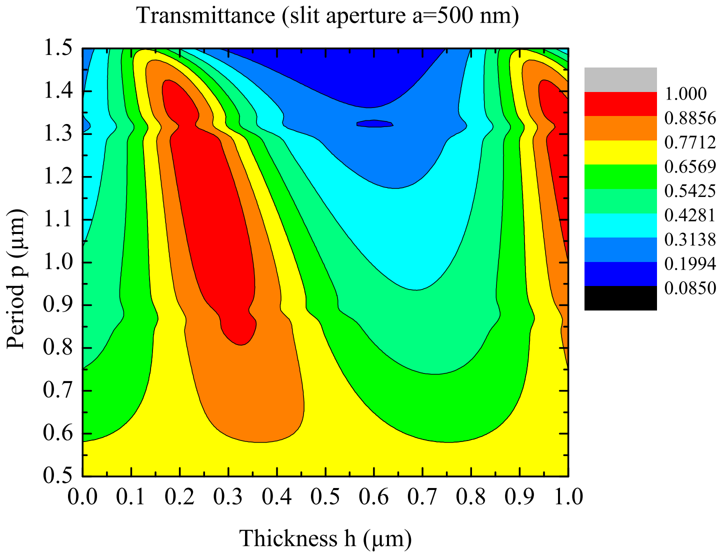


Fig. 2.16: Total transmittance at $\lambda = 1.55$ $\mu$m of a 1D array of slits with aperture $a = 500$ nm as a function of $h$ and $p$.

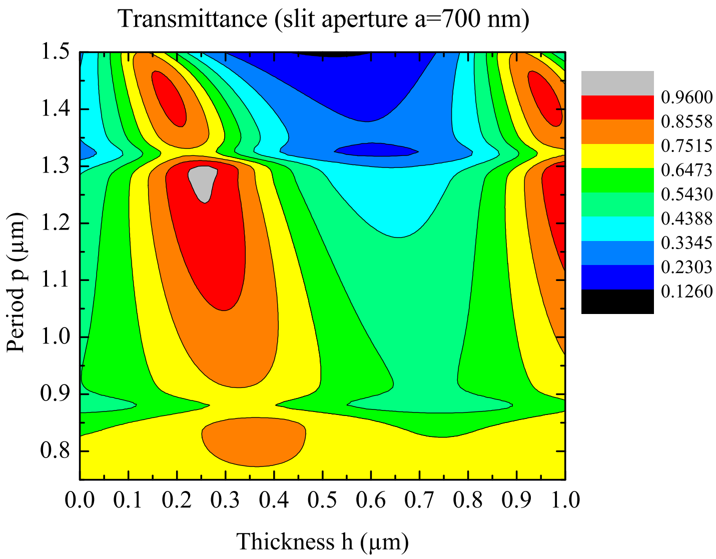


Fig. 2.17: Total transmittance at $\lambda = 1.55$ $\mu$m of a 1D array of slits with aperture $a = 700$ nm as a function of $h$ and $p$.



 

metal strips. In this case the width $w$ of the strips is almost constant all along their thickness $h_2$. This can be achieved only by having $h_1 > h_2$ due to the possibility of having a suitable profile as already discussed above. However, during the development of the exposed resist (after e-beam lithography) the solution tends to etch the resist2 (see Fig. 2.18) that was not intentionally exposed. The reasons is mainly the retro-diffusion of electrons during e-beam lithography. This aspect is critical for small and repetitive patterns when thicker resists are used due to longer times of development. The result is that $a_1$ becomes much smaller than $a_2$ with the potential consequence of pattern mechanical instability. For an aperture $a = 200$ nm (Fig. 2.15) the same problem appears again, but the aspect-ratio is reduced to around 2.25 (same criterion as before). However, using design parameters of $p = 1$ $\mu$m, $h = 300$ nm and $a = 500$ nm seems to be the best solution because a transmittance close to 1 (see Fig. 2.16) can be achieved with an aspect-ratio of 0.9 which is reasonable for the fabrication of high-quality strips as it will be confirmed and shown in the next chapter. Another feature of this set of parameters is that the degree of tolerance is larger than for the other ones as it can be observed by the extension of the red regions around the optimal choices. Finally, in Fig. 2.17 it can be noticed that the maximal transmittance value shifts towards larger periods i.e. 1.1-1.2 $\mu$m and achieves only 83% at $p = 1$ $\mu$m and $h = 300$ nm. Thus, there is no advantage in using such a large aperture as the period has to be increased too, but for a given finite size condition this means a lower number of slits and less transmission as it will be explained better below. From this analysis the optimal parameters that have been chosen are $w = 500$ nm, $p = 1$ $\mu$m and $h = 300$ nm (see Fig. 2.16). These dimensions are compatible with photomixing at 1.55 $\mu$m. Finally, recalling the results on the specific contact resistance for Pt, $\rho_c = 5.3 \cdot 10^{-7}$ $\Omega$cm$^2$, the chosen ratio $a/p$ gives half of the surface covered and a contact resistance of a few $\Omega$ for a 3-$\mu$m-side device which is reasonable for high-speed PDs. The series squared resistance (related to the bulky strips) of the contact is negligible due to the thickness of the strips, in fact a simple calculation of its resistance (considering a 300-nm-thick Au layer) using an Au bulk resistivity of $\rho_{Au} = 2.46{\cdot}10^{-8}$ $\Omega$m leads to an equivalent sheet resistance $R_\square = 0.16$ $\Omega$.

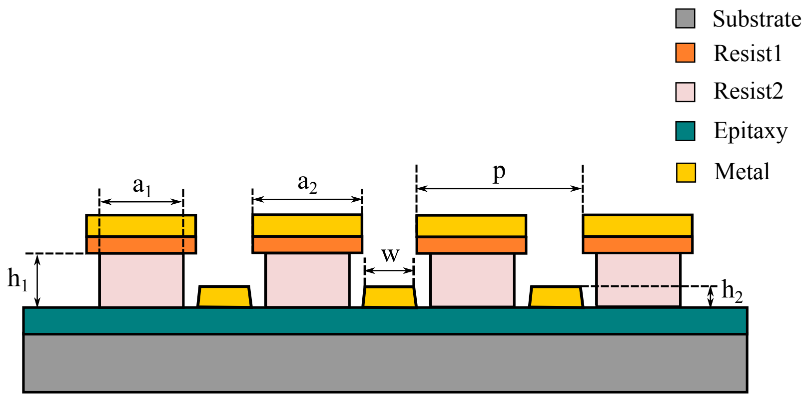


Fig. 2.18: Example of a good compromise between the period $p$, the strips' width $w$ and the thickness $h_2$ for the resist pattern parameters $a_1$, $a_2$ and $h_1$.

#### 2.2.2.2 Comparison with a finite element method

In order to develop a more accurate and precise model of the real contact, a comparison has been firstly established between the quasi-analytical results of Fig. 2.16 and the computational results obtained by COMSOL Multiphysics. The 2D model, reported in Fig. 2.19, consists in:

- Periodic ports at a distance of 1.5 vacuum wavelengths from the interface air/array and array/semiconductor, respectively.
- Periodic boundary conditions normally to the array on the left and right sides of the unit cell.
- Quasi-PEC approximation achieved by inserting a large extinction coefficient $k = 10^8$ and a real refractive index $n = 0$ (for technical reasons of the software).
- Mapped mesh with maximal element size of 20 nm.
- Plane wave excitation with a nominal optical power of 1 W.
- Diffraction orders computed automatically.

In Fig. 2.20(a) are reported the transmittances of an array of slits with the optimal parameters of the previous section (see Fig. 2.16) as a function of the wavelength. It is worth to notice that only half of the power is transmitted into the zero order of diffraction, while the other half is shared between the $\pm 1$ orders.



 

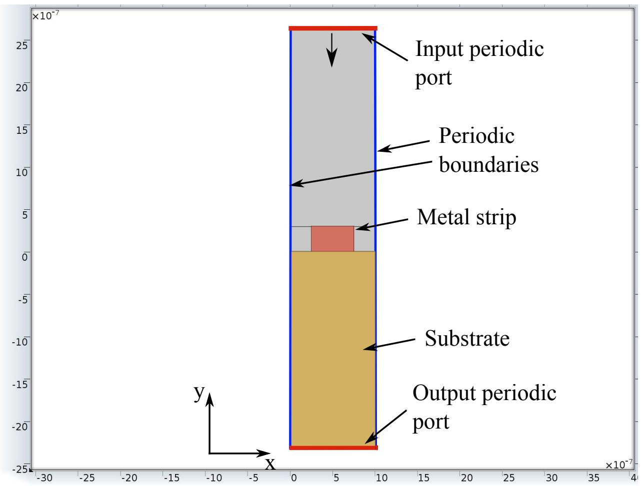


Fig. 2.19: Schematic of the model implemented in COMSOL Multiphysics to calculate the transmission of the grid contact. The impinging electric field is parallel to the x-axis.

Even though the second order $m = 2$ could be excited for $\lambda < pn/m = 1 \cdot 3.55/2 = 1.775$ $\mu$m, the overlapping integral ($\langle 4\pi/p|0\rangle$) is zero for $a/p = 0.5$ regardless of the wavelength (see Eq. 2.14). The deeps are associated to the diffraction condition as already discussed before. A total transmittance of 96% can be achieved at 1.55 $\mu$m. As it can be observed in Fig. 2.20(b), the results agree well with those of Fig. 2.20(a). In particular, a transmittance value of 91.3% is achieved at 1.55 $\mu$m close to the 96% previously calculated. However, in the region between the two diffraction minima ($\lambda = p = 1$ $\mu$m and $\lambda = pn/3 = 1.18$ $\mu$m), the transmittance curve obtained by simulation is above the quasi-analytical one. Such a problem is not really important due to the fact that the range of interest is located at larger wavelengths in which the curves agree pretty well and over a large range of wavelengths (useful for fabrication tolerances). Finally, it can be noticed that a slight difference is present between the theoretical and the simulated curves. The physical reason is related to $\pm 2$ diffraction orders which are present at $\lambda = pn/2 = 1.775$ $\mu$m in the quasi-PEC condition (see Eq. 2.15). However, the difference is quite low ($< 2\%$ at 1.775 $\mu$m) and does not constitute a problem for the results at 1.55 $\mu$m. The overall good agreement over almost all the frequency range, especially far from the diffraction makes trustful the next results and, in particular, the settings chosen for the simulations. In Fig. 2.21 are shown the x-component and the y-component of



 

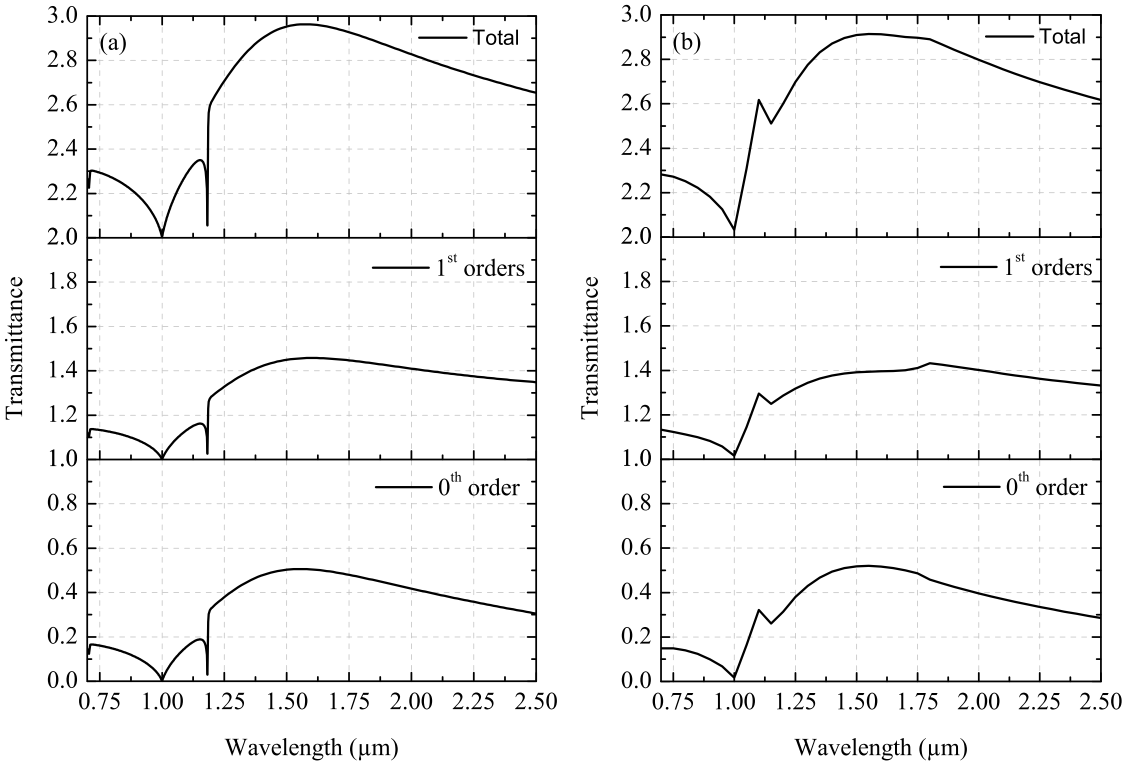


Fig. 2.20: Transmittance of the different orders as a function of the wavelength for an array with parameters $w = 0.5$ nm, $p = 1$ $\mu$m and $h = 300$ nm calculated with CMM (a) and with COMSOL (b) for a PEC and quasi-PEC approximations. The curves for the sum of the $\pm 1^{st}$ diffraction orders and for the total transmittance are shifted by +1 for clarity.

the electric field, $E_x$ and $E_y$ respectively for the simulation of Fig. 2.20(b). Here, it is interesting to observe two main features peculiar of sub-wavelength apertures. Firstly, $E_x$ is higher within the apertures with respect to the impinging plane wave field and, after few wavelengths far from the apertures, the electric field achieves once again a plane wave-like distribution. Secondly, $E_y$ shows the typical dipole-like behavior close to the strip surface indicating that surface waves (SPPs cannot propagate in the PEC approximation) are present.

The next step towards a more realistic model deals with the removal of the PEC approximation. Firstly, a 300-nm-thick Au strip is considered with an Au permittivity given by a Drude model

$$\epsilon = 1 - \frac{\omega_p^2}{\omega^2 + i\omega\omega_\tau} \tag{2.18}$$



 

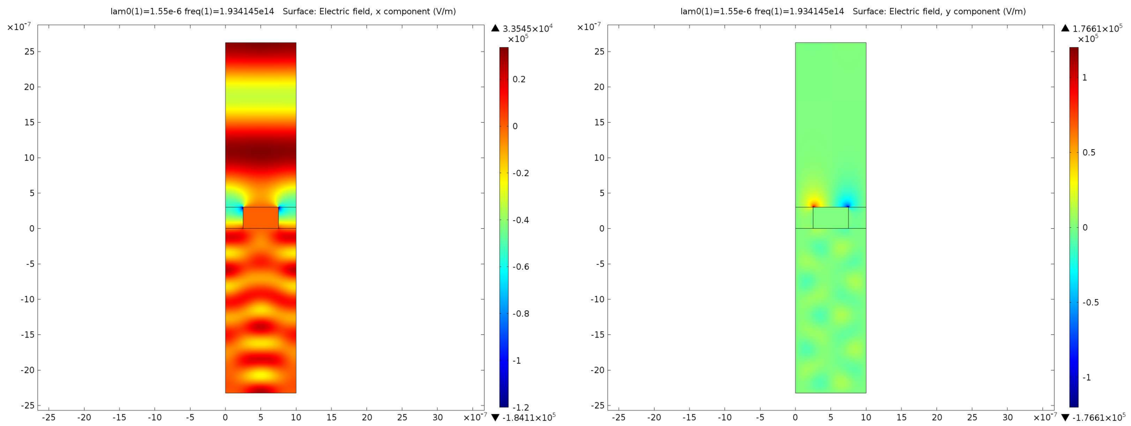

Fig. 2.21: Electric field x-component (left) and y-component (right) at 1.55 $\mu$m for a fixed phase.

where $\omega$ is the angular frequency, $\omega_p$ is the plasma angular frequency and $\omega_\tau$ is the scattering angular frequency. In order to have a good approximation for the optical properties of Au around 1.55 $\mu$m, a solution consists to invert Eq. 2.18 and to find the parameters $\omega_p$ and $\omega_\tau$ by requiring that the complex refractive index at 1.55 $\mu$m corresponds to that one given in Tab. 2.1. This requirement gives $\omega_p = 1.3737 \cdot 10^{16}$ rad/s and $\omega_\tau = 1.2081 \cdot 10^{14}$ rad/s. The model is then modified to account for the penetration depth within the metal by using a boundary layers meshing technique which consists in an automatic creation of a finer mesh around the selected boundaries. In this case a gradual meshing can be used to model better the rapid change of the electric field. Fig. 2.22 shows the mesh of a metal strip with this technique starting with a 2-nm-thick layer at the boundary and then gradually increasing the width of consecutive layers. In Fig. 2.23(a) is reported the transmittance of the previous structure with a Drude model approximation for a 300-nm-thick Au array. The overall shape of the curve is well-maintained with respect to the case of the quasi-PEC approximation. A first difference is the diffraction at $\lambda = pn/2 = 1.775$ $\mu$m which is more evident due to the effective aperture's width ($a_{eff}$) which does not coincide anymore with the physical aperture but it is roughly 540 nm instead of 500 nm. Mathematically, the reason of the larger difference at the diffraction relates to the sinc function in the expression of the propagator (see Eq. 2.15) which becomes different from zero. Another difference is related to the value of the transmittance at 1.55 $\mu$m which achieves 83%. This decrease is due to



 

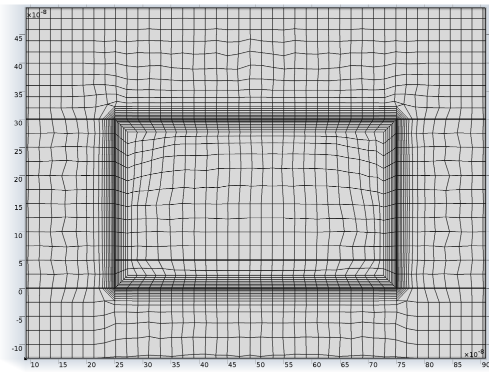

Fig. 2.22: Boundary layers meshing technique to account for the skin effect.

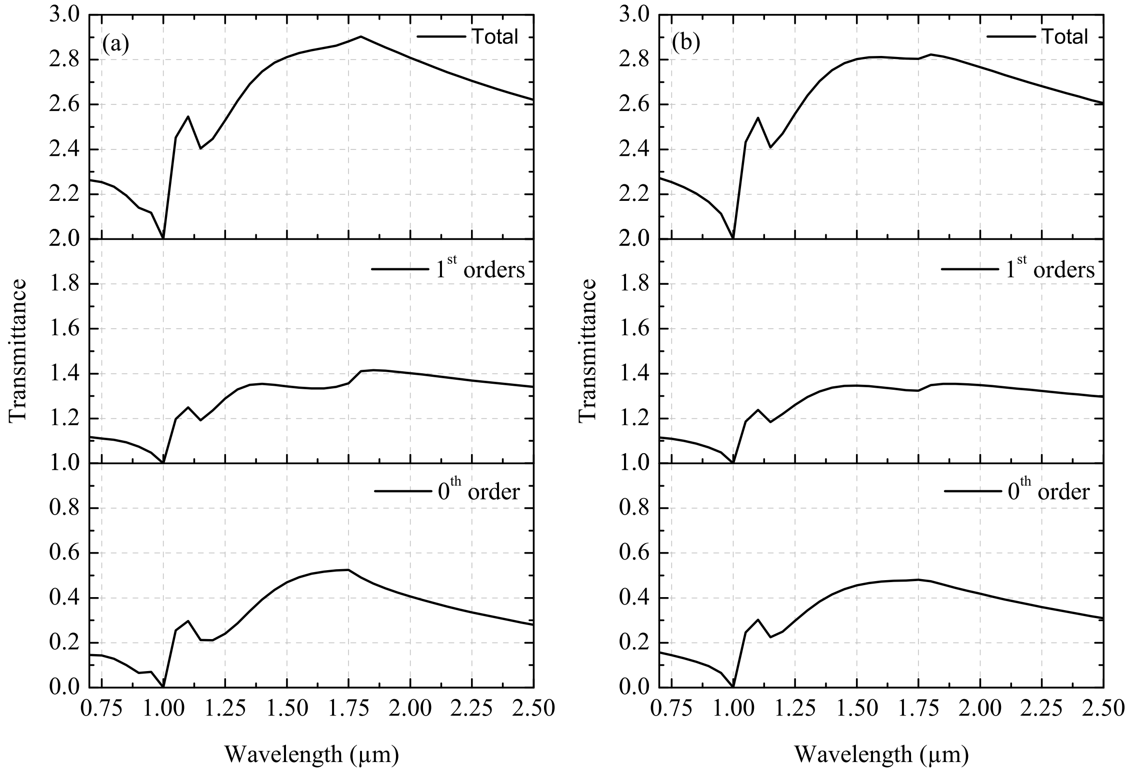


Fig. 2.23: Transmittance of the different orders as a function of the wavelength for the model of Fig. 2.19 with parameters $w = 0.5$ nm, $p = 1$ $\mu$m and $h = 300$ nm within the Drude model approximation for a 300-nm-thick Au array (a) and for a 50/250-nm-thick (Pt/Au) array (b). The curves for the sum of the $\pm 1^{st}$ diffraction orders and for the total transmittance are shifted by +1 for clarity.



 

a red-shift of the maximum of the transmission (90.2%) to a wavelength of 1.8 $\mu$m.

The following step consists in investigating the effect of a composite Pt/Au (50/250 nm) metal sequence on the transmission properties of the grid. Again Pt is modeled with a Drude model in the same manner as before with parameters $\omega_p = 2.01 \cdot 10^{16}$ rad/s and $\omega_\tau = 4.07 \cdot 10^{15}$ rad/s. In Fig. 2.23(b) it can be noticed that the transmittance is still high at 1.55 $\mu$m (81%), while at longer wavelengths it reduces for the $\pm$ 1 diffraction orders compared to the solely Au contact (Fig. 2.23(a)) achieving a maximum at 1.8 $\mu$m of 82.2%. An intuitive explanation of the reduction is related to the different penetration depth of the Pt compared to Au which reduces further the transmission due to absorption and which leads to a larger difference in the sinc function compared to Au justifing why the difference at 1.775 $\mu$m is more pronounced. Moreover, at longer wavelengths the difference between the two penetration depths for Au and Pt is more important than at lower ones ($\delta = 1/(k \cdot k_0)$), particularly in absolute terms once compared to a fixed aperture's width (smaller effective aperture).

The model is then modified to consider the case of a finite array by removing the periodic boundary conditions. Periodic ports have been replaced with standard ports (perfectly absorbing) always with plane-wave excitation and an input power of 1 W. At each side of the structure, two type of regions are placed to avoid that the scattered field is reflected back onto the device. The first type (dashed regions) consists only of air (upper part) and LM-InGaAs with zero absorption (lower part), while the second one are perfect matched layer (PML) regions which absorb within few tens of nm the impinging field with theoretically no reflection (see Fig. 2.24). Firstly, it has been studied the transmission as a function of the number of strips in a quasi-PEC approximation. The electric field wavefront evolution can be seen in Fig. 2.25 which shows $E_x$ for 9 strips. In Fig. 2.26 it can be observed that with 5 strips the transmittance reaches already high values (70%) and then it increases further reaching the value of 87%, close to the previous value of 91.3% in a periodic structure. This result is not really surprising as a similar behavior as been observed before in literature like in the case of thin slits on glass to study ET phenomenon [34]. However, in Ref. [34] the authors have found that 10 slits where sufficient to consider the structure as infinite. Here the value found is closer to 8-9 and a possible explanation can be the fact of having a substrate with a much higher permittivity than the glass one on which the slits were fabricated. Secondly, the wavelength range,



 

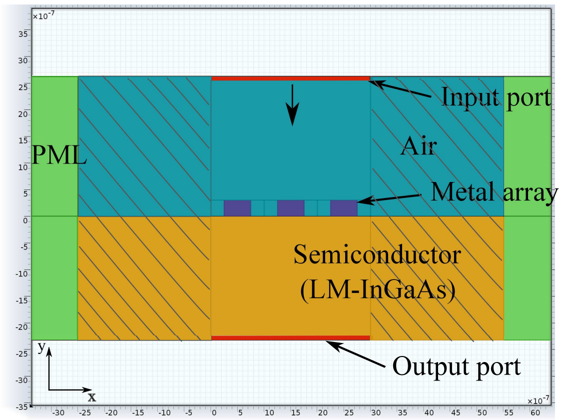


Fig. 2.24: Employed model to study the finite size effect within the previous geometry.

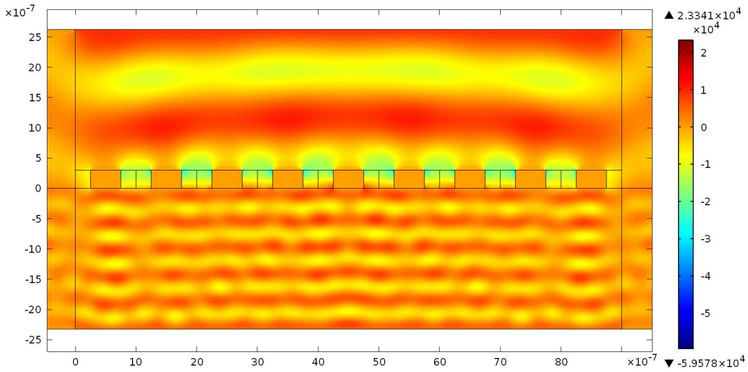

Fig. 2.25: Electric field x-component at 1.55 $\mu$m for 9 strips within the quasi-PEC approximation for the model of Fig. 2.24.

the different properties of the Au strips and the different geometric dimensions could influence also the dependence of the transmittance (see Fig. 2.27).

### 2.2.3 Inclusion of the epitaxial structure

The model is modified from the one of Fig. 2.24 to consider the epitaxial structure of the UTC-PD, in particular the one processed in this thesis. This structure, that will be presented in the next chapter, can be optically modeled with an equivalent one reported in Tab. 2.3. Layer 1 represents the diffusion barrier and the anode contact, layer 2 the active region, layer 3 the so-called spacer whose function will be introduced in the next chapter and layer 4 the collector and substrate. Layers



 

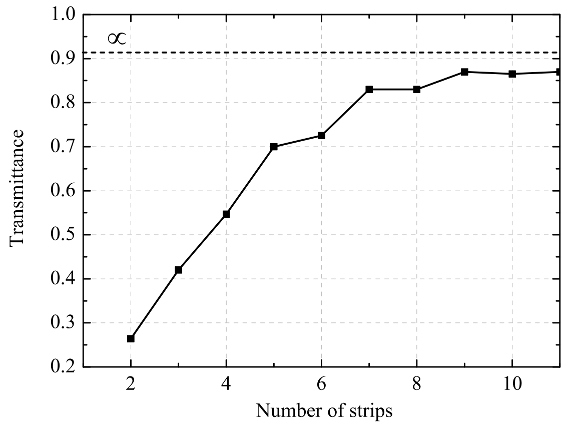


Fig. 2.26: Transmittance as a function of the number of strips within the PEC approximation at 1.55 $\mu$m. The dashed line indicates the value previously found in the case of an infinite number.

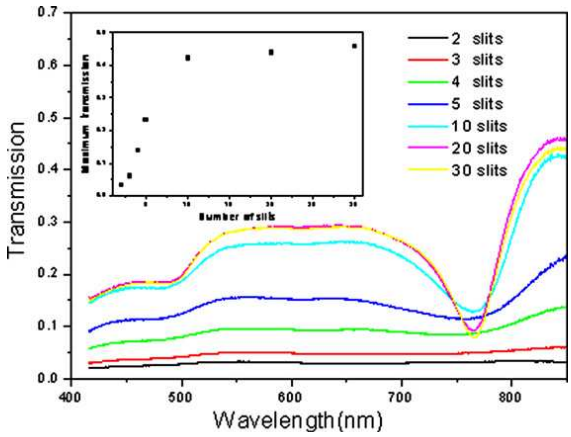


Fig. 2.27: Transmittance as a function of the number of slits for p-polarized light at normal incidence ($h$ = 300 nm, $w$ = 250 nm, $p$ = 500 nm), from Ref. [34].

1-2-3 are present only underneath the grid contact to account for the fabrication process (mesa structure). The thickness of the InP substrate plus collector has been chosen to 2.11 $\mu$m for having the same overall thickness as previously ($1.5\lambda = 2.32$ $\mu$m). Metals (Pt and Au) are modeled with their complex refractive indices at 1.55 $\mu$m reported in Tab. 2.1. The most important quantities to compute are the relative power absorbed in the active region and the one in the grid contact which are directly correlated with the efficiency and the heating of the device.



 

Table 2.3: Structure used to model optically the epitaxial layers of the UTC-PD considered in this thesis.

| No. layer | Material | Thickness (nm) | Complex refractive index |
|---|---|---|---|
| 1 | InGaAs (transp.) | 30 | 3.55 |
| 2 | InGaAs (active) | 150 | 3.55 + i0.12 |
| 3 | InGaAs (transp.) | 30 | 3.55 |
| 4 | InP | 2110 | 3.15 |

Regarding this electromagnetic model for the epitaxial layers the main approximation is to have associated a fixed refractive index to the different layers. Such approximation is pretty valid due to the very small relative change in refractive index given for example by a gradual composition in the active region (a difference in the real part of the refractive index of 0.1-0.2 can be found for the range of composition from In = 0.46 to In = 0.60) [2, 5].

#### 2.2.3.1 Absorption enhancement for higher efficiencies

The final objective is to evaluate the total EM power absorbed in the active region, obtained by computing the integral of the EM power loss density $P_{diss}^{EM}$ (W/m$^3$) in the active region. This quantity (correlated to the transmission) will give an approximated value of the responsivity for the final device. Moreover, the calculation of the dissipated power (in the same manner as before) in the contact will provide a useful information regarding the heating of the device. The power loss density averaged on a time period can be obtained by the conservation of the electromagnetic energy and, in the case of a dielectric where the Joule effect can be neglected compared to the absorption, no imaginary permeability and with an electric field at constant amplitude or slowly varying compared to the time period of oscillation and angular frequency $\omega_0$, its expression is given by [35]

$$\left\langle P_{diss}^{EM} \right\rangle = \omega_0 \mathrm{Im}\epsilon(\omega_0) \left\langle \boldsymbol{E} \cdot \boldsymbol{E} \right\rangle \tag{2.19}$$

where $\langle\rangle$ means the time average over a period equal to $2\pi/\omega_0$.

Firstly, the back-side illumination (with AR coating) for the model previously introduced will be considered to evaluate exactly the advantage of using a nanostructured contact. In particular, the Ti/Pt/Au (20/40/600 nm) contact employed in the previous thesis is considered for comparison. The complex refractive index for the Ti at 1.55 $\mu$m is reported in Tab. 2.1. The distribution of the power loss

Table 2.4: Integrated power loss density normalized to the impinging power over the contact surface and the active region (back-side configuration).

| Metal sequence | Abs. layer thickness (nm) | Metal contact abs. (%) | Active region abs. (%) |
|---|---|---|---|
| Ti/Pt/Au | 150 | 52.1 | 19.5 |
| Pt/Au | 150 | 46.0 | 20.6 |
| Ti/Pt/Au | 100 | 53.8 | 17.1 |

density is presented in Fig. 2.28. In this case, due to the simmetry of the structure, PEC boundaries have been used instead of periodic boundary conditions, while the output port of before as been used as input port (see Fig. 2.24). The previous boundary layer meshing technique has been applied to all the interfaces to take into account the penetration depth of the field. As it can be seen, a large part of the optical power is lost within the Ti and Pt layers. The reason for this non-monotonic distribution of $P_{diss}^{EM}$ in some layers (differently from the straightforward application of the Lambert-Beer law) is due to the multiple reflections at each interface. In

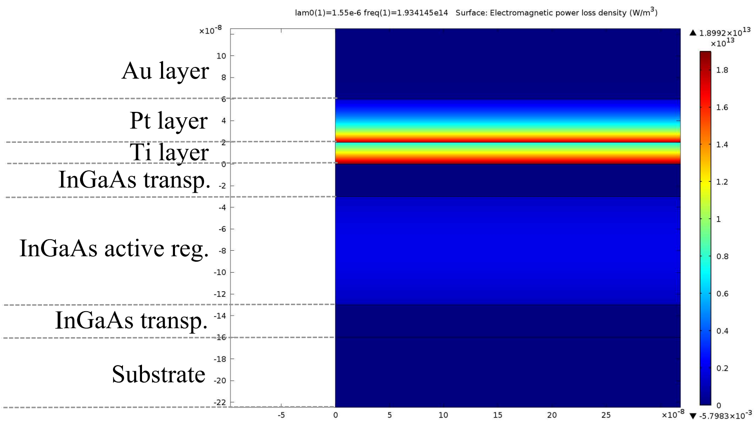


Fig. 2.28: Absorbed power density for a back-side configuration with the metal sequence of the previous thesis. The Au and the substrate layers are only partially reported.

Tab. 2.4 are reported the relative powers absorbed by the metal contact and by the active region for two different metal sequences: Ti/Pt/Au (20/40/600 nm) and Pt/Au (50/250 nm) and for an absorption region of 100 nm (previous thesis) and 150 nm (this work). It should be stressed that the power absorbed by the contact is roughly half of the total impinging power, while in the best case (for Pt/Au) the absorption in the active region is 20.6%.

In Tab. 2.5 is reported the power loss relatively to the initial impinging power as a function of the different number of strips for the contact. Even though the absorption in the active region is slightly lower for 5, 6 and 7 strips compared to a back-side illumination (150 nm), the power absorbed by the contact is definitely lower, less than half even in the worst case. Particularly, an absorption for the contact of 17.8% is similar to the values that can be achieved in a back-side configuration by the best metal choices like Ag or Au. Moreover, if the metal strips are completely removed, then the power absorbed in the active region is only 9.3% and, by using an antireflection (AR) coating at the interface, 12.9% due to the avoided Fresnel reflection. This value is slightly different from the value calculated with the Lambert-Beer relation $1 - e^{-\alpha d} = 13.6\%$. The reason is related to the InP layer underneath the InGaAs one, in fact by substituting it with a transparent InGaAs layer the value obtained for the absorbed power is 13.7%.

The use of such a contact can actually boost the absorption efficiency of UTC-PDs thanks to the high transmittance, leaky surface modes absorption and diffraction due to an increased optical path. However, in this particular case the diffraction intended in the far field region cannot fully explain the difference between the absorbed power with an AR coating (12.9%) and that one with 7 strips (17.0%). In fact, considering the first diffraction orders with $k = 2\pi/p$ then, the angle of diffraction with respect to the normal at the surface by simple trigonometry is only 26° which brings to an optical path of 168 nm instead of 150 nm and a consequent increase to 15.1%. Even though, this calculation is simplified as it does not take into account the epitaxial layers, the actual geometry of the structure (i.e. the finite size) and the fact that not all the power is distributed in higher diffraction orders, it gives an upper limit which tells that another mechanism, i.e. near-field effects due to leaky modes have to contribute [31, 36, 37]. Finally, a 10-nm-thick Ti-layer has been considered in the structure, underneath the grid contact. The reason is that this structure offers an interesting comparison from multiple aspects (optical, electrical and thermal) with respect to the previous structure. In Fig. 2.29(a) and (b) can be observed how the distribution of the power loss density changes with the introduction of a Ti layer. Such a layer is strongly detrimental from an optical point of view (roughly a factor 2). In particular, Tab. 2.6 reports the same quantities of Tab. 2.5, but considering the Ti layer (which contributes to the absorption of the metal contact).



 

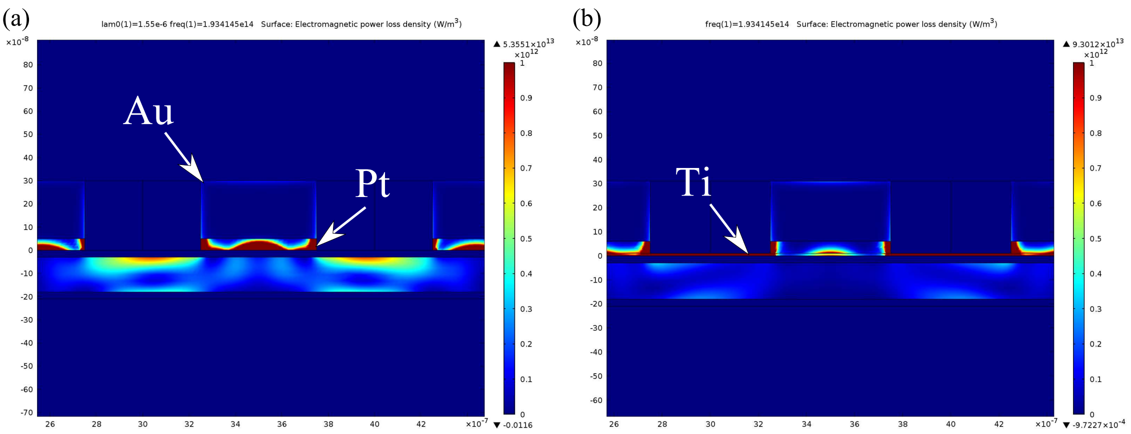


Fig. 2.29: Absorbed power density for the central strips of a Pt/Au (50/250 nm) contact with 7 strips without (a) and with (b) a 10-nm-thick Ti layer.

Table 2.5: Integrated power loss density normalized to the impinging power over the contact surface and the active region without Ti layer (front-side configuration).

| No. strips | Metal contact absorption (%) | Active region absorption (%) |
|---|---|---|
| 3 | 12.4 | 10.6 |
| 4 | 15.2 | 13.2 |
| 5 | 18.2 | 16.6 |
| 6 | 17.5 | 16.8 |
| 7 | 17.8 | 17.0 |

Table 2.6: Integrated power loss density normalized to the impinging power over the contact surface and the active region in the case of a 10-nm-thick Ti layer underneath the grid contact (front-side configuration).

| No. strips | Metal contact absorption (%) | Active region absorption (%) |
|---|---|---|
| 3 | 30.3 | 6.1 |
| 4 | 34.6 | 7.1 |
| 5 | 42.0 | 8.7 |
| 6 | 41.6 | 8.7 |
| 7 | 42.3 | 8.7 |

## 2.3 Conclusion

In this chapter it has been shown that a solution for back-side illuminated devices is difficult to achieve if high optical powers and high-frequency operation are sought due to the high specific contact resistance of the most reflecting metal choices over InGaAs. This problem can be solved by exploiting a front-side configuration and a sub-wavelength-based contact. A theoretical study shows that such a contact has several interesting features for high-power and high-frequency operation UTC-PDs like low absorption, low resistance (series and contact ones) and high transmission. Moreover, this contact presents a diffusion barrier in Pt and no back-side postprocessing, better heat dissipation due to the absence of optical window and to the strongly reduced absorption by the contact and an easier packaging. Furthermore, such a contact has other advantages which will be discussed in the next chapter regarding the ease of fabrication, especially for antenna integration. Finally, as already said, the technique to characterize on-wafer devices employing this type of contact is much easier than for back-side or edge-side configurations.

# Bibliography

[1] J. M. Vandenberg and H. Temkin, *An in-situ x-ray study of gold/barrier-metal interactions with InGaAsP/InP layers*, J. Appl. Phys. **55**, 3676 (1984)

[2] A. Beck, *Réalisation et charactérisation de photodiodes á transport unipolaire pour la génération d'ondes terahertz*, Ph.D Dissertation - University of Lille I (2008)

[3] H. Angus MacLeod, *Thin-film optical filters* (CRC Press, 2010)

[4] Eugene Hecht, *Optics (4th edition)* (Addison-Wesley, 2002)

[5] Sadao Adachi, *Physical properties of III-V semiconductor compounds: InP, InAs, GaAs, GaP, InGaAs and InGaAsP* (John Wiley & Sons, 1992)

[6] Sadao Adachi, *Properties of semiconductor alloys: group -IV, III-V and II-VI semiconductors* (John Wiley & Sons, 2009)

[7] John H. Weaver and Hans P. R. Frederikse, *CRC Handbook of chemistry and physics (Optical properties of metals and semiconductors)* (CRC Press, 1993)

[8] J. H. Weaver, D. W. Lynch, and C. G. Olson, *Optical properties of V, Ta, and Mo from 0.1 to 35 eV*, Phys. Rev. B **10**, 501 (1974)

[9] P. B. Johnson and R. W. Christy, *Optical constants of the noble metals*, Phys. Rev. B **6**, 4370 (1972)

[10] S. N. G. Chu, A. Katz, T. Boone, P. M. Thomas, V. G. Riggs, W. C. Dautremont-Smith, and Jr. W. D. Johnson, *Interfacial microstructure and electrical properties of the Pt/Ti ohmic contact in p-$In_{0.53}Ga_{0.47}As$ formed by rapid thermal processing*, J. Appl. Phys. **67**, 3754 (1990)

[11] J. S. Yu, S. H. Kim and, T. I. Kim, *PtTiPtAu and PdTiPtAu ohmic contacts to p-InGaAs*, in *Proceeding of IEEE ISCS Conference* (1997)

[12] V. L. Rideout, *A review of the theory and technology for ohmic contacts to group III-V compound semiconductors*, Solid State Electron. **18**, 541 (1975)

[13] Simon S. Sze, *Semiconductor devices - Physics and technology 2nd edition* (John Wiley & Sons and Inc, 2001)

[14] Jun J. Sakurai, *Modern quantum mechanics* (Revised edition - Addison-Wesley, 1994)

[15] A. Katz, W. C. Dautremont-Smith, S. N. Chu, P. M. Thomas, L. A. Koszi, J. W. Lee, V. G. Riggs, R. I. Brown, S. G. Napholtz, and J. L. Zilko, *Pt/Ti/p-*$In_{0.53}Ga_{0.47}As$ *low-resistance nonalloyed ohmic contact formed by rapid thermal processing*, Appl. Phys. Lett. **54**, 2306 (1989)

[16] P. W. Leech, G. K. Reeves, M. H. Kibel, *Pd/Zn/Pd/Au ohmic contacts to p-type* $In_{0.53}Ga_{0.47}As/InP$, J. Appl. Phys. **76**, 4713 (1994)

[17] G. Stareev, H. Kunzel, and G. Dortmann, *A controllable mechanism of forming extremely low resistance nonalloyed ohmic contacts to group IIIV compound semiconductors*, J. Appl. Phys. **74**, 7344 (1993)

[18] P. Ressel, K. Vogel, D. Fritzsche, and K. Mause, *Nonalloyed ohmic contacts for p+-type InGaAs base layer in HBTs*, Electr. Lett. **28**, 2237 (1992)

[19] G. Stareev, A. Umbach, F. Fidorra, and H. Roehle, *A reliable fabrication technique for very low resistance ohmic contacts to p-InGaAs using low energy Ar+ ion beam sputtering*, in *Third Conf. Indium Phosphide and Related Materials* (1991)

[20] A. Stano, *Chemical etching characteristics of InGaAs/InP and InAlAs/InP heterostructures*, J. Electrochem. Soc.:SOLID-STATE SCIENCE AND TECHNOLOGY **134**, 448 (1987)

[21] H.H. Berger, *Models for contacts to planar devices*, Solid-State Electronics **15**, 145 (1972)

[22] G. K. Reeves and H. B. Harrison, *Obtaining the specific contact resistance from transmission line model measurements*, IEEE Electron Device Letters **3**, 111 (1982)

[23] T. W. Ebbesen, H. F. Ghaemi, T. Thio, D. E. Grupp, and H. J. Lezec, *Extraordinary optical transmission through sub-wavelength hole arrays*, Nature **391**, 667 (1998)

[24] H. Bethe, *Theory of diffraction by small holes*, Phys. Rev. **66**, 163 (1944)

[25] E. Popov, M. Neviere, S. Enoch, and R. Reinisch, *Theory of light transmission through subwavelength periodic hole arrays*, Phys. Rev. B **62**, 16100 (2000)

[26] L. Salomon, F. Grillot, A. V. Zayats, and F. de Fornel, *Near-field distribution of optical transmission of periodic subwavelength holes in a metal film*, Phys. Rev. Lett. **86**, 1110 (2001)

[27] F. J. Garcia-Vidal and M. Moreno, *Transmission and focusing of light in one-dimensional periodically nanostructured metals*, Phys. Rev. B **66**, 155412 (2002)

[28] F. I. Baida and D. Van Labeke, *Three-dimensional structures for enhanced transmission through a metallic film: annular aperture arrays*, Phys. Rev. B **67**, 155314 (2003)

[29] W. L. Barnes, A. Dereux, and T. W. Ebbesen, *Surface plasmon subwavelength optics*, Nature **424**, 824 (2003)

[30] M. E. Stewart, C. R. Anderton, L. B. Thompson, J. Maria, S. K. Gray, J. A. Rogers, and R. G. Nuzzo, *Nanostructured plasmonic sensors*, Chem. Rev. **108**, 494 (2008)

[31] H. A. Atwater and A. Polman, *Plasmonics for improved photovoltaic devices*, Nature materials **9**, 205 (2010)

[32] F. J. Garcia-Vidal, M. Moreno, T. W. Ebbesen, and L. Kuipers, *Light passing through sub-wavelength apertures*, Rev. Mod. Phys. **82**, 729 (2010)

[33] Olek C. Zienkiewicz et al., *The finite element method: Its basis and fundamentals* (Elsevier Butterworth-Heinemann, 2005)

[34] Y. Pang, C. Genet, and T. W. Ebbesen, *Optical transmission through subwavelength slit apertures in metallic films*, Opt. Commun. **280**, 10 (2007)

[35] John D. Jackson, *Classical electrodynamics* (Third Edition - Wiley, New Jersey, 1998)

[36] J. He, C. Fan, J. Wang, Y. Cheng, P. Ding, and E. Liang, *Plasmonic nanostructure for enhanced light absorption in ultrathin silicon solar cells*, Adv. OptoElectron. **2012**, 1 (2012)

[37] Ed. Sarhan M. Musa, *Computational nanophotonics: modeling and applications* (CRC Press, 2013)

# Chapter 3

# On-wafer characterization of photodiodes at THz frequencies

In this chapter the epitaxial design, the fabrication and the characterization of UTC-PDs employing the nanostructured contact introduced earlier will be presented. Different designs will be considered to confirm the computational results and to understand better their main limitations. A comparison with the previous structure in terms of epitaxial design, fabrication process, experimental setup and performances will be given throughout the chapter.

## 3.1 Design of the epitaxial structure

The epitaxial structure has been inspired by the previous one already realized by a technique called molecular beam epitaxy (MBE) within the EPIPHY group at IEMN [1]. The design has been validated through the software Nextnano++, already introduced in the first chapter. In what follows the key features of MBE will be reported for the growth of III-V semiconductors. The main characteristics and changes of the UTC-PD structure will be underlined through a comparison in terms of band diagram with the previous structure.



 

### 3.1.1 Growth by molecular beam epitaxy

MBE is one of the main techniques to grow high-quality mono-crystalline compound semiconductor layers at the atomic scale level (order of Å). It is based on the condensation of materials at the surface of an opportunely heated crystalline substrate. In solid-state MBE (SSMBE), source materials are high-purity solid elements contained in effusion cells oriented towards the substrate. The sources are heated up to a certain temperature necessary for their sublimation [2]. The key aspect of SSMBE with respect to the other techniques is that it operates in ultra-high-vacuum (order of $10^{-8}$ Pa). The reason is that the mean free path (typical few meters) of the atoms or molecules once evaporated is large enough to avoid any collision before arriving on the substrate where, for suitable conditions, the atoms or molecules are adsorbed. This process brings to an extremely low concentration of thermodynamical defects and impurities, while monitoring in-situ and in real-time the quality of the growing structure through techniques exploiting for example the diffraction of high energy electrons [3]. These high-quality properties are achievable thanks to the possibility of having deposition rates as low as 1 atomic layer/s [2]. Another technique widely used is the gas source MBE (GSMBE) where the sources are in a gas phase (phosphine $PH_3$, arsine $AsH_3$ etc.) for V-elements like P, As and solid phase for III-elements like Ga, In or Al. The gas molecules are then thermally cracked in a specific section to obtain the V-elements which are made condensing on the sample's surface, while the $H_2$ molecules are removed from the system [4]. The main advantage of GSMBE over SSMBE is that the system for V-elements (generally consumed faster than III-elements) insertion in the UHV chamber is regulated by valves. In particular, there is no need of opening the UHV chamber if a V-element finishes, thus increasing the operation time of the overall system. Moreover, through mass flow controllers, it is possible to control precisely the deposition rate of a V-element without depending on the remaining quantity of that element in an effusion cell as may be the case of SSMBE. GSMBE has been used in this work for the epitaxial layers growth.

### 3.1.2 Principal characteristics of the structure

In the first chapter it has been shown that the UTC-PD structure presents multiple epitaxial layers addressed to solve different issues. General considerations regarding the substrate material or the working principles have been already discussed. Here the focus will be more on aspects related to the epitaxy and to the different constraints associated to the material properties. In Tab. 3.1 the structure of the previous thesis is presented with its band diagram reported in Fig. 3.1(a), while in Tab. 3.2 is presented the new structure with its band diagram reported in Fig. 3.1(b) [1]. Before analyzing the differences between the two structures, some considerations are needed to better understand the role of the different epitaxial layers.

The first thing to notice is that the electrons created in the absorption region (layer 3) find no barrier to diffuse/drift in the collector (layer 6). This is achieved by employing a spacer (layer 4) removing the jump in CB from layer 3 to layer 6 due to a different value of $E_g$. Such a spacer has a gradual composition to smooth the jump. Its influence can be seen in Fig. 3.2(a) presenting the structure of Fig. 3.1(b) without the spacer. A doping plane (layer 5) is used to lower the CB profile of the spacer as shown through the comparison with Fig. 3.2(b) by forcing the Fermi level to align. Furthermore, it can be observed that electrons are efficiently blocked by the diffusion barrier (layer 2) with a $\Delta E_c = 0.11$ eV. The structure is plotted up to the n-type InGaAs cathode contact (layer 8) because then the ohmic contact is deposited. The second sub-collector (layer 9) has the effect of decreasing further the resistance of the thin InGaAs cathode contact. The etching stop layer is placed underneath the sub-collector 2 in order to selectively stop the etching during the isolation process for technological reasons. The absorption region presents a gradual composition to establish a quasi-electric field as already explained in the first chapter. Due to strains in the structure, there is a practical limitation between the two extreme compositions at the borders of the absorption region. In particular, an energy difference of around 0.14 eV can be achieved in CB by changing the content of In from 0.46 to 0.6 and, consequently, the one of Ga.

First of all, the thickness of the absorption region has been changed from 100 nm to 150 nm to increase the efficiency due to the different illumination. This means that an equivalent electric field of roughly 14 kV/cm in the previous structure and 9.3 kV/cm in the new one accelerates the electrons during device operation in the low-injection regime. Another difference lies in the anode and cathode contacts (layer



 

1 and 8), which are 10-nm-thick instead of 50 nm and they present a composition of $In_{0.4}Ga_{0.6}As$ instead of $In_{0.53}Ga_{0.47}As$ to avoid absorption at 1.55 $\mu$m by having an $E_g = 0.84$ eV as reported in Tab. 3.1 and in the band diagram of Fig. 3.1(a). Regarding the choice of the doping elements, no change has been done with respect to the previous structure. For the p-type and n-type dopings, Be and Si have been used due to their well-known behavior for this kind of heteroepitaxial structures. For what concerns their concentrations, the p-type doping of the anode contact has been increased from $8 \cdot 10^{19}$ to $1 \cdot 10^{20}$ cm$^{-3}$ to decrease the specific contact resistance.

In terms of response speed, the only difference lies in the lower drift/diffusion time compared to the previous structure which is estimated as $\tau_a = W_a/v_d = 0.32$ ps instead of $\tau_a = 0.14$ ps (see subsection 1.2.2.1). In this case the approximation $v_d >> v_{th}$ can be used as $v_d = 4.7 \cdot 10^7$ cm/s (evaluated by calculating $\Delta E_c = 140$ meV from Fig. 3.2 and a mobility of 5000 cm$^2$V$^{-1}$s$^{-1}$) and $v_{th} = 1 \cdot 10^7$ cm/s [5].



 

Table 3.1: UTC-PD epitaxy used in the previous thesis (identification number: G060304) [1]

| No. | Layer | Material | Thickness (nm) | Doping ($cm^{-3}$) | Comments |
|---|---|---|---|---|---|
| 1 | Anode contact | $In_{0.53}Ga_{0.47}As$ | 50 | p = $8{\cdot}10^{19}$ (Be) | - |
| 2 | Diffusion barrier | $Al_{0.075}In_{0.53}Ga_{0.395}As$ | 20 | p = $5{\cdot}10^{19}$ (Be) | $E_g$ = 0.845 eV |
| 3 | Absorption region | $In_{0.47}Ga_{0.53}As$ | 100 | p = $1{\cdot}10^{18}$ (Be) | Gradual |
| | | $In_{0.60}Ga_{0.40}As$ | | | alloy |
| 4 | Spacer | $In_{0.60}Ga_{0.40}As$ | 10 | p = $1{\cdot}10^{18}$ (Be) | Gradual |
| | | $Al_{0.235}In_{0.53}Ga_{0.235}As$ | 20 | nid | alloy |
| 5 | Doping plane | InP | 7 | n = $1{\cdot}10^{18}$ (Si) | - |
| 6 | Collector | InP | 100 | nid | - |
| 7 | Sub-collector 1 | InP | 50 | n = $2{\cdot}10^{19}$ (Si) | - |
| 8 | Cathode contact | $In_{0.53}Ga_{0.47}As$ | 60 | n = $2{\cdot}10^{19}$ (Si) | - |
| 9 | Sub-collector 2 | InP | 300 | n = $3{\cdot}10^{19}$ (Si) | - |
| 10 | Etching stop | $In_{0.53}Ga_{0.47}As$ | 20 | n = $3{\cdot}10^{19}$ (Si) | - |
| 11 | Buffer | InP | 17.5 | nid | - |
| 12 | Substrate | InP | - | Semi-Insulating | - |

Table 3.2: UTC-PD epitaxy processed during this work (identification number: G120501).

| No. | Layer | Material | Thickness (nm) | Doping ($cm^{-3}$) | Comments |
|---|---|---|---|---|---|
| 1 | Anode contact | $In_{0.4}Ga_{0.6}As$ | 10 | p = $1{\cdot}10^{20}$ (Be) | $E_g$ = 0.84 eV |
| 2 | Diffusion barrier | $Al_{0.075}In_{0.53}Ga_{0.395}As$ | 20 | p = $5{\cdot}10^{19}$ (Be) | $E_g$ = 0.845 eV |
| 3 | Absorption region | $In_{0.47}Ga_{0.53}As$ | 150 | p = $1{\cdot}10^{18}$ (Be) | Gradual |
| | | $In_{0.60}Ga_{0.40}As$ | | | alloy |
| 4 | Spacer | $In_{0.60}Ga_{0.40}As$ | 10 | p = $1{\cdot}10^{18}$ (Be) | Gradual |
| | | $Al_{0.235}In_{0.53}Ga_{0.235}As$ | 20 | nid | alloy |
| 5 | Doping plane | InP | 7 | n = $1{\cdot}10^{18}$ (Si) | - |
| 6 | Collector | InP | 100 | nid | - |
| 7 | Sub-collector 1 | InP | 50 | n = $3{\cdot}10^{19}$ (Si) | - |
| 8 | Cathode contact | $In_{0.4}Ga_{0.6}As$ | 10 | n = $3{\cdot}10^{19}$ (Si) | - |
| 9 | Sub-collector 2 | InP | 300 | n = $3{\cdot}10^{19}$ (Si) | - |
| 10 | Etching stop | $In_{0.4}Ga_{0.6}As$ | 20 | n = $3{\cdot}10^{19}$ (Si) | - |
| 11 | Buffer | InP | 17.5 | nid | - |
| 12 | Substrate | InP | - | Semi-Insulating | Orientation (100) |



 

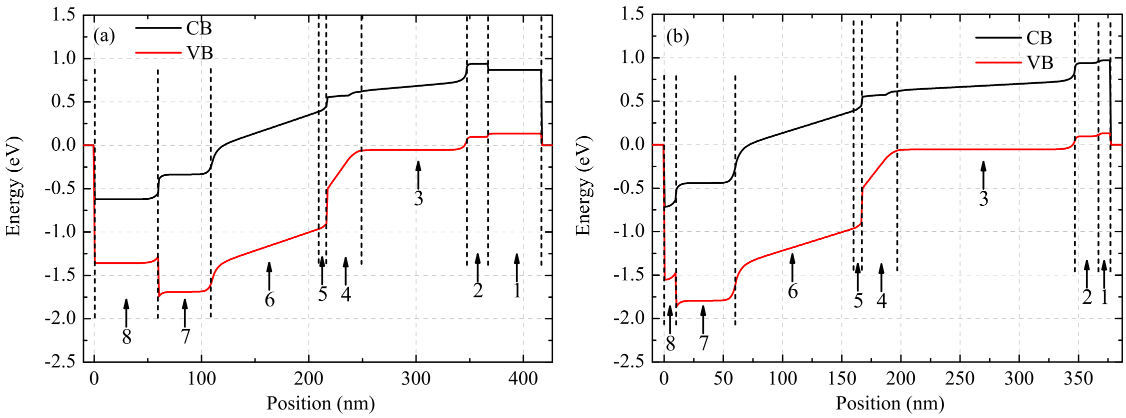


Fig. 3.1: Band diagram of the structures of Tab. 3.1 (a) and Tab. 3.2 (b). Ohmic contacts have been applied in the abscissa range: (-10,0);(417,427) nm (a) and (-10,0);(377,387) nm (b).

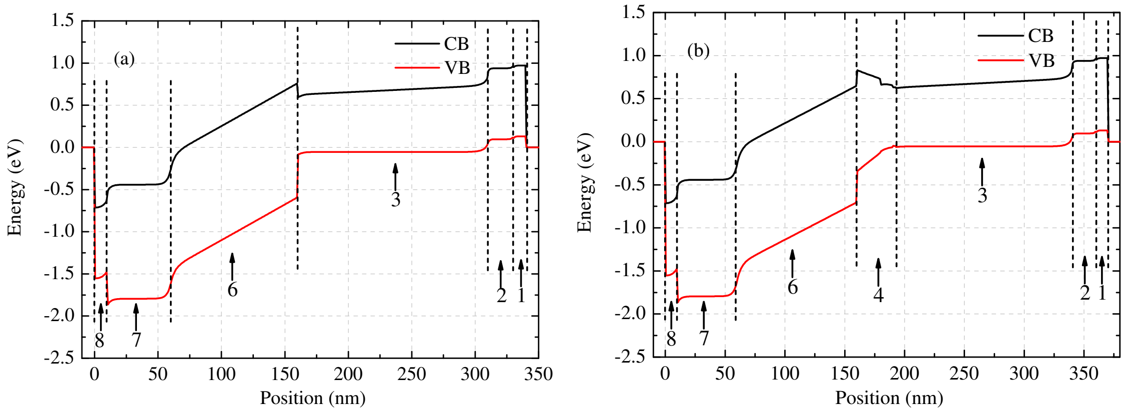


Fig. 3.2: Band diagram of the structure of Tab. 3.2 without spacer and doping plane (layer 4 and 5) (a) and without doping plane (layer 5) (b). Ohmic contacts have been applied in the abscissa ranges: (-10,0);(340,350) nm (a) and (-10,0);(370,380) nm (b).



 

# 3.2 Fabrication of uni-travelling carrier photodiodes

In this work, the fabrication of UTC-PDs has been based on the patterning of the sample's surface by e-beam lithography. In what follows the principal steps, reported schematically in Fig. 3.3, will be illustrated underlining the most crucial parts of the fabrication.

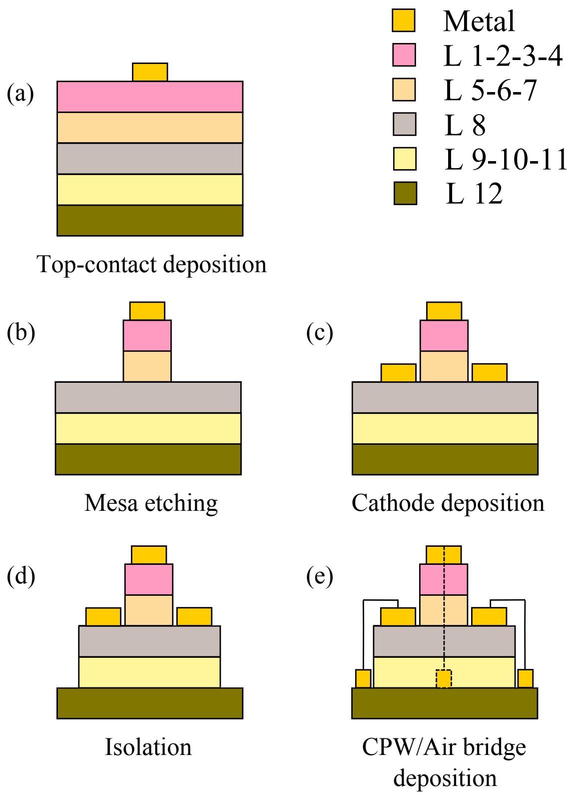


Fig. 3.3: Schematic diagram of the fabrication process. L refers to the layers reported in Tab. 3.2. The black lines at step (e) represent the air-bridge that electrically connects the anode and the cathode contact with the coplanar waveguide (CPW) transmission lines.

## 3.2.1 High-aspect ratio slits

One of the main ways to fabricate arrays of slits with $\mu$m and sub-$\mu$m dimensions is by a focused ion beam (FIB) technique. Such a technique relies on the physical etching of a material through an accelerated ion beam. The main advantage of this tool for this kind of structures is the possibility to achieve high aspect-ratio and to obtain highly precise and abrupt profiles. It has been already successfully used to fabricate samples for studying the ET phenomenon at sub-$\mu$m wavelengths in the case of arrays of slits [6]. However, the principal disadvantage comes from the high ion beam etching rate of III-V semiconductors, in particular higher than for Au. In fact, in order to study only the transmission properties of an array of slits, glass is not a major problem as substrate material (see Fig. 3.4). The etching rate by FIB technique of glass is much lower compared to III-V semiconductors permitting to have a higher tolerance in the effective etching time. Some tests have been carried on over an InP substrate with a 300-nm-thick Au layer deposited by e-beam evaporation to investigate the possibility of employing such a technique. From Fig. 3.5 it is clear that a problem of homogeneity appears at the sample metal surface. This problem can be solved by etching the sample for a longer time in order to completely remove the metal from the slits. However, due to the fact that some metal regions have been already etched completely, the added time spent on them will lead to an etching time for the semiconductor, in particular for the active region in the case of a UTC-PD structure. These considerations associated to the fact that the etching of each device has to be done separately due to the intrinsic operation of the FIB technique, are the reasons for which only e-beam lithography has been investigated for the design of the contact, in particular taking into account its limitations for high aspect-ratios slits.

The fabrication has been done under the supervision of Dr. Mohammed Zaknoune belonging to the group ANODE at IEMN. Different geometries of contacts have been considered to understand experimentally the influence of the various elements like the strip's width and the contact resistance. In Tab. 3.3 are reported the characteristics of the contacts with their associated reference. This reference, followed by the side width of the contact, will be used in the characterization section to distinguish each of them. The technological steps consist in the deposition of Ti/Au (20/100 nm) markers, of a 10-nm-thick Ti layer (only for some devices) and of the Pt/Au anode contact (50/250 nm) (see Fig. 3.3(a)). Markers are necessary for the alignment of the different layers during the fabrication process. The technique for depositing metal patterns has been already discussed in subsection 2.1.2.1 and described in Fig. 2.6. Due to the fact that the Ti layer (10 nm) is not thick enough

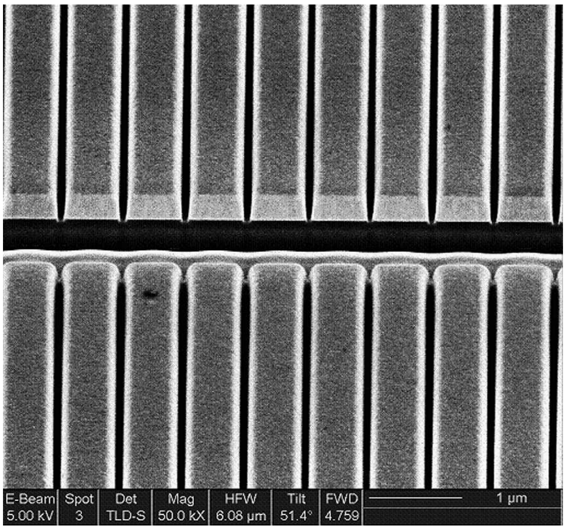


Fig. 3.4: Array of slits fabricated by a FIB technique starting from a 400-nm-thick Au layer thermally deposited over a 1-mm-thick glass substrate. Parameters are $p$ = 750 nm and $w$ = 250 nm, from Ref. [6].

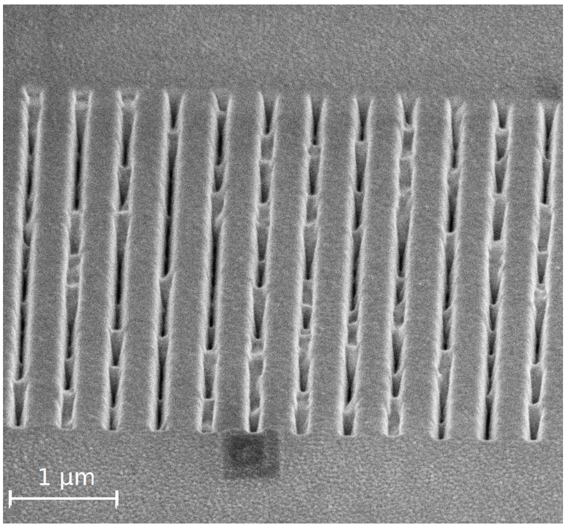


Fig. 3.5: Example of a test carried on at IEMN by Dr. David Troadec to investigate the FIB technique for the fabrication of arrays of slits.

Table 3.3: Different geometries of top-contacts studied.

| Ref. | Strip width/period ($\mu$m) | Covered Area | Ti layer |
|---|---|---|---|
| A | 0.5/1 | 50% | No |
| B | 0.5/1 | 50% | Yes |
| C | 0.3/1.45 | 21% | No |
| D | 0.3/1 | 30% | No |
| E | 0.3/1 | 30% | Yes |

to be used as a marker layer, the markers have been deposited alone as the first layer. The thin Ti layer is a square pattern (side length corresponding to the strip's length of the grid contact) which is present only for B and E type devices (see Fig. 3.3) underneath the Pt/Au grid contact. Some difficulties have been encountered during the fabrication due to the high-aspect ratio of the strips. Their widths are $w_1 = 300$ or $w_2 = 500$ nm with a thickness $h = 300$ nm for all the designs as already discussed for optical reasons in the previous chapter. The necessary high quality for the strips has obliged to some preliminary tests by changing parameters of the e-beam writing such as the dose, the current and/or the correction file to take into account the geometry, apart from having tried different resists combinations. The results of these tests are reported in Fig. 3.6 showing the bi-layered resist profile before (a) and after metallization and consequent lift-off process (b).

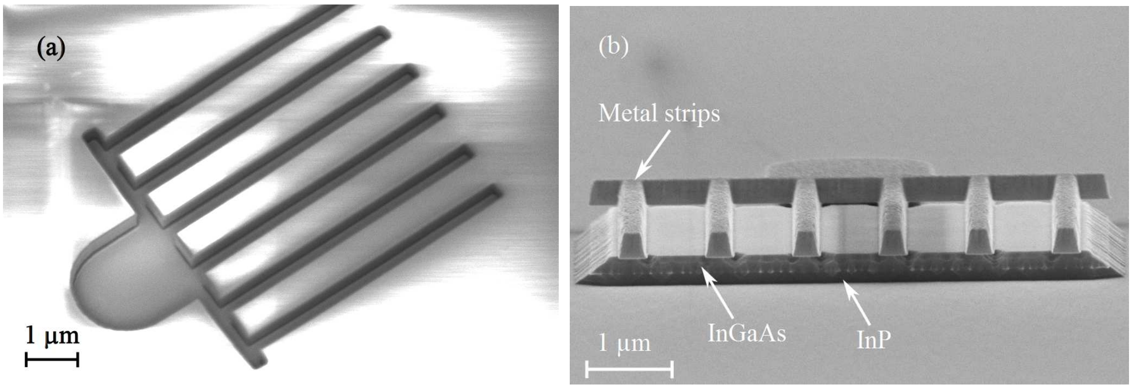


Fig. 3.6: SEM images of the process for strips fabrication with width $w_1$. In Fig. 3.6(a) is reported the resist pattern before metal deposition and in Fig. 3.6(b) the metal strips after lift-off. Moreover, Fig. 3.6(b) shows also the following step of mesa definition explained in the next subsection.



 

### 3.2.2 Definition of the mesa

The second major step consists in the so-called "mesa definition" which means, with reference to Tab. 3.2, the etching of the epitaxial structure (layers 1 to 7) up to the cathode contact (layer 8) (see Fig. 3.3(b)). The wet etching process for InGaAs ($H_20$:$H_2O_2$:$H_3PO_4$ with ratios 40:5:1) has been already explained in subsection 2.1.2.1 (see Fig. 2.6). For what concerns the selective etching of InP the solution used consists of $HCl/H_3PO_4$ in ratio 1:4. This solution is well-known and presents an etching rate varying with the percentage of HCl (here roughly 1 $\mu$m/min) [1]. In Fig. 3.6(b) the etching profile is clearly evident for the different materials (no distinction can be seen between the quaternaries and InGaAs). No etching stop layer is needed at this point due to the respective solution selectivities. The smallest etched feature is a mesa of 2 $\mu$m in diameter for contacting the device through an air-bridge. This contact region can be seen better in Fig. 3.7(a) where the etching reveals also the InP crystalline planes at 45° with respect to the contact side. In order to reduce the capacitance of the device due to this added circular region, the resist protected only the active region (where the grid is), while the remaining one was protected by the metal to benefit from the under-etching decreasing the added capacitance. However, it has been observed that the resist had a worst adherence to the metal compared to the semiconductor. This difference translated in an etching of the active region due to the penetrated solution with degradation of the device's characteristics, in particular of the responsivity. Fortunately, this problem was observed only on some devices and a mapping of the sample has been carried on to identify the damaged devices.

### 3.2.3 Cathode contact and isolation

After mesa definition, the fabrication proceeds with the deposition of a Ti/Pt/Au cathode ohmic contact (see Fig. 3.3(c)). This step (analogous to the markers deposition) does not present any difficulty due to the large size (tens of $\mu$m) of the patterns. After the contact deposition, the device is electrically isolated from the others by wet-etching (through the same solutions as before), with reference to Tab. 3.2, layers 8 to 11 (see Figs. 3.3(d) and 3.8(a)). The etching is stopped when the sample presents the semi-insulating (S.I.) substrate's surface (no more current is measured between test pads by I-V measurements). This means that transmission



 

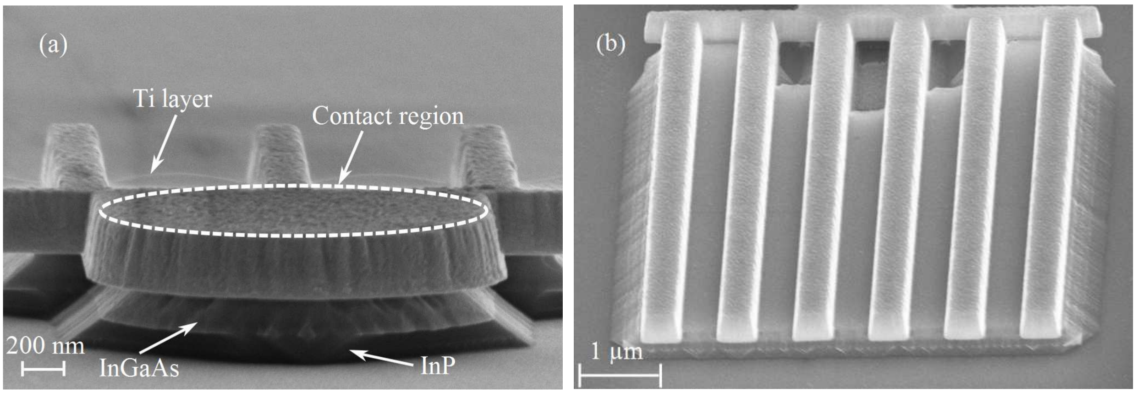


Fig. 3.7: SEM images of the etching process. (a) shows the contact region and the peculiar etching profile of InP. (b) shows the etching of the active region related to the penetration of the solution.

lines can be deposited without risking of short-circuits due to a non-negligible conductivity of the surface. Due to the considerable thickness of the InP subcollector 2 (300 nm) and to the fact that the buffer and the substrate are both in InP, an etching stop-layer is present to avoid that the etching process creates a step in height too large, relative to the anode contact (see the air-bridge contact region in Fig. 3.8(b)), for the air-bridge fabrication.

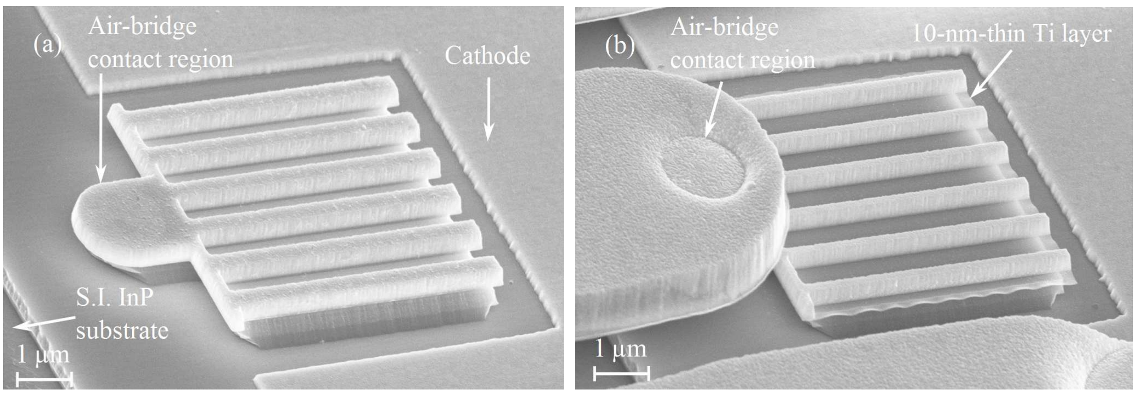


Fig. 3.8: SEM images of an A6 type device before air-bridge connection (a) and of an E6 type device after air-bridge connection (b).



 

### 3.2.4 Transmission lines and air-bridge interconnection

In order to perform on-wafer measurements, coplanar waveguides (CPW) transmission lines are used. They present an impedance of 50 $\Omega$ at the device point calculated through a 3D full-wave electromagnetic solver based on a finite integration technique, CST Microwave Studio [7]. The CPW is linearly tapered to keep the impedance almost constant, while having a geometry suitable for measurements with ground-signal-ground (GSG) probes with a pitch of 125 and 50 $\mu$m. Ti/Au (100/400 nm) CPWs are deposited with the standard process (like for the markers) without any difficulty due to their large dimensions (several $\mu$m). After that, the air-bridge process starts with the creation of a resist support for the air-bridge. This step is reported in Fig. 3.9(a) which shows the resist pattern (PMGI-SF11) with the openings on the cathode and anode ohmic contacts and on the CPW conductors as supports for the air-bridge.

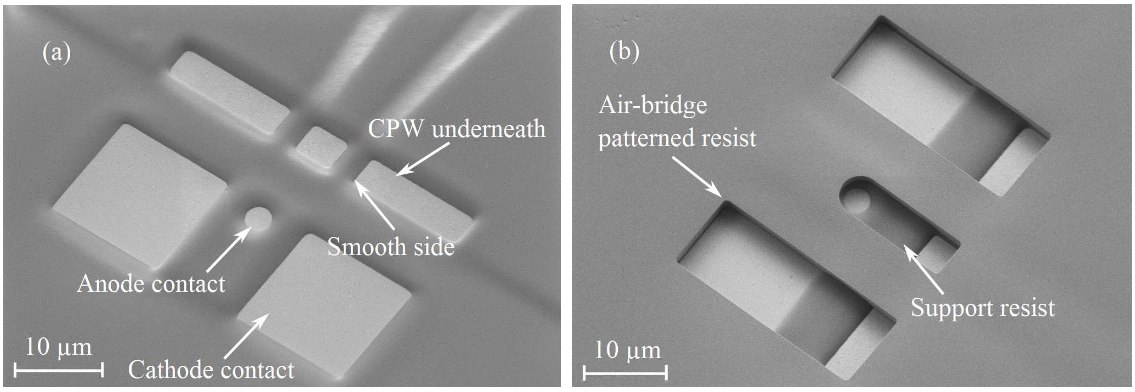


Fig. 3.9: SEM images of the air-bridge process. (a) shows the resist support (PMGI-SF11) after its re-flowing. (b) shows the resist profile (MMA/PMMA) and the resist support (mono-layer underneath) before the metallization of the air-bridge.

After definition of the support, the resist is made re-flowing on the walls of the apertures (by a short baking) to avoid sharp angles that could damage the bridge during the next steps. The resist used as support is chosen to be selective with the developper solution used for the above resist to pattern the bridge. In this way, the support is not damaged during the development of the above bi-layered resist (MMA/PMMA) as it can be observed in Fig. 3.9(b). At the end, a Ti/Au (200/600 nm) layer is deposited for the air-bridge fabrication (see Fig. 3.3(e)). An example of a completed device is reported in Fig. 3.10 with the dimensions of the CPW lines.



 

There are a few main differences in the fabrication with respect to the previous Ph.D thesis [1]. Firstly, the top-contact is semi-transparent instead of being a circularly thick Ti/Pt/Au (20/40/600 nm) metallization (see Fig. 3.11). The reason is related to the back-side illumination in the previous case as already explained before. Secondly, due to the on-wafer measurements, no antenna is required to test the devices. This aspect has two important consequences:

- The fabrication process is much easier as it does not require a 3D antenna like the TEM horn antenna developed in the previous work and reported in Fig. 3.11 (planar antennas are not practically useful for back-side configuration due to the illumination setup/optical path which would coincide with the RF radiating field path) [1]. However, with CPWs the measurements are possible only up to 325 GHz due to the availability of suitable probes.

- The number of devices on a wafer is extremely higher due to the absence of the antenna (the TEM horn antenna occupied around 6 $mm^2$, while the CPW lines here 0.06 $mm^2$).

The previous two points underline the possibility to test many more devices and to perform multiple changes on the geometries, structures, metallizations etc. obtaining useful information for the final device. Furthermore, the front-side configuration allows to integrate classical planar antennas like the log-periodic or the spiral one [8]. However, differently from a TEM horn antenna, an hyperhemispherical Si lens is needed to improve the directivity of planar antennas reducing also the Fresnel losses and avoiding substrate modes.

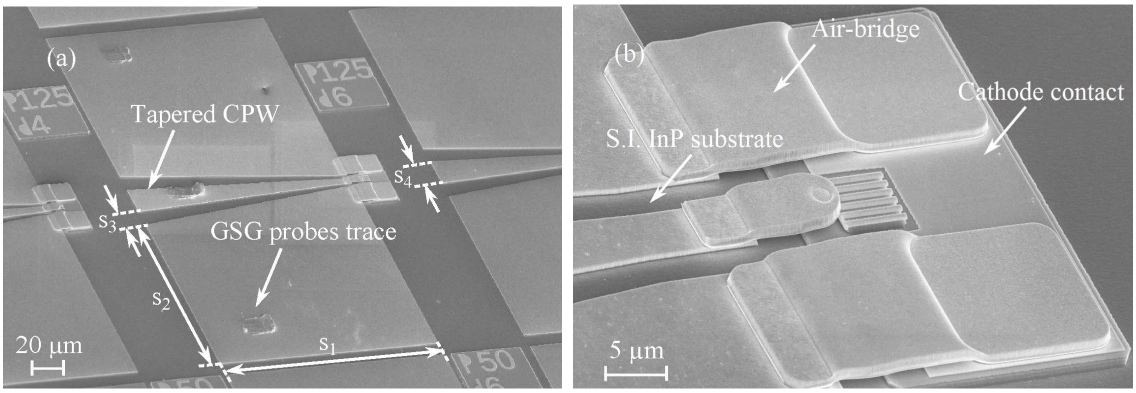


Fig. 3.10: SEM images of a completed device integrated with CPW lines. (a) shows the CPW geometry employed and the GSG probes trace after measurements. The CPW lines dimensions are $s_1 = 160$ $\mu$m, $s_2 = 128$ $\mu$m for the 125-$\mu$m-pitch (53 $\mu$m for the 50-$\mu$m-pitch), $s_3 = 12$ $\mu$m and $s_4 = 20$ $\mu$m. (b) shows a close-up of an A6 type device.

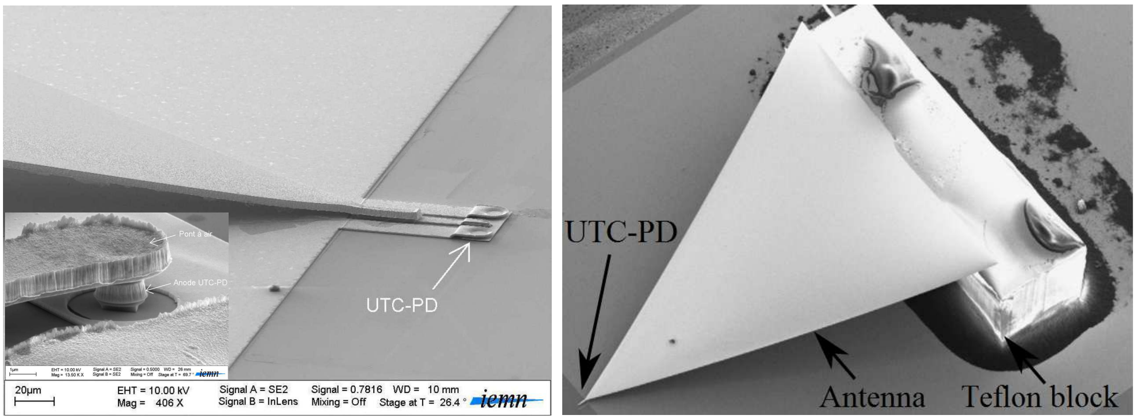


Fig. 3.11: SEM images of a UTC-PD fabricated in the previous thesis. The UTC-PD is connected with an air-bridge and monolithically integrated to a 3D TEM horn antenna. The inset shows a close-up of a 2-$\mu$m-diameter device, from Ref. [1].

## 3.3 On-wafer characterization

In this section the results of the devices in terms of efficiency, frequency response and total power generated are presented. The characterization has been done by on-wafer measurements thanks to a bench for optoelectronic experiments developed by Dr. G. Ducournau, Dr. E. Peytavit and Dr. J.-F. Lampin, all belonging to the THz photonics group at IEMN led by Dr. J.-F. Lampin. The measurements have been performed jointly with Dr. G. Ducournau.

### 3.3.1 Experimental setup

The experimental setup, reported in Fig. 3.12, consists of an optical part to generate the beatnote, an optoelectronic part which is the device under test (DUT) and an RF part where the generated RF power is detected. For what concerns the optical part, there are two distributed feedback lasers (DFBs: 81642A Agilent external cavity lasers) to generate the beatnote followed by polarizer controllers based on stress-induced birifrengence in order to have the same polarization for optimal photomixing, an erbium doped fiber amplifier (EDFA) to increase the initial power of DFBs (up to around 400-450 mW), another polarizer controller to adjust the polarization of the electric field perpendicularly with respect to the slits, a 99/1% coupler to monitor the laser frequencies with a wavemeter and to illuminate UTC-PDs thanks to a lensed fiber with a minimum waist of 1.5 $\mu$m. In order to align the fiber to the device, a camera with microscope objective was mounted at 45° (compared to the sample plane) to image the sample, the fiber and the GSG probes (Probes Cascade Microtech GSG) (see Fig. 3.13). The UTC-PD (DUT) receives the impinging optical beams at frequencies $\nu_1$ and $\nu_2$ and generates the beatnote at frequency $\nu_1 - \nu_2$ that propagates in the CPW. Finally, the RF part concerns the GSG probes (different probes have been used depending on the frequency band) with integrated bias-T to apply a bias to the UTC-PD (without leading the RF signal going in the bias circuit and the DC current going in the AC circuit) and to measure the DC photocurrent with an amperometer. GSG probes are integrated with coaxial or waveguide-type extenders depending on the frequency band in order to connect the detector for the RF measurements. Two types of detector have been used: a bolometer (438A + 8487A for 0.05-50 GHz or W8486A for 75 - 110 GHz Agilent) for the measurements up to 110 GHz and a calorimeter (Erickson PM4), illustrated in Fig. 3.15, for the measurements in WR 3.4 band (220-325 GHz). The protocol for the measurements consisted in the following steps:

1. Searching the mapped device according to its position on the sample.

2. Tracing an I-V characteristic of the device to verify its diode-like behavior.

3. Aligning the lensed fiber to the device by optimizing the DC photocurrent.



 

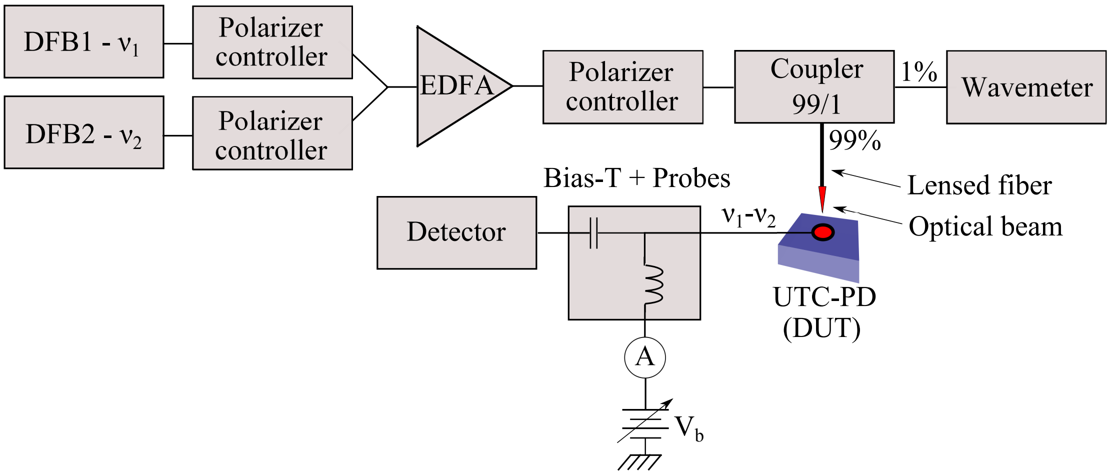


Fig. 3.12: Experimental setup employed for on-wafer characterization of UTC-PDs.

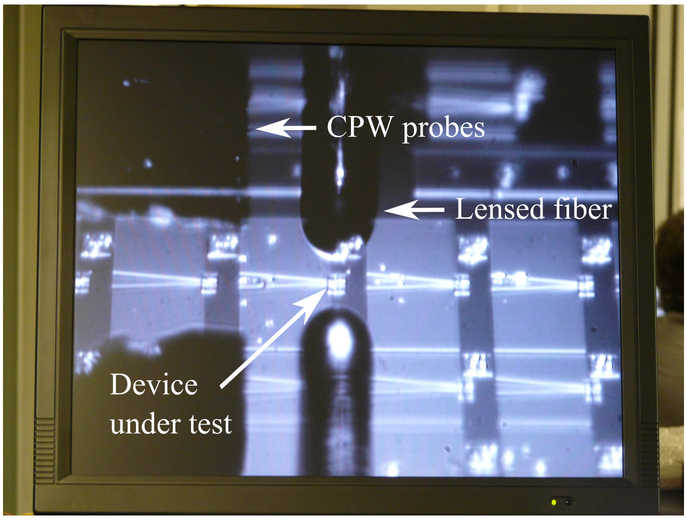


Fig. 3.13: Screen microscope view showing the lensed fiber illuminating the DUT.

4. Rotating the polarization of the optical beam to find the maximum photocurrent.

5. Tracing I-V characteristics at different optical powers to check the linearity.

6. Measuring the RF power at different optical powers.

Further steps not carried on over all the devices were:

- Measuring the RF power and DC photocurrent at different bias voltages (in some cases up to the device's destruction).



 

- Measuring the RF power at different optical powers (in some cases up to the devices destruction).

No specific cooling system has been used throughout the measurements. The sample was cooled thanks to the natural conduction of the metal chuck at RT (substrate thickness 350 $\mu$m). The losses due to the fiber coupling and path from the EDFA to the output of the fiber have been deduced equal to 4 dB from measurements with a power meter. The measurements have been corrected for the losses of the coaxial cable plus the probes and the bias-T (bolometer detection up to 50 GHz) and for the GSG probes and the bias-T (bolometer/calorimeter detection above 75 GHz). The measurements are not corrected for the coupling between the output of the fiber and the UTC-PD surface related to the Gaussian spot-size.

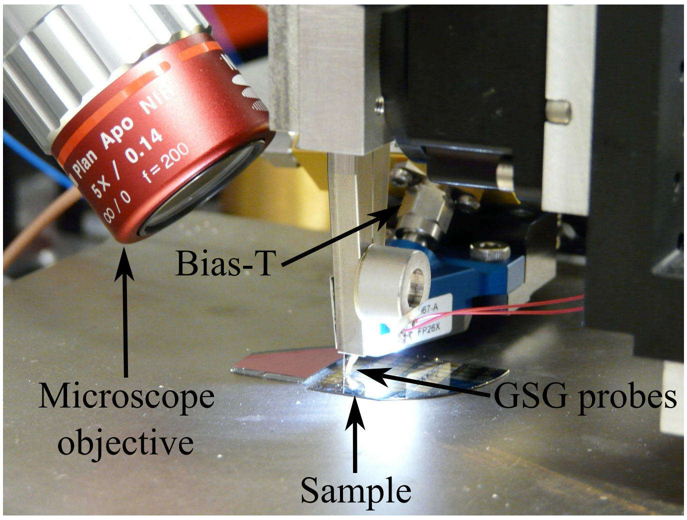


Fig. 3.14: Close-up of the GSG probes contacting the sample.

### 3.3.2 Results and analysis

In what follows the results for the fabricated UTC-PDs are reported. Due to the large number of measurements, only some representative curves are reported even though the extrapolated values for significant parameters are given in tables.



 

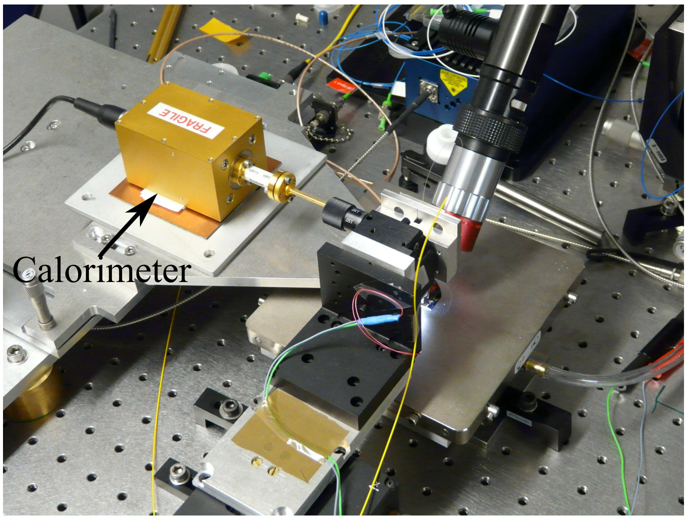


Fig. 3.15: Experimental setup employed for on-wafer characterization of UTC-PDs (220-325 GHz).

#### 3.3.2.1 I-V characteristics

A Keithley multimeter served as amperometer to measure the DC photocurrent and as generator to apply the bias voltage. In Figs. 3.16 and 3.17 are reported several I-V characteristics in a dark condition for different types of UTC-PDs (see Tab. 3.3 for the references). From these measurements two parameters can be extracted: the ideality factor $\eta$ and the dark current $I_s$ of the PD. These parameters are evaluated with no illumination for simplicity. Here, the theoretical I-V relation for a PD in the absence of photocurrent (Eq. 1.1 with $I_{ph} = 0$ see subsection 1.1.1.1) is modified to take into account the non-ideality of the junction (due to generation-recombination processes in the depleted region and at the contact surface) and is given by

$$I = I_S(e^{\frac{qV}{\eta k_B T}} - 1) \tag{3.1}$$

The values for $\eta$ are obtained by taking the natural logarithm of the current and then the derivative of the curve (by neglecting the factor -1 in Eq. 3.1) $dI/dV = q/(\eta k_B T)$. A strong difference can be observed among devices with and without Ti layer. In fact, for B type devices (with Ti layer) the values obtained for $\eta$ are similar to those in literature for PDs in InGaAs/InP and their characteristics are linear over all the considered range (see Figs. 3.16(b) and 3.17(b)) [9]. On the contrary, for devices without Ti layer the linearity at large bias voltages (above 0.3-0.4 V) is no more maintained and the values for $\eta$ are quite different (up to 2.7). It can be noticed also that for C type devices the values are the largest. This issue has been observed also on other devices with same topologies. This effect which is related to the Ti layer can be argued to be associated to a different distribution of the electric field lines within the junction or to an increase of the recombinations at the surface (due to the different contact topology). No effect of the contact resistance is thought to be responsible for this difference (specific contact resistance $\rho_c = 5{\cdot}10^{-7}$ $\Omega$cm$^2$ from TLM measurements which gives less than 3 $\Omega$ for an A6 type device). Regarding the dark current, $I_s$ is below 20-30 nA which is in agreement with previous values reported for UTC-PDs [10].

#### 3.3.2.2 P-I characteristics

I-V characteristics have been recorded for impinging powers (corrected by the 4 dB loss factor) of 6, 9, 12 and 15 dBm. The conversion dBm to mW is given by $P(\text{mW}) = 10^{P(\text{dBm})/10}$. Measurements of the photocurrent as a function of the optical power and the bias voltage provide the responsivity $R = I_{ph}/P_{opt}$, already defined in subsection 1.1.1.1, and the differential resistance from $r_d = \left(\frac{dI}{dV}\right)^{-1}$ corresponding, once evaluated at $V_b$, to the intrinsic resistance $R_i$ introduced in the equivalent circuit model of Fig. 1.8 in subsection 1.1.2.

For what regards these quantities, some preliminary considerations are necessary on the way UTC-PDs are illuminated. In fact, the complex electric field amplitude of a Gaussian beam can be written under paraxial approximation ($\tan(\theta) \approx \theta$ with $\theta$ the angle of incidence defined as the angle between the wavevector and the normal to the interface) for the fundamental $\text{TEM}_{00}$ mode as [11]

$$E(r, z) = E_0 \frac{w_0}{w(z)} e^{\frac{-2r^2}{w^2} - ikz - ik\frac{r^2}{2R(z)} + i\zeta(z)} \tag{3.2}$$

with $r$ and $z$ the radial and axial coordinates, $E_0$ the amplitude of the electric field at $r = 0$, $w(z)$ the waist of the beam defined as the distance from the optical axis at which the electric field amplitude falls to $1/e$ of its maximum value ($w_0$ is the minimum waist at the focus), $k$ is the wavevector modulus in the vacuum equal to $2\pi/\lambda$, $R(z)$ is the radius of curvature of the wavefront at position $z$ and $\zeta(z)$ is the Gouy phase shift. A useful parameter to treat Gaussian beam propagation is the



 

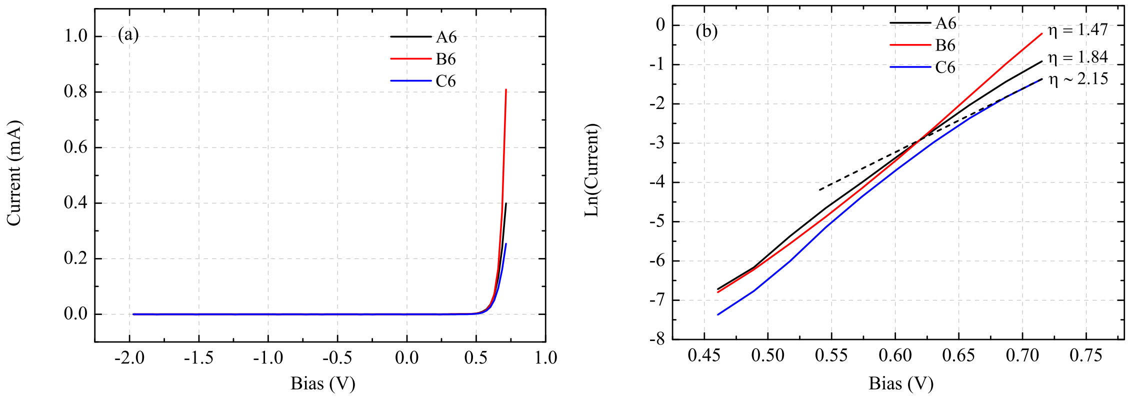


Fig. 3.16: I-V characteristics for A6, B6, C6 type devices in the range -2 V - 0.6 V (a) and natural logarithm of the current to obtain the ideality factor (b).

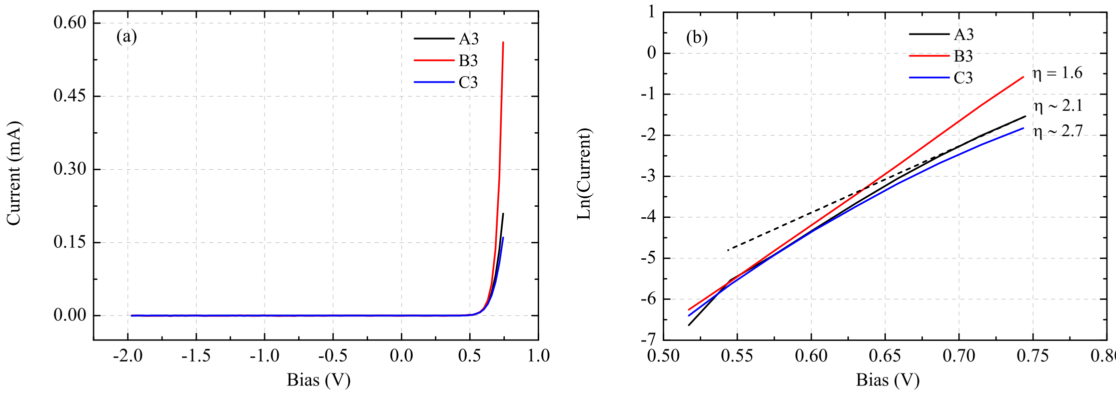


Fig. 3.17: I-V characteristics for A3, B3, C3 type devices in the range -2 V - 0.6 V (a) and natural logarithm of the current to obtain the ideality factor (b).

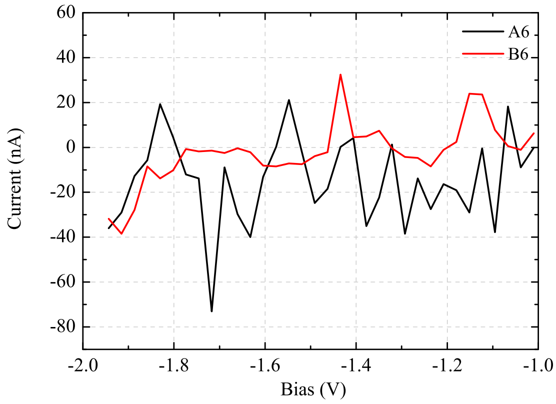


Fig. 3.18: Dark currents for an A6 and a B6 type devices.

Rayleigh range defined as

$$z_R = \frac{\pi {w_0}^2}{\lambda} \tag{3.3}$$

This parameter represents in first approximation how fast a Gaussian beam diverges. In our case, $z_R = 4.56$ $\mu$m by using $w_0 = 1.5$ $\mu$m for the lensed fiber (value furnished by the manufacturer). The dependence of the waist from the distance $z$ can be then written as [11]

$$w(z) = w_0 \sqrt{1 + \left(\frac{z}{z_R}\right)^2} \tag{3.4}$$

At the minimum spot size ($w(z) = w_0$) the wavefront of the Gaussian beam is a plane wave ($R(0) = \infty$). For increasing $z$ the wavefronts become curved according with the following expression

$$R(z) = z\left(1 + \left(\frac{z_R}{z}\right)^2\right) \tag{3.5}$$

During the measurements, it has been observed that a shift $\Delta z$ from the optimal height $z_0$ (associated to the 3-$\mu$m-side device) was necessary to achieve the maximal photocurrent for the 4-$\mu$m-side ($\Delta z = 2$ $\mu$m) and for the 6-$\mu$m-side ($\Delta z = 4$ $\mu$m) device, measured thanks to a graduated differential micrometer screw. Such an effect was present even under low optical powers and it has been attributed to the anode contact's optical properties. In Fig. 3.19 is represented in a schematic way the effect of a defocusing on the wavefront. By taking the phase of Eq. 3.3 and fixing the value of $z$, the only term that depends on the distance $r$ from the optical



 

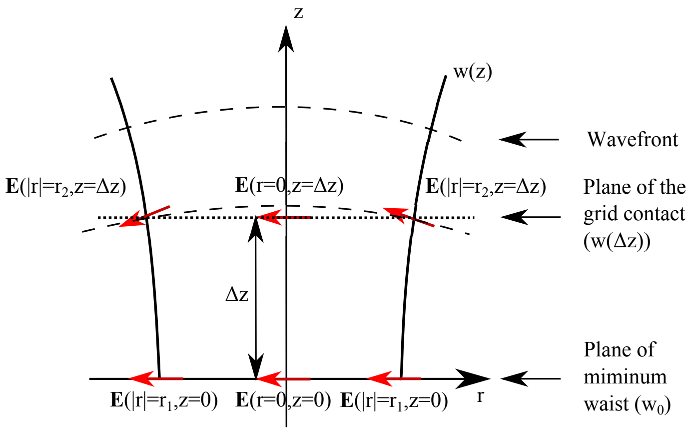


Fig. 3.19: Schematic of the evolution of a Gaussian beam. The electric field vector is no more perpendicular to the z-axis for a shift from its minimum waist position ($z = 0$).

axis is $\phi_1 = kr^2/2R(z)$. By calculating this term for $\Delta z = 2$ $\mu$m and $r_2 = 2$ $\mu$m and for $\Delta z = 4$ $\mu$m and $r_2 = 3$ $\mu$m (see Fig. 3.19) using Eq. 3.5, it can be found that the electric field vector has a phase delay with respect to the electric field vector in $r = 0$ of 37.5° in the case of a 4-$\mu$m-side and of 113.2° in the case of a 6-$\mu$m-side. However, from Eq. 3.3 it is evident that the spot size increases due to the defocusing. The electric field will have a lower maximal value, but it will be spread over a larger surface increasing ET and so the photocurrent due to a better uniformity of the field. However, this phase delay will be a problem due to the coherent nature of ET. Moreover, even though the phase of the electric field is not fully constant at the plane of the device during the illumination, the impinging power is not affected considerably by the defocusing. In fact, the angle obtained between the electric field vector and its projection on the contact surface (calculated with Eq. 3.5 and simple trigonometry) is of 9.3° for the 4-$\mu$m-side and of 19.0° for the 6-$\mu$m-side devices. No further considerations will be done due to the complex way in which these two aspects (no constant impinging power and no coherent diffraction) are related with the trasmission in the grids. Finally, it is worth to notice that in the case of the 3-$\mu$m-side devices the real impinging power is roughly (by considering a circle and not a square surface) 86% of the total amount at the end of the fiber accounting for the waist of 1.5 $\mu$m. However, the impinging powers are not corrected by this factor because of the complex geometry of the surface as discussed above. From these considerations, it is evident that the effective responsivity of the fabricated devices can be increased further in the case of devices with a larger surface than the mode field diameter ($2w_0$).

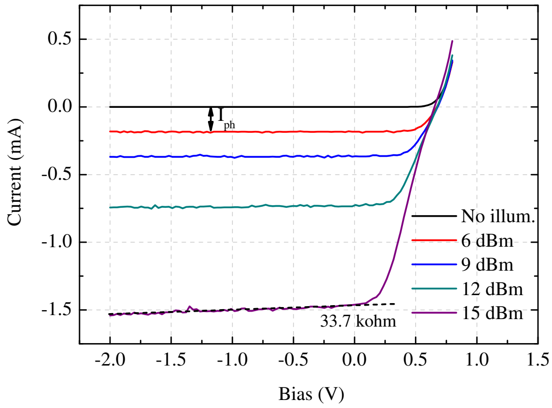


Fig. 3.20: I-V characteristic for a D3 type UTC-PD at different impinging optical powers.

As it can be observed in Fig. 3.20, at high impinging powers the differential resistance becomes lower. This means that the intrinsic resistance $R_i$ of the equivalent circuit model (see Fig. 1.8) cannot be neglected anymore. This behavior results from the increased carrier densities that lower the effective built-in barrier in a similar way as the application of a direct bias voltage does in a p-n diode.

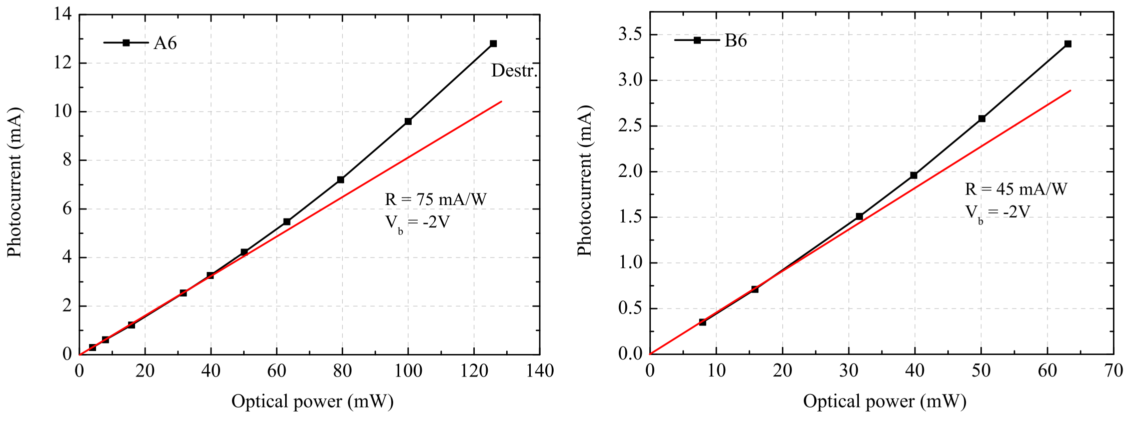


Fig. 3.21: Optical power versus photocurrent for an A6 and B6 type UTC-PDs at $V_b$ = -2 V. At high injected powers the linearity is not maintained anymore.

Another effect that has been observed under high optical powers during P-I measurements at a fixed bias voltage $V_b = -2$ V is a deviation from the linearity relation between the photocurrent and the optical power. This aspect is thought to be related to a decrease of the energy gap for the absorption region due to an increase of the PD's temperature [12]. In fact, a decrease of the energy gap for the InGaAs layer leads to a higher absorption coefficient and a consequent higher photocurrent. This effect was also observed to be reversible in agreement with this explanation. At 135 mW and $V_b = -2$ V the A6 type UTC-PD was destroyed and its I-V characteristic was that one of a short-circuit. This non-linear behavior has been observed for all the devices subjected to high optical powers. The responsivity values for the different devices, calculated at low photocurrents, are reported in Tab. 3.4 with values obtained by applying the COMSOL model introduced in the previous chapter. These results lead to the following conclusions regarding the optical properties of the contact:

- The contact's size and the geometry are important factors for the optical absorption.
- The A6 type UTC-PD shows the highest responsivity as expected (to remember that it presents a covered surface of 50% compared with the 21% one of C6 type UTC-PD), see Tab. 3.3.
- By decreasing the contact's size the extraordinary transmission decreases as seen by comparison of A4, C4 and D4 type UTC-PDs which show nearly the same responsivity as expected.
- By further decreasing the contact's size, the absorption results slightly higher for the devices with a larger uncovered surface as seen by comparison of A3 and D3 type UTC-PDs.
- The Ti layer has the effect of decreasing by nearly a factor 2 the responsivity. The effect is related to the classical absorption in the Ti layer.
- The D3 type UTC-PD presents the highest responsivity among 3-$\mu$m-side devices.
- The calculated values with a plane wave approximation are pretty different from the experimental ones. This can be related to an overestimation of the

absorption coefficient (see C6 which has 21% of covered surface) and to reflections at the grid contact. Moreover, the computed values are obtained considering the dimension parallel to the strips as infinite (2D model) which is of course not the case in the devices. However, the ratio between the different responsivities is well-maintained confirming that the calculations are able to predict which contact will be more efficient.

It can be also remarked that these responsivities are higher than those obtained in the previous thesis (45 mA/W and 29 mA/W for 4 and 3-$\mu$m-side devices). This can be explained by the different illumination, by the fact that no AR coating was used in the previous structures, by the enhancement of the optical absorption thanks to the grid contact topology and by the thicker absorption region (150 nm instead of 100 nm).

Table 3.4: Experimental/theoretical responsivities and differential resistance for the different geometries at $V_b$ = -2 V and, for $R_i$, $P_{opt}$ = 15 dBm.

| Ref. | $R_{exp}$ (mA/W) | $R_{th}$ (mA/W) | $R_i$ (kΩ) |
|---|---|---|---|
| A3/A4/A6 | 41/58/75 | 132/165/210 | 40/26/19 |
| B3/B4/B6 | 26/33/38 | 76/89/101 | 116/85/60 |
| C3/C4/C6 | 45/53/66 | 143/150/175 | 28/26/23 |
| D3/D4/D6 | 46/62/66 | 133/149/206 | 30/24/25 |
| E3/E4/E6 | 24/32/32 | 80/85/94 | 222/178/- |

In Fig. 3.22(a) is shown the effect of $V_b$ over a wide range of photocurrents for an A6 type UTC-PD. It is interesting to notice that the previous hypothesis would also explain the lower difference from the linearity for the curve at $V_b = -1$V as the achieved temperature is lower due to a lower Joule heating. Fig. 3.22(b) reports the behavior of the photocurrent at low optical powers (21 dBm = 125.9 mW) as a function of the bias voltage. For the lower curves ($P_{opt}$ = 19 and 20.5 dBm) there is no appreciable difference in the photocurrent for an increase of $V_b$ up to 3 V. This is due to the built-in electric field which is strong enough to allow the PD to operate even without bias for low photocurrents. This is the main difference with respect to photoconductors which instead have to be always biased for their correct operation.

Another interesting characteristic is the quadratic behavior of the RF power as a function of the photocurrent (see Fig. 3.23 for B4 and C6 type devices). The reason of lower quadratic coefficients, reported in the legend, than the theoretical ones of

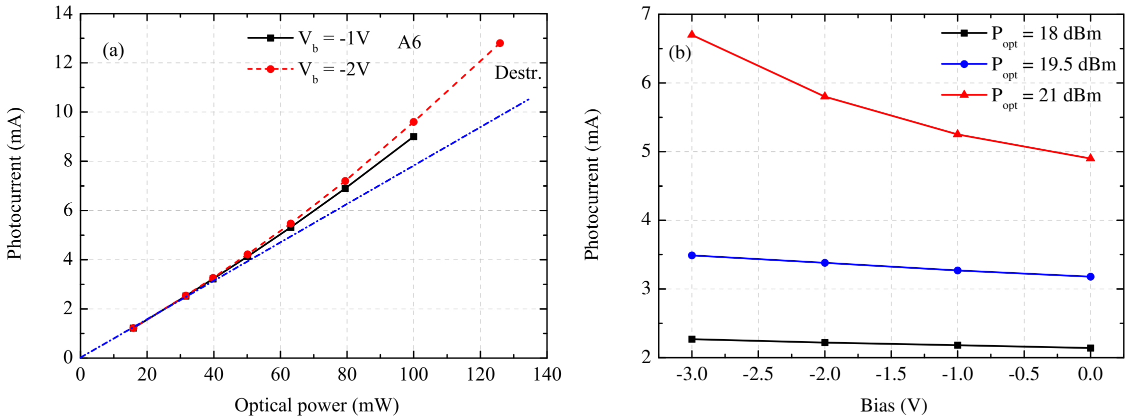


Fig. 3.22: Photocurrent as a function of the optical power and of the bias voltage. (a) shows the photocurrent response for an A6 type UTC-PD at $V_b$ = -2 V and -1 V, (b) shows the behavior of an E4 type UTC-PD for low optical powers in the range $V_b$ = [0,-3] V.

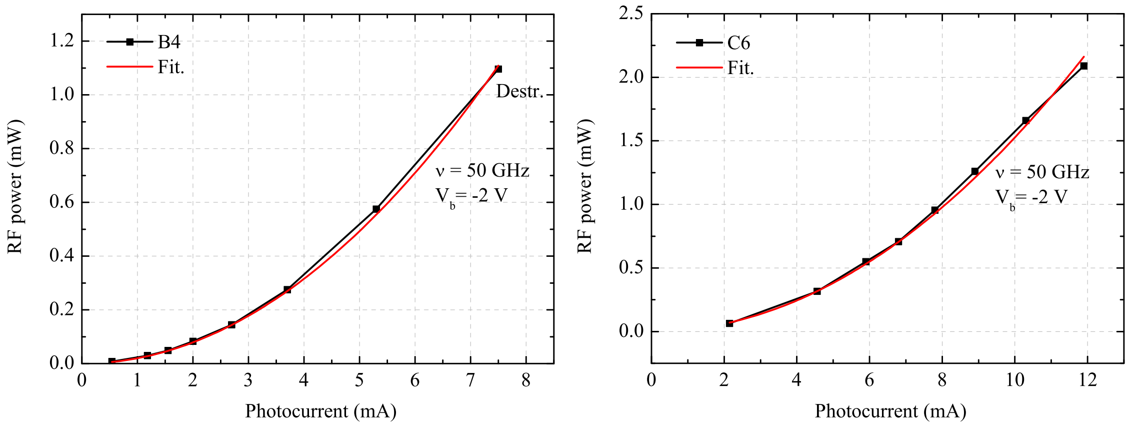


Fig. 3.23: RF power at 50 GHz as a function of the photocurrent for a B4 (quadratic coefficient: 19.7 Ω) and a C6 (quadratic coefficient: 15.3 Ω) type UTC-PDs at bias voltages of -2 V.

25 Ω (see Eq. 1.26 subsection 1.2.2.1) is due to the difference between $I_{ph}^{DC}$ and $I_{ph}^{AC}$. In particular, for UTC-PDs with a larger size, the capacitance is higher and the quadratic coefficient decreases faster due to the lower cut-off frequency. A second issue to be noticed is that, even at high photocurrents (just before destruction), the RF power follows almost perfectly a quadratic law. This may suggest that, notwithstanding the deviation from the linearity of the photocurrent as a function of the optical power, the RF power is not affected by it. This is equivalent to adfirm



 

that the non-linear contribution to the photocurrent at high optical powers is a fast contribution to the photocurrent (can be modulated at high frequencies). Moreover, this would support the previous hypothesis regarding the change in the energy gap of the absorption region. It is remarkable to observe that a power of 2.1 mW has been achieved at 50 GHz with a photocurrent of 11.9 mA at an optical power of 141 mW.

Another aspect that has been investigated is the effect of the bias voltage at high optical power on the RF power generated. Fig. 3.24 shows the enhancement of the RF power generated at 300 GHz by a D3 type UTC-PD. In particular, the saturation of the RF power can be achieved by gradually increasing the bias voltage keeping constant the impinging optical power. An RF power of 394 $\mu$W at a photocurrent of 12.7 mA has been achieved with an optical power of 200 mW by applying a bias voltage of -1.5 V. A further increase to $V_b = -1.65$ V led to the destruction of the device for a photocurrent of 12.9 mA after a short period of time (order of a few seconds). It is interesting to calculate the optical and overall (optical plus electrical) efficiencies of the device. The optical efficiency can be defined as the ratio between the RF generated power to the optical power: $\eta_{opt} = \frac{P_{RF}}{P_{opt}}$, while the overall efficiency takes into account the power provided by the generator through the bias voltage and can be defined as $\eta_{tot} = \frac{P_{RF}}{P_{opt}+P_{el}}$ with $P_{el} = I_{ph}V_b$. Here, $\eta_{opt} = 2 \cdot 10^{-3}$ and $\eta_{tot} = 1.8 \cdot 10^{-3}$. These values are comparable with the best values found in literature for broadband UTC-PDs at 300 GHz [13, 14]. Moreover, considering a surface of $9 + 1.8 = 10.8$ $\mu$m$^2$, the current density at the junction is $J_{junc} = 118$ kA/cm$^2$. However, the ohmic contact for a D3 type covers only $1.8 + 0.3 \cdot 3 \cdot 3 = 4.5$ $\mu$m$^2$ thus the current density at the contact is $J_{cont} = 284$ kA/cm$^2$. In the previous thesis, the highest current densities achieved were 100 kA/cm$^2$ for a 2-$\mu$m-diameter UTC-PD at $V_b = -0.4$ V and 85 kA/cm$^2$ for a 4-$\mu$m-diameter UTC-PD at $V_b = -0.85$ V [1]. In that case $J_{junc}$ and $J_{cont}$ coincided due to the contact geometry (see Fig. 3.11). Here, $J_{cont}$ is considerably higher and, due to the low specific contact resistance for Pt and Ti over p-InGaAs, the failure because of the electrical properties of the contact can be excluded. This is not so surprising, in fact the product $I_{ph}^2 \cdot R_s$ gives less than 1 mW for a series resistance of a few $\Omega$. A more interesting value is the one of $J_{junc}$ which is only slightly higher than the one found in the previous thesis. The reason may be related to the mechanism of failure which is the junction breakdown due to the accumulated carriers at the interface absorbing/collector region which can induce fields higher than 500 kV/cm (breakdown field for InP) [15]. This effect has been already addressed as one of the possible causes of failure of PIN and UTC-PDs [15].

In Fig. 3.24 is shown the dynamic effect of the bias voltage over the RF power for high optical powers. The saturation of the RF power and the consequent destruction of the device suggest that the collector is the critical part of the device. However, thermal aspects should have a non-negligible influence as observed by many groups, especially on their RF characteristics [15, 16, 17]. In fact, the possibility of employing high optical powers combined with high bias voltages has led to RF powers as high as 400 $\mu$W at 300 GHz before the destruction of the device. It is interesting to notice that this value of RF power coincides with the maximal one predicted by Feiginov based on drift-diffusion simulations for a device with 13-$\mu$m$^2$-section at 300 GHz with $V_b = -1.5$ V and absorption and collector regions of 98 and 282 nm, respectively [5]. Moreover, the value obtained represents the highest power ever measured in literature from a UTC-PD at 300 GHz in a broadband configuration. However, the integration with an antenna may lead to lower powers depending on the antenna radiation efficiency and impedance. The highest value reported in a resonant configuration (1.2 mW at 300 GHz for two combined UTC-PDs) has been achieved in 2012 at NTT laboratories by exploiting a $\lambda/4$ transformer and a microstrip-to-waveguide transition as already mentioned in the state-of-the-art section [18].

In the previous work, an RF power of 1 $\mu$W at 300 GHz for a 3-$\mu$m-side device was obtained at a photocurrent of 1.26 mA and bias voltage of -0.35 V for an impinging power of 43 mW and an RF power of 20 $\mu$W at 300 GHz for a 4-$\mu$m-side device was obtained at a photocurrent of 5.6 mA and bias voltage of -0.7 V for an impinging power of 120 mW [19]. However, due to the small number of available UTC-PDs (related to the antenna integration which occupies a lot of space on the sample), no measurements were done for the RF power under conditions close to their failure. Thus it is not possible to make an absolute comparison of the RF performances which strongly depends on several factors like the bias voltage, the heating, the illumination or the technique of measure (on-wafer or free-space) [1].

At an optical power of 140 mW and bias voltage of -2 V, the B4-type UTC-PD of Fig. 3.23 transformed within a few seconds in a short-circuit. Such a change has been observed for all the devices that have been destroyed. The change in the



 

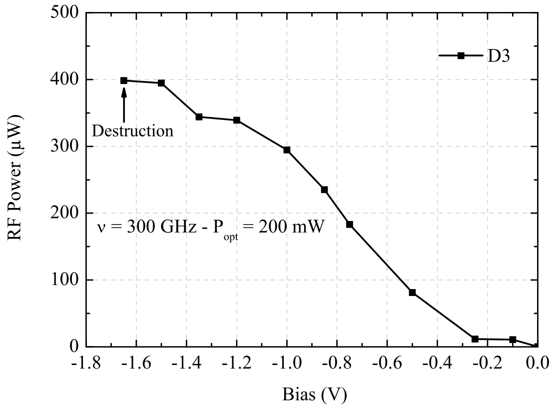


Fig. 3.24: RF power as a function of the bias voltage for a D3 type UTC-PD at an optical power of 200 mW.

device's structure can be observed in the SEM images of Figs. 3.25 and 3.26. From all the SEM images, it seems to be that the main concerned region is located almost at the center, opposite to the strip that shorts the whole grid. This effect can be explained by considering the symmetry of the contact along the plane parallel to the strips, the effect of the perpendicular strip which reflects the E-field and the mesa facets which may deteriorate faster due to defects with respect to internal regions. Moreover, the region that starts to melt is likely correlated to the highest optical field density.

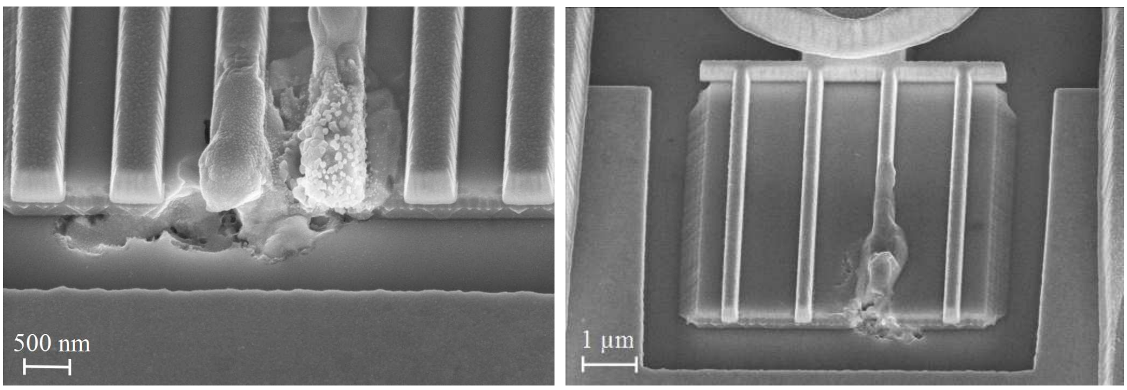


Fig. 3.25: Example of an A6 (left) and a C6 (right) type devices after burnt-out.

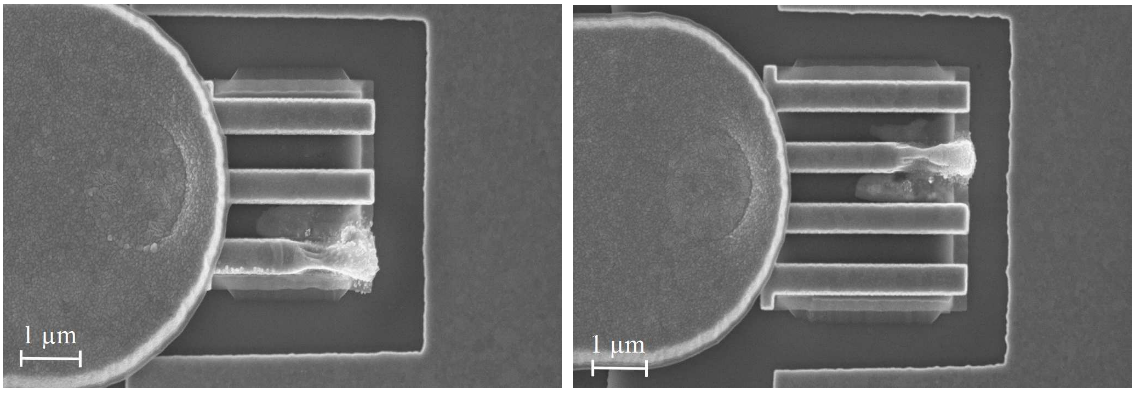


Fig. 3.26: Example of a B3 (left) and B4 (right) type devices after burnt-out.

#### 3.3.2.3 P-$\nu$ characteristics

One of the main characteristic of PDs for THz generation is their frequency response as already widely discussed from a theoretical point of view in the first chapter. Fig. 3.27 report the P-$\nu$ characteristic behavior for an A3, A4 and A6 type (a) and D3, D4 and D6 type (b) devices. The RF powers reported in the range 5-110 GHz have been calculated from the corresponding measurements by applying the following conversion factor

$$f_{conv} = \left( \frac{I_{ph}^{h}}{I_{ph}^{l}} \right)^{2} \tag{3.6}$$

where $I_{ph}^{h}$ and $I_{ph}^{l}$ are the photocurrents measured in the J band and in the range 5-110 GHz for the original measurements, respectively. The conversion factor (in the order of 4-5) takes into account the fact that the photocurrent has been increased for the measurements with the calorimeter in the J band due to its sensitivity and to the low generated power compared to previous measurements at lower frequency. As expected due to the capacitance which is higher for 6-$\mu$m-side devices the roll-off happens first than for 4 and 3-$\mu$m-side devices. The difference between 4 and 3-$\mu$m-side devices is much weaker due to the other poles which are equivalent (see Tab. 3.5). In particular, it can be seen that in the range 30-100 GHz the situation is quite different showing a roll-off of only 9 dB/dec for 4 and 3-$\mu$m-side devices and of roughly 20 dB/dec for 6-$\mu$m-side devices. While the latter is expected due to the *RC* pole at around 78 GHz, the roll-off of 9 dB/dec is related to the fact that the *RC* pole is not present at those frequencies (located above 160 GHz) and thus the roll-off



 

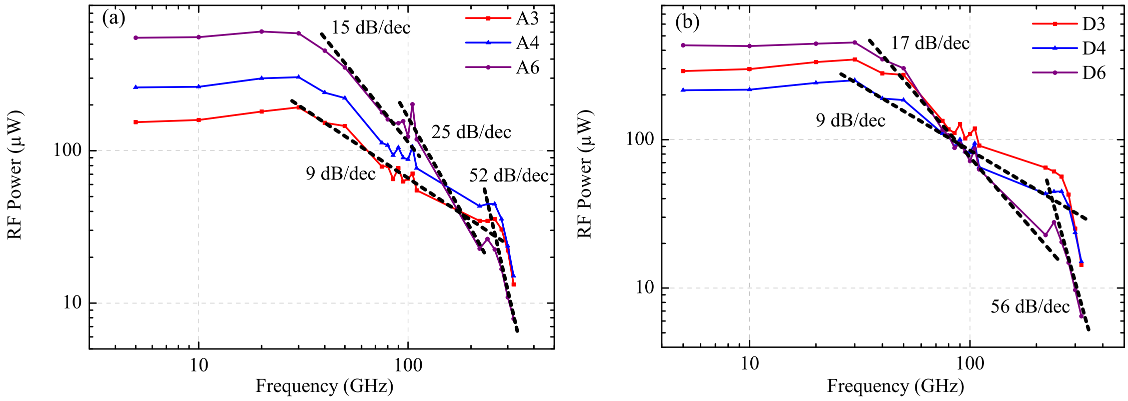


Fig. 3.27: RF power as a function of the frequency. The values in the range 5-110 GHz have been scaled with the conversion factor $f_{conv}$.

Table 3.5: Theoretical and experimental (cut-off) frequencies of the different poles for 3,4 and 6-$\mu$m-side devices. For the collection region, a transit time of 1 ps has been used ($v_s = 1{\cdot}10^7$ cm/s) and for the absorption region of 0.32 ps. Units are GHz.

| Cut-off Freq. | 6-$\mu$m-side | 4-$\mu$m-side | 3-$\mu$m-side |
|---|---|---|---|
| $\nu_{RC}$ | 78 | 161 | 265 |
| $\nu_a$ | 498 | 498 | 498 |
| $\nu_t$ | 443 | 443 | 443 |
| $\nu_{-3dB}$ | 75 | 139 | 193 |
| $\nu_{-3dB}^{exp}$ | 65 | 70-75 | 65-70 |

value extrapolated from the values in W band (75-110 GHz) is a combined effect of the 3 poles which have a complessive theoretical cut-off frequencies (-3 dB) at higher frequencies (139 and 193 GHz for 4 and 3-$\mu$m-side devices, respectively). In fact in Fig. 3.27(a) the roll-off at low frequencies can be even divided in an initial one of 15 dB/dec and an other at higher frequencies of 25 dB/dec. The oscillation of the power seen in the W-band (75-110 GHz) is related to resonances within the probe waveguide. In the J-Band (220-325 GHz) the behavior in terms of roll-off is similar for all the devices (measured around 50-60 dB/dec). However, such a roll off is higher than expected at those frequencies as it can be observed in Tab. 3.5 which presents the frequency location of the theoretical and experimental cut-off frequencies. This difference is clearer in Figs. 3.28 and 3.29 which compare the experimental data for devices with and without a Ti layer and theoretical curves. The adding of a Ti layer is shown to play no major role in the frequency response for any device size.



 

Regarding the difference between experimental and theoretical curves, a possible explanation could be related to the onset of saturation effects for the measurements in the J-band due to the fact that, in order to have a high sensitivity of the detector, the photocurrent was increased above 4-5 mA. This issue may also explain the discontinuity between the measurements in W and J bands. Moreover, it can be also seen that a small difference in the values of the load resistance and capacitance for a 3-$\mu$m-side device (see Fig. 3.29) from their theoretical ones of around 12 fF and 50 Ω can modify quite considerably the frequency response. The uncertainty in the capacitance value is estimated within at least few fF (for 3-um-side devices) from the nominal one due to under-etching and resist mask precision, while the series resistance for smaller devices and the uncertainty in the load resistance can be up to 10-20 Ω higher than the nominal one.

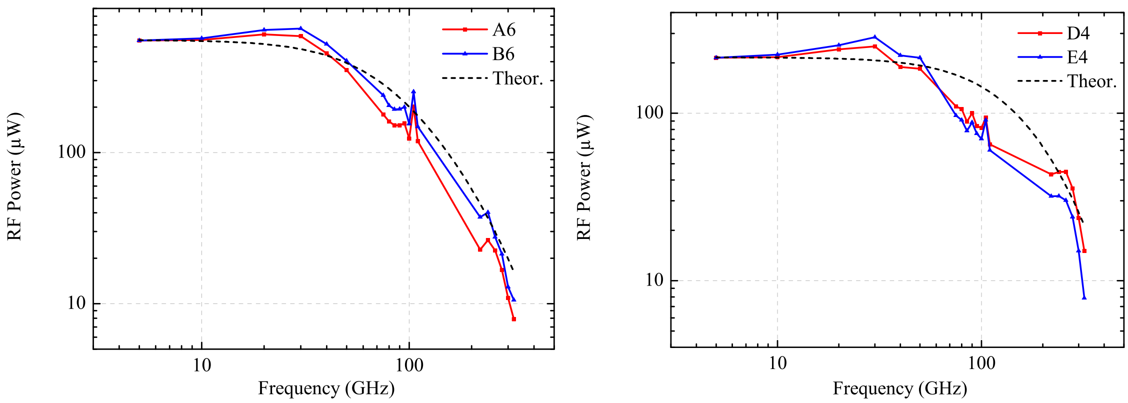


Fig. 3.28: RF power as a function of the frequency. The values in the range 5-110 GHz have been scaled with the conversion factor $f_{conv}$.

It can be noted also that the measurements in W band may look underestimated compared to the theoretical curves. A possible reason for this disagreement could be related to the GSG probe in W band which presents an imaginary part of the impedance that has a non negligible effect for devices with lower capacitances. This could explain why for 6-$\mu$m-side devices this discontinuity is apparently absent. Further measurements will be performed in the future to clarify these points.

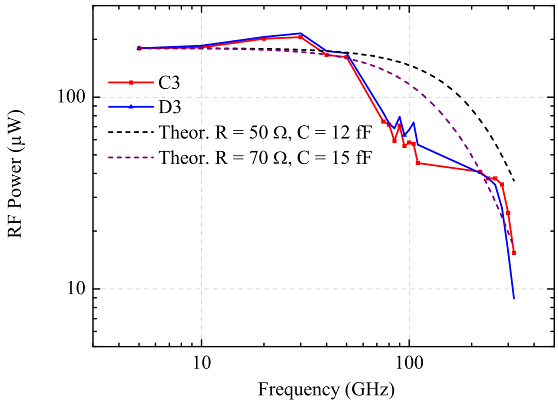


Fig. 3.29: RF power as a function of the frequency. The values in the range 5-110 GHz have been scaled with the conversion factor $f_{conv}$.

## 3.4 Conclusions

Top-side illuminated UTC-PDs have been fabricated and measured by on-wafer measurements. The devices have shown good performances in terms of responsivity as well as generated RF powers. A non-linearity has been observed in the photocurrent as a function of the optical power. This effect has been attributed to a heating of the PD which reduces the energy gap increasing the optical absorption and the consequent photocurrent. The responsivities obtained by simulations are larger than those effectively measured, however the ratio between different contact topologies is in agreement with measured values. In particular, the calculations are useful to estimate which contact topology is more suitable for high responsivities. Before device destruction, RF powers as high as 2 mW at 50 GHz and 400 $\mu$W at 300 GHz have been measured for a 6-$\mu$m-side and a 3-$\mu$m-side UTC-PDs with no matching circuits. The value at 300 GHz represents the highest value ever obtained without matching circuits by UTC-PDs. Moreover, state-of-the-art optical ($2{\cdot}10^{-3}$) and total ($1.8{\cdot}10^{-3}$) efficiencies have been achieved at 300 GHz. This study has also led to the validation of the concept of a sub-wavelength contact for increasing the responsivity of UTC-PDs (to recall that resonant optical cavity configurations can be implemented to increase further the total optical path length), while providing a contact which is able to sustain high current densities (higher than 100 kA/cm$^2$) and work properly even at high frequency.



 

# Bibliography

[1] A. Beck, *Réalisation et charactérisation de photodiodes á transport unipolaire pour la génération d'ondes terahertz*, Ph.D Dissertation - University of Lille I (2008)

[2] Ed. Mohamed Henini (Hg.), *Molecular beam epitaxy: from research to mass production* (Elsevier, 2013)

[3] Marian A. Herman et al., *Epitaxy: physical principles and technical implementation* (Springer-Verlag, 2004)

[4] Ed. Robin F. C. Farrow, *Molecular beam epitaxy: applications to key materials* (Noyes Publications, 1995)

[5] M. N. Feiginov, *Analysis of limitations of terahertz p-i-n uni-traveling-carrier photodiodes*, J. Appl. Phys. **102**, 084510 (2007)

[6] Y. Pang, C. Genet, and T. W. Ebbesen, *Optical transmission through subwavelength slit apertures in metallic films*, Opt. Commun. **280**, 10 (2007)

[7] www.cst.com

[8] Kim-Lu Wong, *Planar antennas for wireless communication* (John Wiley & Sons, 2003)

[9] A. Joshi and S. Datta, *High-speed, large-area, p-i-n InGaAs photodiode linear array at 2-micron wavelength*, Proc. SPIE 8353, Infrared Technology and Applications XXXVIII, 83533D (2012)

[10] T. Furuta, T. Ito, Y. Muramoto, H. Ito, M. Tokumitsu, and T. Ishibashi, *D-band rectangular-waveguide-output uni-travelling-carrier-photodiode module*, Electron. Lett. **41**, 715 (2005)

[11] Orazio Svelto, *Principles of lasers - 5th Edition* (Springer, 2010)

[12] Neil W. Ashcroft and David N. Mermin, *Solid state physics* (Harcourt college publishers, 1976)

[13] E. Rouvalis, C. C. Renaud, D. G. Moodie, M. J. Robertson, and A. Seeds, *Traveling-wave uni-traveling carrier photodiodes for continuous wave THz generation*, Opt. Exp. **18**, 11105 (2010)

[14] E. Rouvalis, C. C. Renaud, D. G. Moodie, M. J. Robertson, and A. J. Seeds, *Continuous wave terahertz generation from ultra-fast InP-based photodiodes*, IEEE Trans. Microwave Theory Techniques **60**, 509 (2012)

[15] K.J. Williams, *Comparisons between dual-depletion-region and uni-travelling-carrier p-i-n photodetectors*, in *IEE Proc.-Optoelectron., Vol. 149* (2002)

[16] M. Chtioui, A. Enard, D. Carpentier, S. Bernard, B. Rousseau, F. Lelarge, F. Pommereau, and M. Achouche, *InGaAs-InP uni-traveling carrier photodiodes for high power capability*, in *20th International Conference on Indium Phosphide and Related Materials, 2008* (2008)

[17] T. Yasui, T. Furuta, T. Ishibashi, and H. Ito, *Comparison of power dissipation tolerance of InP/InGaAs UTC-PDs and pin PDs*, IEICE Electron. Expr. **9**, 1 (2003)

[18] H.-J. Song, K. Ajito, Y. Muramoto, A. Wakatsuki, T. Nagatsuma, and N. Kukutsu, *Uni-travelling-carrier photodiode module generating 300 GHz power greater than 1 mW*, IEEE Microwave Wireless Compon. Lett. **22**, 363 (2012)

[19] A. Beck, M. Zaknoune, E. Peytavit, T. Akalin, G. Ducournau, J.-F. Lampin, F. Mollot, F. Hindle, C. Yang, and G. Mouret, *Terahertz photomixing in InP/InGaAs UTC-PD integrated with TEM horn antennas*, in *Proc. 33rd International Conference on Millimeter and Terahertz Waves, 2008 (IRMMW-THz 2008)* (2008)

# Chapter 4

# Metal mesh filters based on sub-wavelength apertures for THz applications

Dielectric losses at THz frequencies are one of the main problems for free-space devices such as filters, metamaterials and plasmonic devices due to the high absorption coefficient of commonly employed dielectric materials. Recently, the cyclic olefin copolymer (COC) has been proven suitable for a wide range of applications like THz fibers, low-loss interconnects and waveguides, owing to to its remarkable properties at THz frequencies. In what follows, it will be shown that such a material is a valuable candidate for free-space devices through the realization of a high-pass, low-loss, broadband mesh filter with cut-off frequency at 1 THz. This device is suitable for integration in experiments concerning UTC-PDs for measuring properly low powers at frequencies above 1.5-2 THz with incoherent detectors.

## 4.1 Cyclic olefin copolymer properties and related THz applications

Here, the main properties of COC will be briefly illustrated. The focus will be especially on its transmission properties in the THz region, in particular it will be shown its superiority in terms of losses compared to the most commonly used dielectrics. Finally, a few recent THz applications involving its use will be presented.



 

### 4.1.1 Main properties of the cyclic olefin copolymer

The chemical structure of COC, known under the trade name of Topas®, consists of linear and cyclic olefins which form the repeating structural unit of the copolymer (see Fig. 4.1). This material presents many remarkable properties like an amorphous character, high transparency in the UV and visible, possibility to be molded allowing a re-shaping of the material and chemical resistance [1, 2]. In contrast to other polymers widely employed even in the THz region, this material is intrinsically non-polar (no net localized charges in its structure which induce dipoles similarly to the case of the water molecule) and it has a much lower absorption coefficient in the THz region compared to the majority of polymers commonly used like polytetrafluoroethylene (Teflon®) or the polyimide (Kapton®). In fact, as it can be observed in Fig. 4.2, the absorption coefficient of COC is lower than 3 cm$^{-1}$ over the whole THz region (0.2 cm$^{-1}$ at 1 THz) and two orders of magnitude with respect to Teflon® or Kapton® for certain frequencies. This feature allows potentially to fabricate devices with broadband properties for several applications where THz waves are employed.

Furthermore, COC presents processing temperatures which are lower compared to

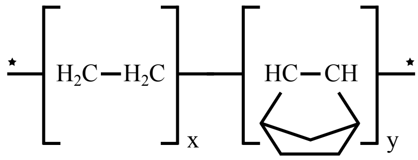


Fig. 4.1: Repeating structural unit of COC consisting of linear and cyclic olefins.

other polymers like the benzocyclobutene (BCB) which has a low absorption coefficient at 1 THz ($\alpha = 2$ cm$^{-1}$), but requires a cure baking at 250°C [4, 5]. Such a baking has been found to be detrimental for its mechanical properties due to different expansion coefficients between the dielectric film and the host substrate on which BCB is spin-coated [6]. Moreover, during the hard-bake, potential oxigen contamination may change strongly its optical properties [4]. Another advantage of COC consists in the possibility of achieving films by spin-coating with a desired thickness ranging from 3-4 $\mu$m to 40-50 $\mu$m by multiple layer deposition and using COC resists with different dilutions. This feature gives more freedom compared to polymers like polypropylene ($\alpha = 2.1$ cm$^{-1}$ at 1 THz) in processes where the thickness of the film is a crucial aspect of the design [7]. Generally, membranes obtained



 

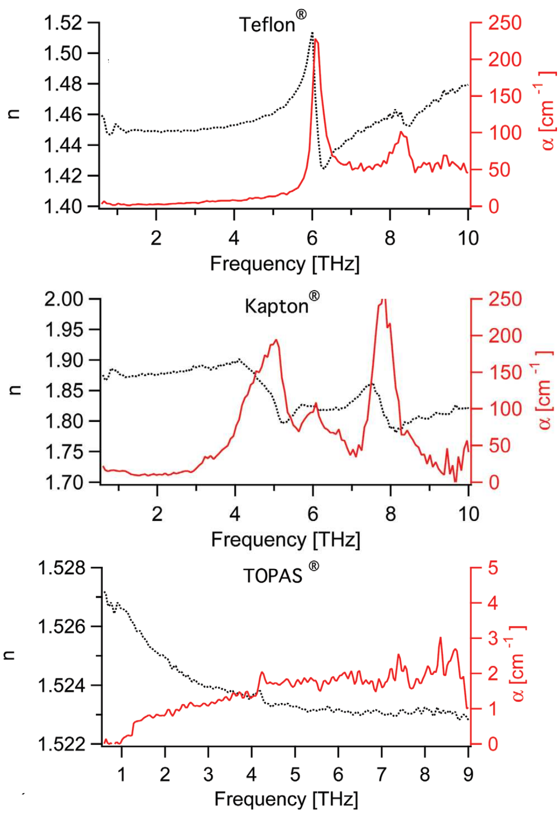


Fig. 4.2: Optical properties of COC compared with Teflon and Kapton, both dielectrics widely used in THz applications, from Ref. [3].

commercially by other techniques (injection molding, compression molding, thermoforming etc.) with specific thicknesses (order of a few tens of $\mu$m) and no possibility of deposition by spin-coating have a lower surface quality which can turn out to be detrimental for achieving high pattern resolutions during processing. This issue has been observed in the fabrication of metamaterials for THz frequencies based on polypropylene membranes which shown defects grain-like of the size of 6-10 $\mu$m as reported in Fig. 4.3 [8]. Finally, differently from the case of materials like Teflon® or polypropylene, metals have a much better adhesion on COC surfaces [9, 10].



 

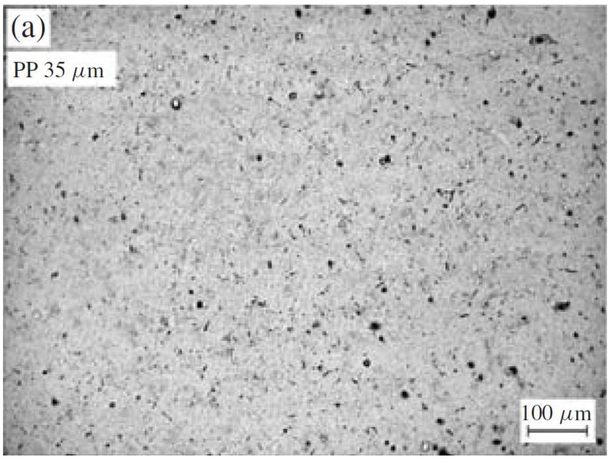


Fig. 4.3: Optical transmission micrograph of a 35-$\mu$m-thick PP film, from Ref. [8].

### 4.1.2 THz applications employing the cyclic olefin copolymer

Due to its remarkable properties in the THz region, COC has been already used to fabricate low-loss THz fibers, reported in Fig. 4.4, achieving an absorption coefficient $\alpha < 0.4$ cm$^{-1}$, low-loss interconnects based on thin film microstrip (see Fig. 4.5) and grounded-CPW technology with an absorption coefficient $\alpha < 1.75$ dB/mm up to 220 GHz and directional couplers [2, 5, 11]. It has also a large potential in the microfluidic field for biosensing applications due to its high hydrofobic behavior and to the strong response of many biological substances at THz frequencies [12].

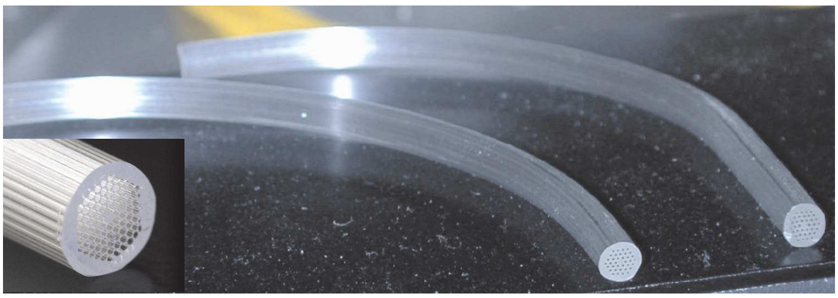

Fig. 4.4: A THz fiber in COC realized by a drawing tower. The inset shows the micro-structure of the fiber with 250-$\mu$m-diameter drilled apertures, from Ref. [2].



 

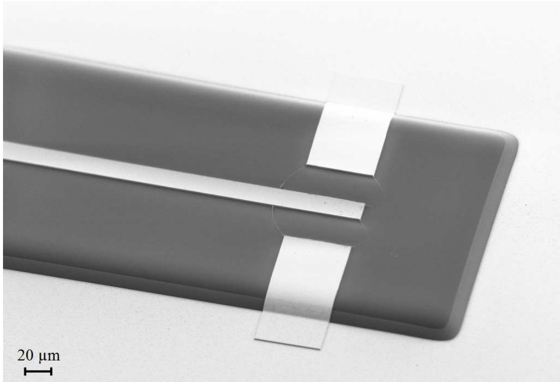


Fig. 4.5: Thin film microstrip line realized on a 5.8-$\mu$m-thick COC fabricated by Dr. E. Peytavit (see Ref. [5]).

## 4.2 Broadband low-loss mesh filters for THz applications

In this section it will be firstly explained the interest of developing broadband highly transparent filters at THz frequencies for photomixing experiments at RT. Then, there will be presented some basics of metal mesh filters and the exploited design with the major constraints which have to be taken into account. Finally, the fabrication and the transmission measurements from a few hundreds of GHz up to 10 THz by THz-TDS and synchrotron light characterization will be illustrated.

### 4.2.1 Motivations for broadband high-pass filters at THz frequencies

One of the most serious limitations of THz sources based on photomixing is their low generated powers above 2-2.5 THz, especially for broadband configurations (few tens of nW) [13, 14, 15]. Powers at these frequencies are generally measured with Golay cells and bolometers at RT or at cryogenic temperatures to increase the signal-to-noise ratio. An important figure of merit for detectors is the noise-equivalent-power (NEP), measured in W/Hz$^{0.5}$, which is defined as the power needed to achieve a signal-to-noise ratio equal to 1 after an integration time of half a second for a bandpass of 1 Hz. While this value is quite low for state-of-the-art detectors at cryogenic temperatures (from a few aW/Hz$^{0.5}$ to a few fW/Hz$^{0.5}$, commercial closer to 100 pW/Hz$^{0.5}$), detectors working at RT present NEP values which are definetely larger (order of 100 pW/Hz$^{0.5}$ or higher) [16, 17, 18]. Even though, for a single measurement the integration time may be of several seconds or minutes, for imaging and fast spectroscopic applications shorter integration times and high sensitivity are more suitable to avoid long scanning periods [19].

Two main advantages of photomixers are their intrinsic broadband character and the RT operation as already widely discussed in the first chapter. These two features are important for practical spectroscopic systems which should not need cryogenic bulky systems. However, in order to have a good signal-to-noise ratio, powers to be detected (which above a few THz are in the order of tens of nW or lower) do not have to be reduced by any sort of passive component included in the detection path, especially for powers close to the noise floor of the detector. Unfortunately, a problem which arises in photomixing experiments is the generation of a background noise coming from the photomixing of all the frequency components present in the spectrum of the lasers due to the amplified spontaneous emission (ASE) effect in the EDFA. Furthermore, as the efficiency of photomixers is higher at lower frequencies, this contribution may not be negligible on the overall detected power, even though the dynamic range of the laser power at the output of the EDFA is 30 or 40 dB. This issue can be solved by placing a high-pass filter in front of the detector in order to suppress the spurious contribution at lower frequencies. However, such a filter has to be also broadband in order not to reduce the tunability of the photomixers and, finally, it has to be highly transparent for what mentioned above regarding the NEP of RT detectors (short integration times) and due to the noise floor of incoherent detectors at THz frequencies like Golay cells ($>$ 0.1-0.2 nW) or pyroelectric sensors ($>$ a few tens of nW) [19, 20, 21, 22, 23]. To fulfill these requirements a high-pass metal mesh filter based on a thin COC film has been developed.

### 4.2.2 Basic concepts of mesh filters

Metal meshes have been used since 60's in far-infrared optics, in particular for astronomical applications. Since then, they have been used extensively as filters, beam splitters and reflectors in different domains like imaging, sensing and detection [24, 25, 26]. Different types of filtering properties can be achieved depending on the mesh pattern. The most common ones, reported in Fig. 4.6, are inductive (high-pass behavior) and capacitive (low-pass behavior) filters. These filters can be described in a first approximation with an equivalent electric model. In Fig. 4.7

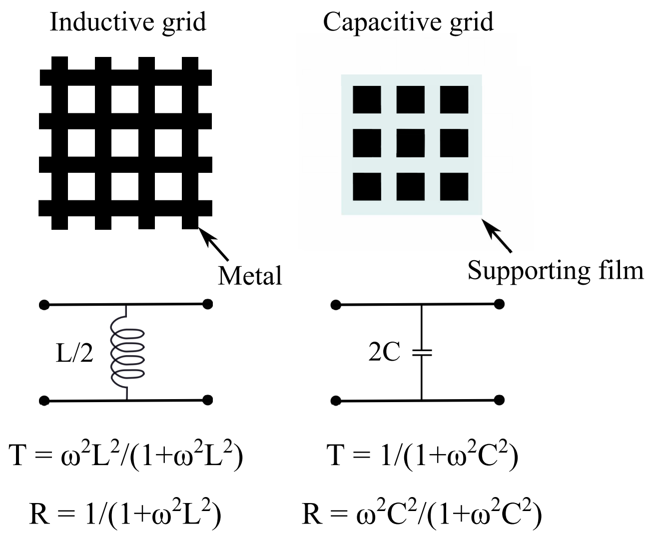


Fig. 4.6: Design of inductive and capacitive mesh filters with their related equivalent circuits and corresponding transmission ($T$) and reflection ($R$) functions. $\omega$ is the normalized angular frequency and the parameters $C$ and $L$ are the normalized capacitance and inductance values, respectively.

are plotted the transmittance and reflectance coefficients for an inductive grid with $L = 10$. In this model there are no losses or diffraction effects. For complementary capacitive grids, the transmittance and reflectance curves have to be exchanged due to their complementary analytical form (Babinet's principle) as reported in Fig. 4.6. Here, it can be seen that in order to have a high-pass behavior, an inductive filter has to be adopted. In this case, for wavelengths much larger than the period, the mesh behaves like a metal sheet by strongly reflecting the impinging electric field.

### 4.2.3 Mesh filter design

The equivalent electric model introduced previously holds for thin substrates (if not free-standing) compared to the wavelength, for thin mesh widths compared to their thicknesses, far from the diffraction and, in a single element model, for perfect metals. The last two assumptions can be removed by inserting in the equivalent circuit other elements to obtain an LC circuit and a resistor which can only approximately model the diffraction and the non-zero penetration depth in metals. Moreover, the



 

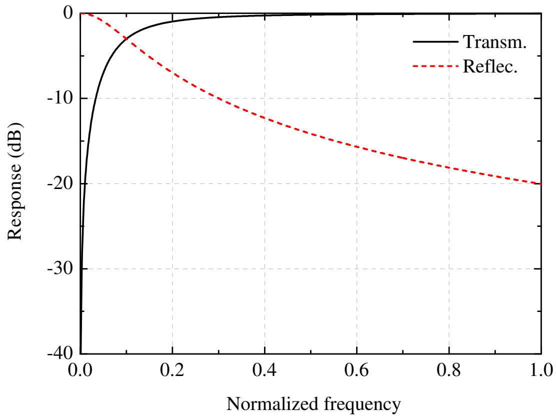


Fig. 4.7: Response of an inductive filter with the equivalent circuit model of Fig. 4.6 ($L = 10$).

main parameters of such a model have to be determined by fitting experimental curves or through pre-compiled tables depending on the design. These aspects are resumed in Fig. 4.8 which reports a first example of application of this equivalent model to experimental transmittance results for a capacitive filter showing that a single element model can work well only for low frequencies and that adding a second element can improve the data fitting and take into account diffraction. A more accurate model like CMM, introduced in the second chapter, could be used to treat this type of structures. However, even though such an approach would provide better results for the design, it still considers the substrate as infinitely thick. Unfortunately, at THz frequencies and for substrates of a few tens of $\mu$m, the influence of the finite thickness of the substrate can be non-negligible. Ultimately, modifications of the main mesh design are not taken into account with the analytical and quasi-analytical methods. For all these reasons, a 3D full-wave electromagnetic simulator based on a finite integration technique (CST Microwave Studio) has been used [27].

#### 4.2.3.1 Filter requirements

It is worth to remind that a squared-lattice mesh filter (inductive filter) can be considered as an infinite array of coupled waveguides with propagation constant



 

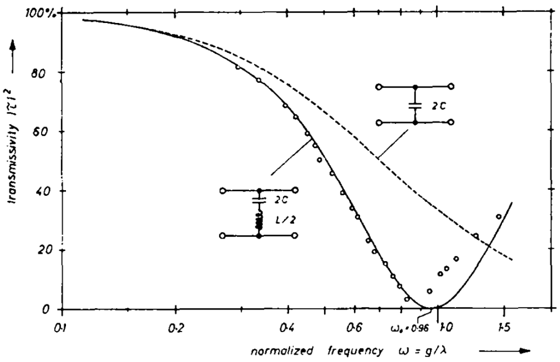

Fig. 4.8: Transmittance as a function of the normalized frequency (to the inverse of the period) for a capacitive filter and data fitting with a single and double element models, from Ref. [24].

given by [28]

$$q_z = \sqrt{k_\omega^2 - \frac{\pi^2(n^2+m^2)}{a^2}} \tag{4.1}$$

where $k_\omega$ is the wavevector in vacuum as already defined, $a$ is the mesh aperture given by the period length $p$ minus the mesh width $w$ and $m, n$ is a couple of positive integers starting from zero, excluded the couple (0,0). The above expression is the classical formula for finding the propagation constants associated to the different TE and TM modes in a squared waveguide. Another point to recall is that for a free-standing periodic squared array, diffraction appears at wavelengths given by

$$\lambda_{m,n} = \frac{p}{\sqrt{m^2+n^2}} \tag{4.2}$$

These two basic considerations lead to the following conclusions to design a high-transparency broadband filter:

1. It is necessary to work in the sub-wavelength regime (evanescent propagation in the waveguide apertures).

2. The mesh width has to be as small as possible.

3. Free-standing (no substrate) structures are very difficult to be employed.

4. The substrate has to present low losses over a large band.

Point 1. is related to the diffraction, in fact a lattice with aperture $a = 150$ $\mu$m would give a real propagation constant for a frequency $\nu > 1$ THz, but it would also lead to a first diffraction minimum close to 2 THz (assuming a negligible mesh width). Point 2. is related to point 1. because of the reflection at the metal surface which needs to be reduced as much as possible. Point 3. is related to point 1. and point 2. due to the evanescent character of the propagation and to the reflection at the surface which does not allow, for high transmittances, to use a mesh with widths and, in particular, thicknesses of several $\mu$m. Free-standing meshes would not be mechanically stable in the case of sub-$\mu$m dimensions for widths or thicknesses. Finally, point 4. is essential to achieve a high transparency in the pass-band. In fact, in the THz region is quite difficult to achieve a broadband high transparency transmission due to the absorption coefficients of conventional substrates. Fig. 4.9 shows a first example for capacitive (low-pass) filters with different polymide substrate thicknesses (lower curves). Their transmittance spectra in the pass-band are strongly affected by the optical properties of the polymide film (upper curves with $T < 70\%$), particularly in the 24-35 $\mu$m band where a 10-$\mu$m-increase of the thickness changes drastically the properties of the filters. In the conclusions of the article of Ref. 29, the authors of the work suggested that another material with lower losses or a polymide thickness of only 1-2 $\mu$m should be used as substrate. However, such a thickness would result in a decrease of the mesh stability apart from limiting the design due to the impossibility of embedding metal meshes with thicknesses of 1 $\mu$m or higher. In Fig. 4.10 are reported the transmittance spectra of a single-layer (measured) and a triple-layer (measured and calculated) inductive filters. The meshes are embedded in polyimide films with a 17-$\mu$m-separation between them for the triple-layer filter. The authors of this work have decided to place the cut-off frequency far away from the two absorption bands of polyimide at 15 and 30 $\mu$m in order to avoid absorption in the pass-band. Moreover, even though with a triple-layer filter the rejection ratio can be improved as seen in Fig. 4.10, the transmittance value is strongly affected and achieves a maximum value of only -5 dB ($T < 31.6\%$).

#### 4.2.3.2 Electromagnetic model

The model implemented in the electromagnetic solver is reported in Fig. 4.11. Periodic boundary conditions have been applied in x and y directions. PMLs have



 

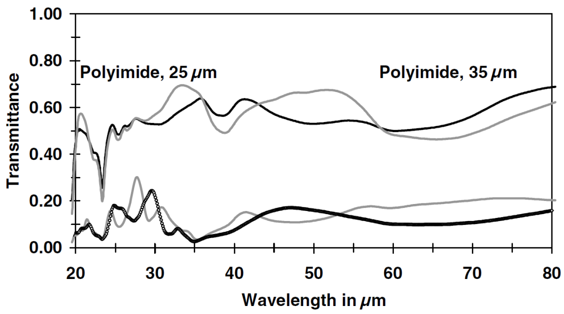


Fig. 4.9: Upper curves are related to the transmission of 25-$\mu$m-thick (grey line) and 35-$\mu$m-thick (black line) films of polyimide. Lower curves report the transmittance spectra of two capacitive cross-shape meshes with a 25-$\mu$m-thick (grey line) and a 35-$\mu$m-thick (black line) films, from Ref. [29].

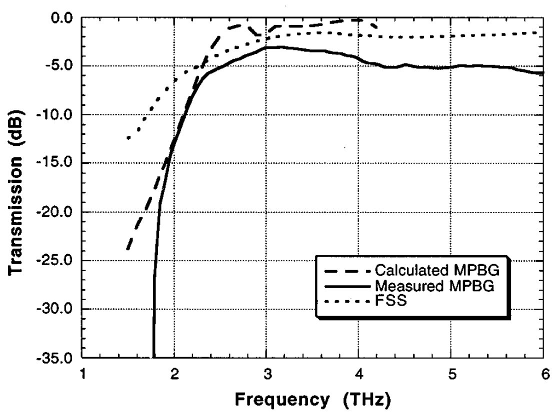


Fig. 4.10: Transmittance spectra for a single-layer measured (dot line) and a triple-layer measured (solid line) and calculated (dashed line) inductive mesh filters, from Ref. [25].

been applied in z direction at a distance of $\lambda_c/8$ with $\lambda_c$ the central wavelength of the calculation range ($\lambda_c = 60$ $\mu$m and frequency range 0 - 10 THz). Floquet's modes (which are the equivalent of Bloch waves in solid state physics) have been used at the input and output ports to take into account the periodicity of the structure [30]. The metal has been modeled as a 300-nm-thick Au layer with a DC conductivity and penetration depth of the electric field given by

$$\delta = \frac{1}{\sqrt{\pi \nu \mu_0 \sigma_{\mathrm{Au}}}} \tag{4.3}$$



 

with $\sigma_{\mathrm{Au}} = 4.07 \cdot 10^7$ S/m and the vacuum magnetic permeability $\mu_0 = 4\pi \cdot 10^{-7}$ H/m. The COC substrate is modeled with an approximated Debye model [31]. The

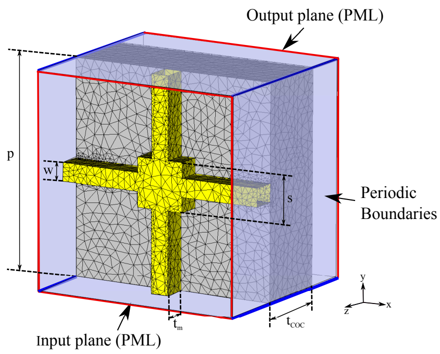


Fig. 4.11: Design of the structure considered with tetrahedral mesh and periodic boundaries (light blue transparent planes) in x and y directions and input/output planes in z direction (red bordered).

model requires only the absorption coefficient ($\alpha = 2$ cm$^{-1}$ at 9 THz) and the real permittivity ($\epsilon_r = 2.32$ at 9 THz) where 9 THz is the highest frequency at which optical parameters for COC are available [3]. A fitting procedure is then applied to the ordinary Debye model given by

$$\epsilon_r(\omega) = \epsilon_\infty + \frac{\epsilon_s - \epsilon_\infty}{1 + i\omega\tau_r} \tag{4.4}$$

where $\tau_r$ is the dielectric relaxation time, $\epsilon_s$ and $\epsilon_\infty$ are the static and high frequency real permittivities and $\omega$ is the angular frequency. The fitting procedure leads to an approximation of the dielectric function for the range of frequencies considered. Such an approximation holds because no resonances (which are usually modeled as Lorentz oscillators) are present in the THz spectrum of the material (see Fig. 4.12).

The mesh employed is tetrahedral with a minimum number of mesh cells per wavelength (with respect to the upper limit of the frequency range - 10 THz) of 8 and automatic mesh adaptation based on S-parameters. In Figs. 4.13(a) and (b) is illustrated the effect of the mesh width and its thickness (parameters are contained in Tab. 4.1 for the different simulations) on the zero order transmission. First of all, it can be noticed that, as expected, the transmittance value increases by decreasing either the width or the thickness of the mesh.



 

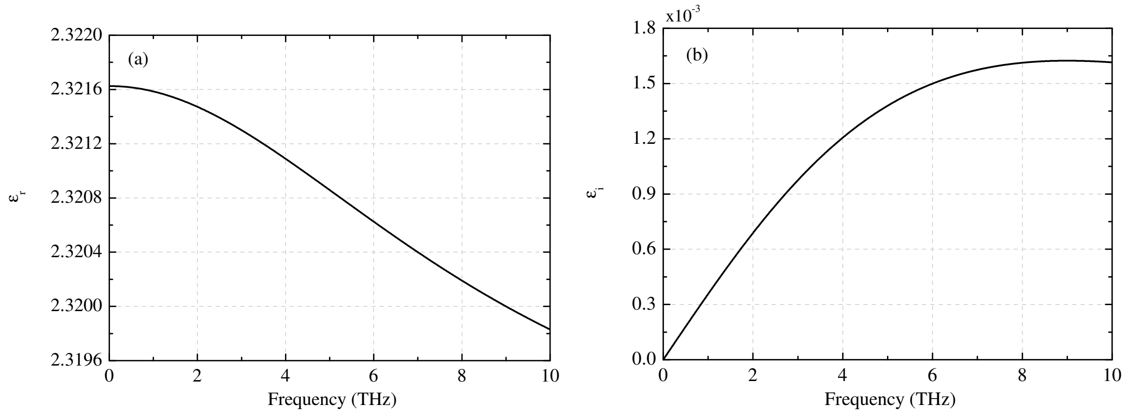


Fig. 4.12: Relative permittivity obtained from the fit of a first order Debye model. (a) shows the real permittivity part $\epsilon_r$, while (b) reports the imaginary one $\epsilon_i$.

Due to the sub-wavelength mesh aperture and to its thickness, the rejection ratio in the stop-band is not really high (13 dB/decade). However, a solution well-known in literature to improve it consists in considering a stack of meshes as already seen in Fig. 4.10 [24]. In order to demonstrate that such a possibility is feasible, single and double-layered structures will be considered later. For what concerns the substrate, its effect is to modulate the transmission, even though the modulation is not exactly the one of a Fabry-Pérot cavity due to the fact that in the sub-wavelength regime the field, after having passed through the apertures, scatters similarly to a spherical-like wave and the thickness of the substrate (compared to the effective wavelength) is not sufficient to recover a plane wave wavefront by overlapping of all the contributions. In particular, optimum values have been found to achieve a cut-off (-3 dB) frequency at around 1 THz and a broadband character for a bandwidth of 5 THz above 1.5 THz (transmittance higher than 75%). These parameters and the associated designs (in scale) are reported in Tab. 4.2 and in Fig. 4.14. Their transmittance spectra are reported in the analysis section with the experimental results. For the triple-layer filter, the transmittance has been only calculated to show the further increase in the rejection ratio.

Secondly, a strong minimum is observed at a wavelength close to 6.7 THz. This is related to the diffraction mediated by the substrate. Moreover, the peak red-shifts by reducing the width. This behavior is likely to be related to the condition to resonate in the aperture which changes, in particular for smaller width the aperture is larger and thus the resonance is at lower frequencies. On the contrary, a change in the



 

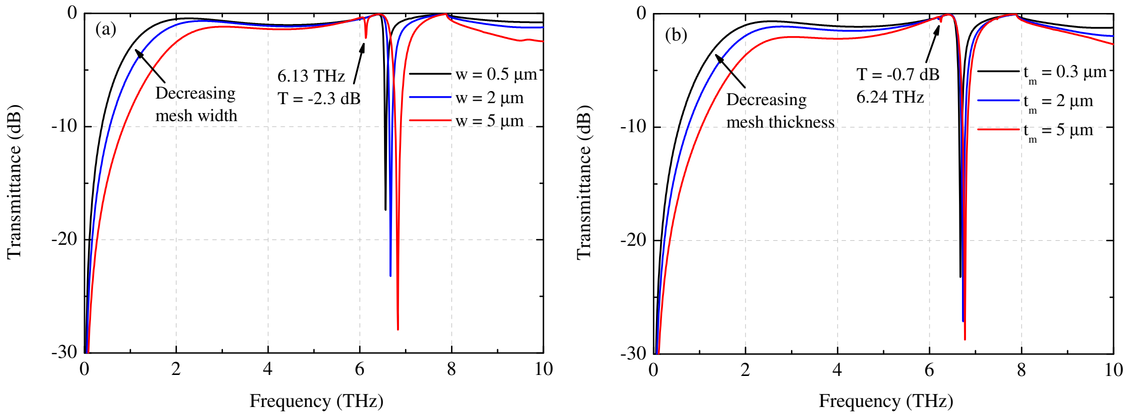


Fig. 4.13: Filter transmittances for different mesh widths $w$ (a) and thicknesses $t_m$ (b). All the other parameters are reported in Tab. 4.1.

Table 4.1: Parameters used for the simulation of Figs. 4.13(a) and (b) (units are $\mu$m)

| | $p$ | $w$ | $s$ | $t_{COC}$ | $t_m$ |
|---|---|---|---|---|---|
| (a) | 38 | var. | 2 | 13 | 0.31 |
| (b) | 38 | 0.5 | 2 | 13 | var. |

mesh thickness does not modify the frequency location of the minimum considerably. Furthermore, a second peak appears evident only for certain choices of parameters. This peak is related also to a resonance in the substrate, but its nature is more complicated. Finally, at the diffraction (7.89 THz) the transmittance decreases and other propagative orders appear.

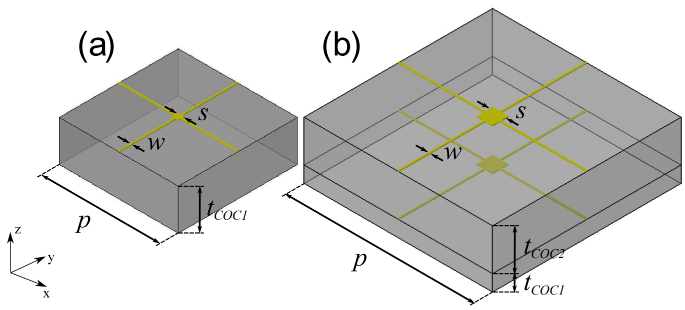


Fig. 4.14: Unit cells of the mesh-filters used for the simulations of the fabricated filters. Figs. 4.14 (a) and (b) show the structures of the single-layer and double-layer filters, respectively. The structures are in scale and their dimensions are reported in Tab. 4.2.



 

Table 4.2: Parameters used in the design of the single-layer, double-layer and triple-layer (only simulated) filters with $\nu_{-3dB}$ at 1 THz (units are $\mu$m)

| | $p$ | $w$ | $s$ | $t_{COC1}$ | $t_{COC2}$ | $t_{COC3}$ | $t_m$ |
|---|---|---|---|---|---|---|---|
| Single | 38 | 0.5 | 2 | 13 | – | – | 0.31 |
| Double | 59 | 0.5 | 5 | 5 | 13 | – | 0.31 |
| Triple | 70 | 0.5 | 5 | 5 | 13 | 13 | 0.31 |

In Figs. 4.15, 4.16, 4.17 and 4.18 are reported the x,y and z-components amplitudes and phases (x-component (a), y-component (b)) of the electric field for the filter of Fig. 4.13(a) with $w = 5$ $\mu$m at the two minima values, 6.13 THz (a) and 6.83 THz (b), respectively. It can be noticed that at 6.13 THz, the x-component has the major contribution and the resonant behavior looks like that one of a dipole (see Fig. 4.18(a)). In this case the y-component of the electric field is not really relevant in terms of magnitude compared to the x-component. Finally, it can be also observed that the majority of the electric field loss is localized at the borders of the strips on the y-direction (see x and z-components).

On the contrary, at 6.83 THz the main contribution of the electric field comes from the y-component and the pattern which is obtained within the substrate is related to surface waves propagating into it (see Fig. 4.18(b)). In this case, the x-component has not a relevant interest, while the z-component is connected to the concentration of the field at the borders of the strips, but this time on the x-direction.

### 4.2.4 Fabrication process

The fabrication process consists in six major steps. In Fig. 4.19 are schematically reported each of these steps. The patterning process is done by e-beam lithography due to the minimum dimension of the design (500 nm). However, it should be mentioned that it may be developed also using deep-UV and immersion lithography which permit to achieve resolutions of around 100-150 nm for cost effective fabrication process.

#### 4.2.4.1 High-definition metal meshes

First, an Al sacrificial layer is deposited over a 2 inches Si wafer by RF sputtering (step a)). Then, COC (Grade T8007 mr-I T85-5.0 XP by micro resist technology) is deposited by spin-coating on top of it (step b)). Initially, the parameters employed



 

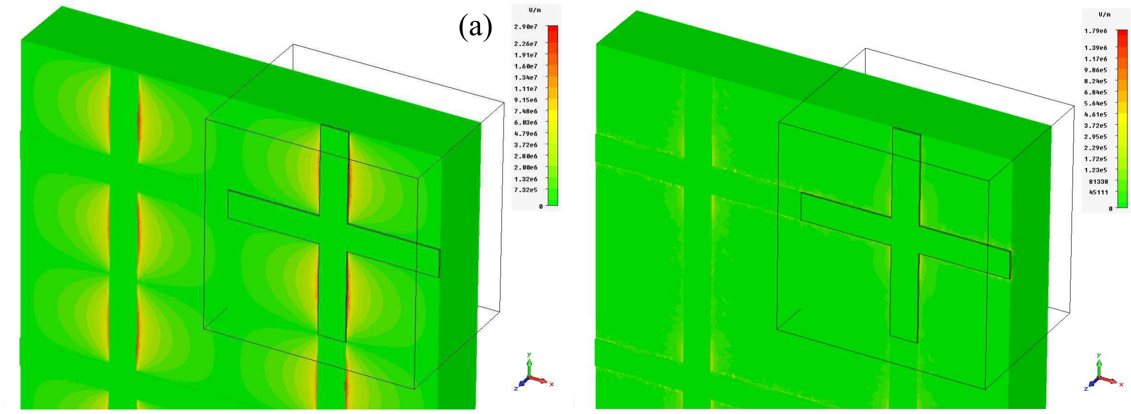


Fig. 4.15: Modulus of the electric field x-component from the simulation of Fig. 4.13(a) with $w = 5$ $\mu$m at 6.13 THz (first minimum) (a) and at 6.83 THz (second minimum) (b).

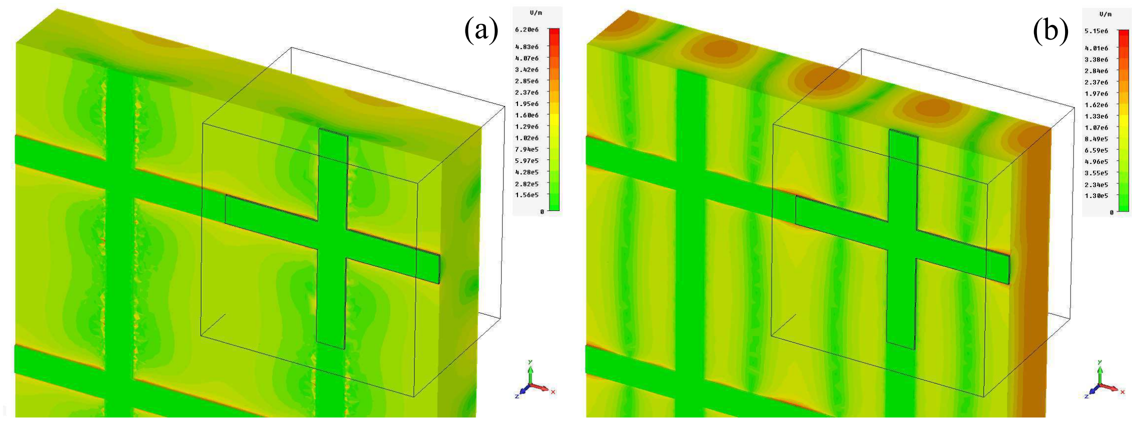


Fig. 4.16: Modulus of the electric field y-component from the simulation of Fig. 4.13(a) with $w = 5$ $\mu$m at 6.13 THz (first minimum) (a) and at 6.83 THz (second minimum) (b).



 

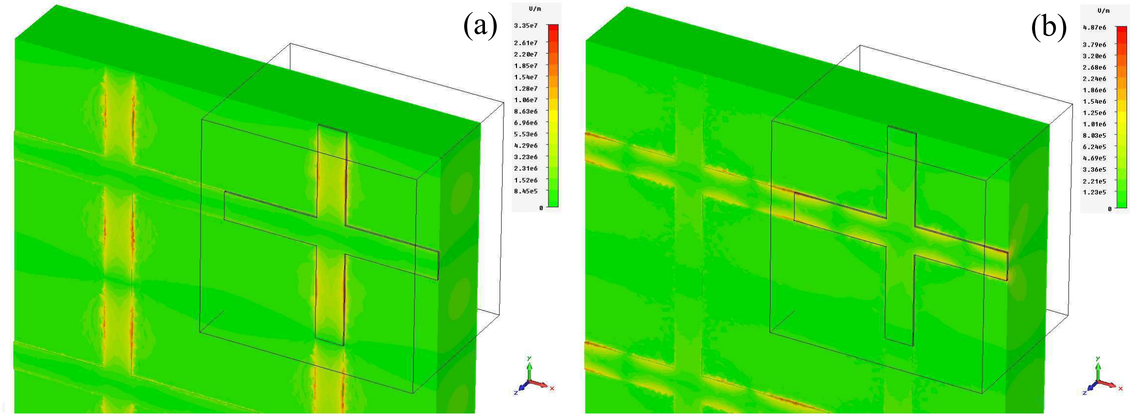


Fig. 4.17: Modulus of the electric field z-component from the simulation of Fig. 4.13(a) with $w = 5\ \mu$m at 6.13 THz (first minimum) (a) and at 6.83 THz (second minimum) (b).

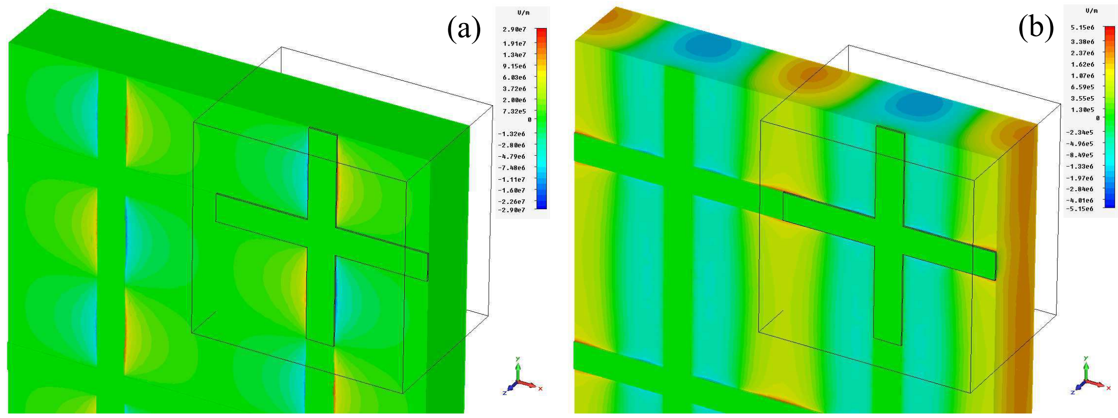


Fig. 4.18: Electric field from the simulation of Fig. 4.13(a) with $w = 5\ \mu$m at 6.13 THz (first minimum) x-component (a) and at 6.83 THz (second minimum) y-component (b).



 

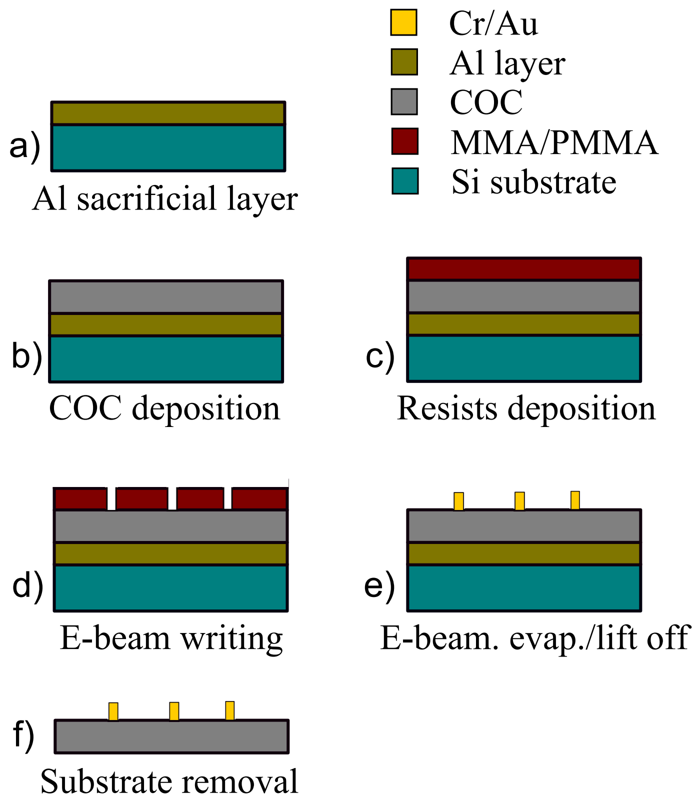


Fig. 4.19: Main steps of the fabrication process for the mesh filters.

where those supplied by the manufacturer. The thickness of the layer has been then controlled by reflectivity measurements (fitting an interference pattern) and, for multiple layer deposition, by measuring the distance with an optical microscope between different focal planes once the film was free-standing (after removal of the sacrificial layer). This allows a measure of the thickness within around $\pm 0.5$ $\mu$m. The reason for which the reflectivity method was not applied is that, after multiple depositions, the surface becomes slightly wavy and not perfectly homogeneous preventing an accurate measure of the reflection at UV wavelengths. A bi-layer of electronic resists is deposited to transfer the mesh pattern (step c)). The resists are then patterned by e-beam lithography and developed in a solvent to remove the exposed regions (step d)). A Cr/Au (10/300 nm) metallization is deposited by e-beam evaporation and a lift-off process, already described in chapter 2, is employed to remove the exceeding metal and remaining resist (step e)). Finally, a chemical etching is necessary to remove the Al sacrificial layer obtaining the free-standing



 

COC film with the mesh (step f)). Steps from b) to e) are repeated once again for a double-layer filter before step f). As it can be seen in Fig. 4.20(a) this process leads to high-quality metal patterns with sub-$\mu$m dimensions over large areas. To perform the transmission measurements the 2-inches film has been glued to an annular metal holder (see Fig. 4.20(b)) with an internal diameter of 2 cm. It is worth to notice that throughout the process the film has remained flat.

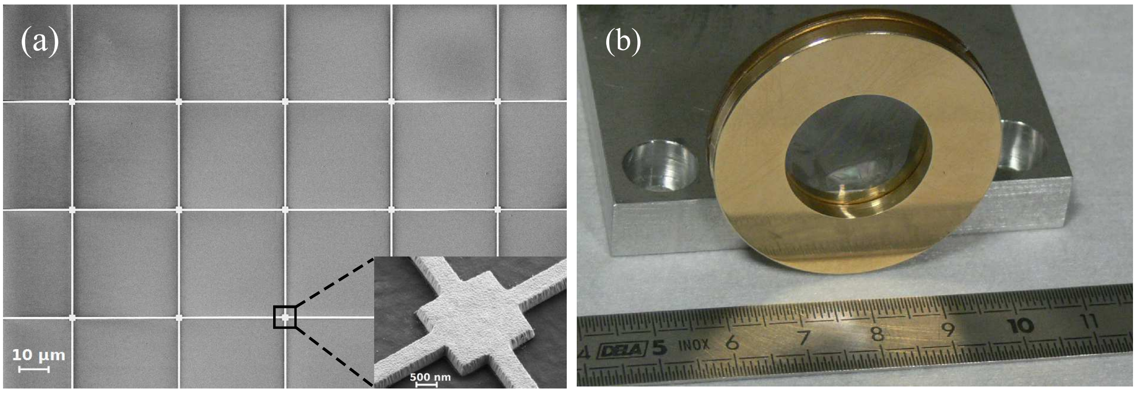


Fig. 4.20: On the left, Fig. 4.20(a) reports an SEM image of the single-layer mesh filter with parameters reported in Tab. 4.2. The inset reveals the high-definition of the mesh with the nominal dimensions well-maintained. On the right, Fig. 4.20(b) reports a photograph of the single-layer filter mounted onto an annular holder. COC high transparency and sub-$\mu$m mesh wires width make the filter hardly visible.

#### 4.2.4.2 Lift-off and metal adhesion problems

The first type of problems observed and reported in Fig. 4.21(a) is well-known in the technology of devices with closed patterns. The main reason for the uncomplete lift-off is that the solvent has a much greater difficulty to penetrate (in order to etch the resist) compared to patterns which have at least one side which is opened. Moreover, the large number of closed patterns/squares (order of $10^4$) obliges to modify the standard lift-off process in order to avoid strongly reflecting defects. This problem has been solved by using ultrasounds for a short period of time before rincing the sample. A second issue connected to the lift-off is the possibility of having patterns which remain stuck to the mesh surface (see Fig. 4.21(b)). Again this problem has been solved by using ultrasounds and by placing the sample during the whole duration of the lift-off with the mesh surface facing the bottom of the beaker. In this situation the patterns which leave the sample fall on the bottom of the beaker by gravity obtaining almost perfectly clean surfaces. A second type of

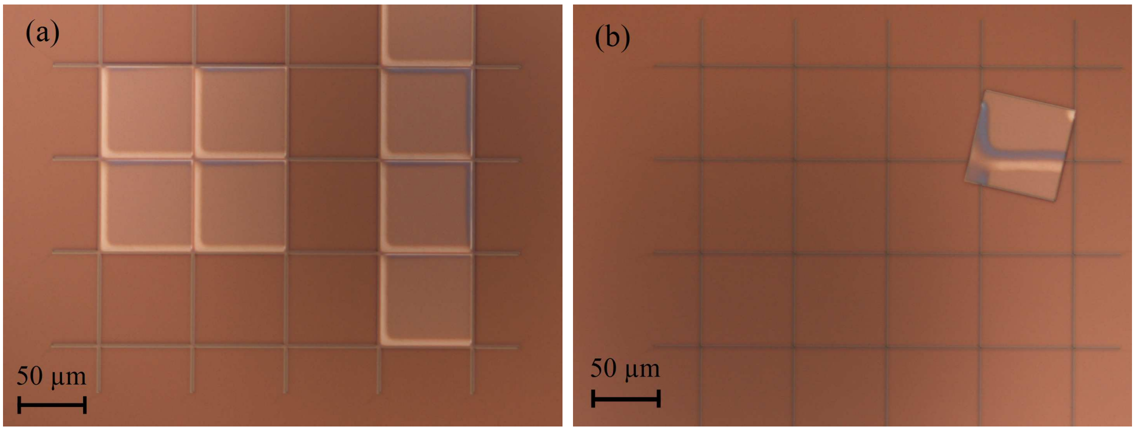


Fig. 4.21: Optical micrographs of two encountered problems after the lift-off step. (a) shows that the metal patterns to be removed may not leave completely the mesh surface ($w$ = 2 $\mu$m). (b) shows that the patterns removed may get stuck at the surface ($w$ = 0.5 $\mu$m).

problems is related to the metal adhesion to the COC's surface. In Fig. 4.22 are reported the results of a test performed by spin-coating a diluted COC resist (500-nm-thick) over a metal mesh. Due to the centrifugal force and to the high viscosity of COC compared to other resists, the mesh may be not well-aligned anymore after deposition (see Fig. 4.22(a)). This problem has been solved by employing a thin layer of Cr (10 nm) which presents a much better adhesion compared to Au or Ti (not reported in Fig. 4.22) and by inserting squared blocks at each mesh cross for increased mechanical stability without any drawback on the EM response (see Fig. 4.22(b)).

### 4.2.5 Experimental setups

Here, two different techniques and related setups for characterizing samples at THz frequencies will be presented. In particular, their working principles will be introduced focusing in particular on their range of frequencies.



 

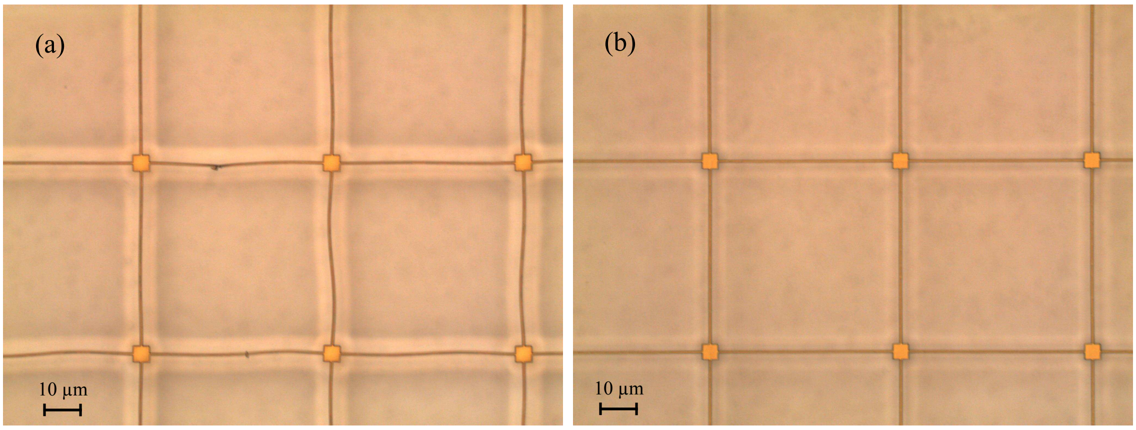


Fig. 4.22: Example of problems related to the metal adhesion for a mesh with dimensions $w$ = 500 nm, $p$ = 65 $\mu$m and $s$ = 5 $\mu$m over a 13-$\mu$m-thick COC film deposited on top of a sacrificial Al layer and a Si substrate. (a) and (b) are related to Au (300 nm) and Cr/Au (10/300 nm) metal mesh patterns, respectively.

#### 4.2.5.1 THz time-domain spectroscopy

The first technique used to characterize the filter transmission is THz-TDS. The setup developed by Dr. Frédéric Garet at the University of Savoie, schematically illustrated in Fig. 4.23, consists of 100 fs - 800 nm pulses coming from a Ti-Sapphire laser pumped by an Ar ion laser with a repetition rate of 82 MHz. The laser signal is separated by a beam splitter into two branches: one for the generation of the THz signal and the other one for its detection. The signal addressed for the generation is modulated with a chopper (whose reference is sent to a lock-in amplifier which tracks the detected signal modulated at the chopper frequency $\nu_M = 1$ kHz to improve the signal-to-noise ratio) and then focused onto a photoconductor based on LT-GaAs polarized at $V_b = 9$ V ($E = 15$ kV/cm). The spectrum, resulting from the generation of photo-carriers within the photoconductor, is radiated thanks to a dipole antenna and collimated through a Si hyperhemispherical lens underneath the photoconductor's substrate. The frequency range covered by the generated spectrum goes from 150-200 GHz up to 2.5-3 THz. The THz signal is collimated by parabolic mirrors and then used to probe the sample in the confocal beam waist at mid-way between the emitter and the detector. The signal which results from the interaction with the sample is re-collected and focused onto an equivalent photoconductor integrated with an antenna and a Si hyperhemispherical lens. The electric field is transfered to the electrodes of the photoconductor where the laser signal coming from the second branch (for the detection) is used to sample the THz signal. The sampling is based on the generation of photocarriers by the laser signal which are accelerated thanks to the THz field applied at the electrodes (collected from the antenna) and, by changing the path of the laser signal through a delay line, it is possible to cover the whole THz signal time extension (maximum delay line time window: 167 ps with steps of 0.98 fs). The electric field is then proportional to the derivative of the photocurrent and thus, from its value, it is possible to obtain the value of the electric field in the time domain [32]. By Fourier transforming the electric field, information regarding the amplitude and the phase of each frequency component can be obtained. Finally, a measure without the sample (see Fig. 4.24(a) and (b)) has to be used as reference (an iris is used to select a spot on the sample) to extract quantitative information regarding the properties of the sample like the complex refractive index or its thickness depending on the known parameters. Here, the focus is only on the attenuation of each frequency component (amplitude information) for which the following relation for the transmittance is used

$$T(\nu) = \left| \frac{E_{sample}(\nu)}{E_{ref}(\nu)} \right|^2 \tag{4.5}$$

where $E_{sample}(\nu)$ and $E_{ref}(\nu)$ are the Fourier transforms of the recorded electric field with and without sample. No preferential polarization has been considered due to the symmetry of the filters and only normal incidence has been used.

#### 4.2.5.2 Synchrotron light source

The second technique is based on the THz spectrum obtained from a particle electron accelerator. The accelerator that has been used is the synchrotron Soleil in Paris (see Fig. 4.27) [33]. The physical mechanism to obtain a broadband THz signal which can be extracted at opportune places of the accelerator storage ring is based on the fact that charged particles, if accelerated, emit radiation [34]. Bunches of electrons are usually deviated by bending magnets (dipolar magnets) to let the electrons following the ring path. However, these elements can be also tuned to provide a radiation with a certain energy (to remember that a change in the velocity direction corresponds to an acceleration) and a precise angle. Other elements that are used to obtain synchrotron radiation are the so-called wigglers which consist of several



 

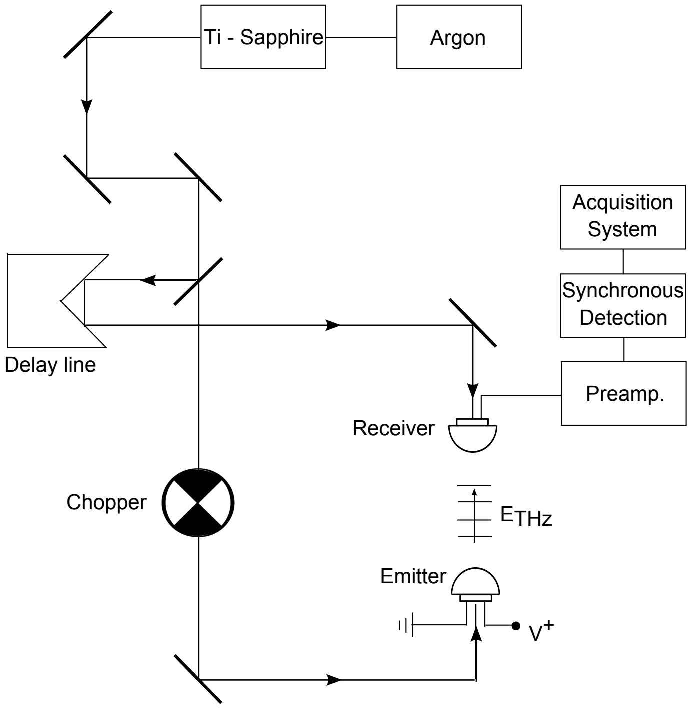


Fig. 4.23: Schematic of the THz-TDS apparatus used to perform the transmission measurements.

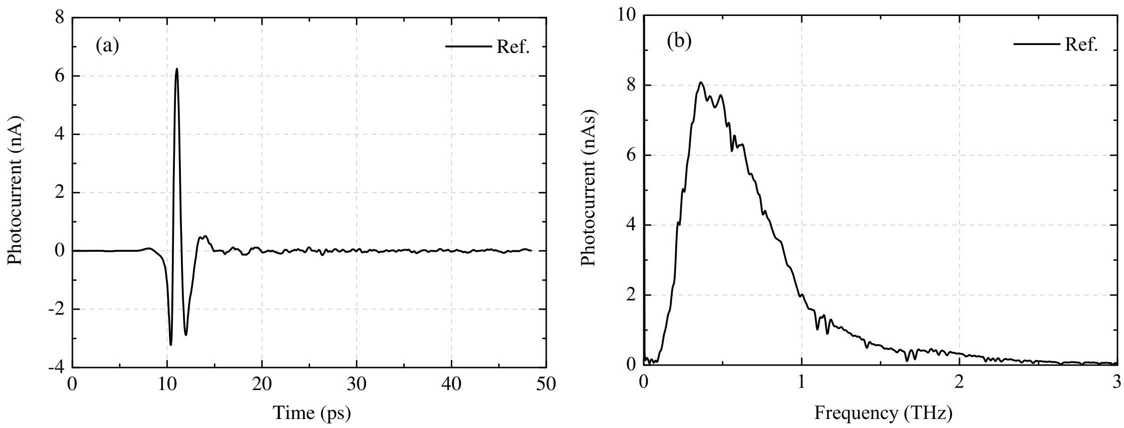


Fig. 4.24: Reference photocurrent signal as a function of the time (a) and of the frequency (b) at the photoconductor detection stage obtained by using an iris with 7 mm of internal diameter.

dipolar magnets arranged periodically. Wigglers deflect laterally the electrons which generate as before radiation, but with different properties in terms of photon energy and intensity. The radiation coming out from the ring is then collected through a complex optic system (filters) in order to be ultimately used to probe the samples. The advantages of using a synchrotron source for probing at THz frequencies are that the spectrum covered can be extremely broad (from a few hundreds GHz to nearly one hundred THz) and that the intensity of the source is well higher. As an example the available intensity at 3 THz is $5{\cdot}10^{13}$ photons/(s·0.1%BW) for the line AILES where 0.1%BW at 3 THz means that the flux is measured over 3 GHz at a central frequency of 3 THz, corresponding to a power of 80 nW in a bandwidth of 3 GHz around 3 THz than all other compact sources which are available and have been presented in the first chapter. The transmittance is obtained using a Fourier transform spectrometer from the ratio between the power measured by a bolometer cooled down at 4.2 K with and without the sample.

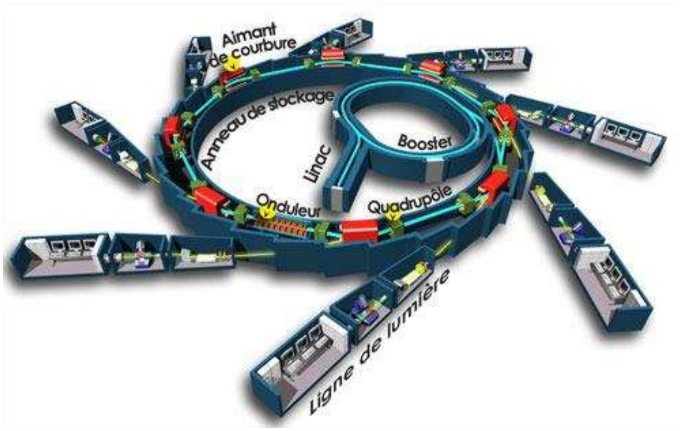


Fig. 4.25: View of the synchrotron Soleil with its different lines and related bending magnets to extract the radiation employed in the connected laboratories, from Ref. [35].

### 4.2.6 Measurements and analysis

Measurements by THz-TDS and by synchrotron light are presented over two different decades (0.25 - 2.5 THz) and (1 - 10 THz), respectively and compared with simulation results. The double-layer filter has been measured only by THz-TDS. The measurements by THz-TDS have been performed by Dr. Frédéric Garet and Ph.D student Mohan-Babu Kuppam, while the measurements by synchrotron light have been performed by Dr. Pascale Roy, director of the line AILES at Synchrotron Soleil.

#### 4.2.6.1 THz time-domain spectroscopy results

In Fig. 4.26 are reported the transmittance spectra recorded by THz-TDS of the fabricated and/or calculated mesh filters. The calculations in this frequency range agree pretty well with the experimental results. In particular Fig. 4.26(a) illustrates the importance of achieving small mesh widths to reduce as much as possible the reflection with a fixed period. A transmittance higher than 75% is achieved over 1 THz of bandwidth above 1.5 THz. The measured rejection ratio of 13 dB/decade for $w = 0.5$ $\mu$m can be improved further as reported in Fig. 4.26(b) which show a comparison between a single layer, a double layer and a triple-layer (only simulations) filter. The rejection ratio increases to 15 dB/decade for a double-layer filter

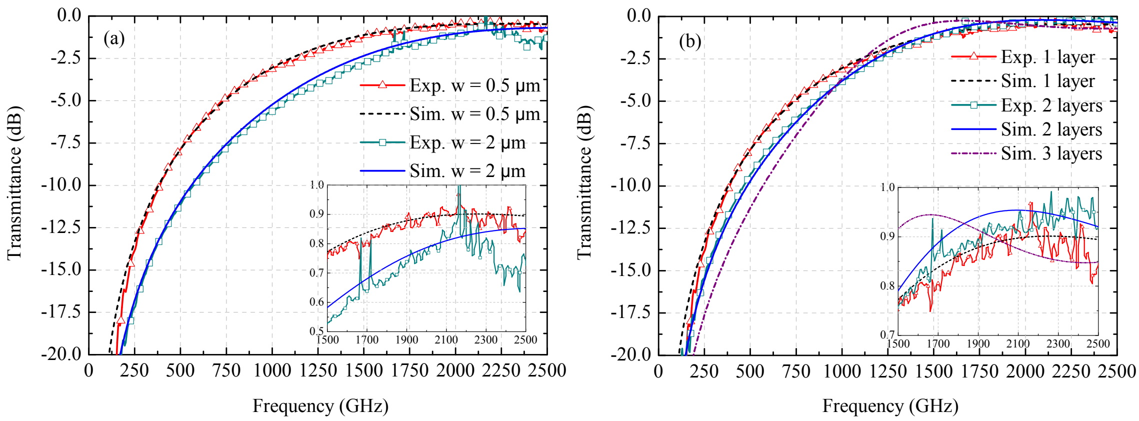


Fig. 4.26: Transmittance spectra of the fabricated filters in the range 0.25-2.5 THz. (a) illustrates the critical role of the mesh width $w$ in achieving high transmittance values in the pass-band for a constant period and (b) illustrates that a multi-layered filter can increase the rejection ratio in the stop-band, while still providing a high transmittance above 1.5 THz.

and to 17 dB/decade for a triple-layer one. Moreover, by increasing the thickness of the dielectric spacer ($t_{COC2/3}$) the rejection ratio can be increased further. It is worth to notice that the transparency is well-maintained above 1.5 THz thanks also to the constructive interference within the substrate. If the rejection ratio is the main objective of the filter requirements, a thicker mesh or thicker dielectric spacers are necessary to be used in order to avoid cascading several elements [25].



 

#### 4.2.6.2 Synchrotron light results

In Fig. 4.27 are reported the measured (a) and calculated (b) linear transmittance spectra with reference to Fig. 4.26(a) (single-layer filters). Several aspects need to be noticed here. First, the transmittance is higher than 75% not only over 1 THz, but over 5 THz of bandwidth as expected from calculations (see Fig. 4.13(a)). This result has been possible thanks to the design, in particular the sub-wavelength apertures, and to the high transparency of the substrate. Secondly a strong minimum is observed in both cases of Fig. 4.27(a). This minimum is likely to be associated to that one reported in Fig. 4.27(b). In fact, not only the spectral location is close (200-300 GHz of difference), but it red-shifts according to a reduction of the mesh width in agreement with the calculations. The difference in the measured and calculated minimum at higher frequencies may be attributed to fabrication tolerances, particularly regarding the thickness homogeneity and the flatness of the dielectric film. A second minimum is also present at lower frequencies, at $\nu = 6.27$ and 6.38 THz for $w = 0.5$ and 2 $\mu$m, respectively. Such a minimum has been already observed in previous simulations (see Fig. 4.13), but for different parameters. However, the simulation does not show it clearly, even though it appears clearer increasing the thickness or the mesh width as already discussed in the design section at almost the correct frequency. This issue may be thus related to a question of discretization of the structure. Even by strongly refining the mesh and changing other parameters or models (like Drude model for the metal), it has not been possible to correctly describe this resonance at lower frequency for the design parameters. However, in the framework of the interest of a high-transparency broadband filter, this problem has a secondary importance and no further investigation has been carried on.

Another interesting aspect regards the peak transmittance value. In fact, by considering that the surface covered by the metal in the case of $w = 2$ $\mu$m is 10%, it can be observed that actually, close to the diffraction, the transmittance is 94% thus achieving a value higher than the unity once normalized to the unit cell. This is the ET phenomenon which has been already widely introduced in the second chapter and which appears close to the diffraction as expected. For $w = 2$ $\mu$m, the enhancement factor is 1.044 (0.94/0.90) which is quite low due to the large apertures compared to the period.



 

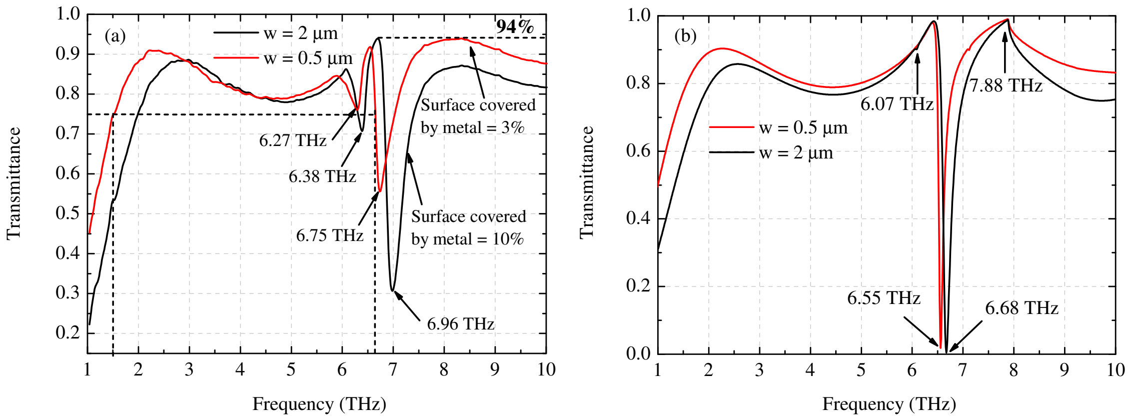


Fig. 4.27: Synchrotron Soleil measurements (a) and calculations (b) in the 1-10 THz range.

## 4.3 Conclusions

In conclusion, it has been shown that COC is a potential candidate for the next generation of free-space devices based on low-loss dielectric materials. In particular, a processing technique based on e-beam lithography has been demonstrated starting from films obtained by spin-coating of a commercial resist. The process permits to achieve sub-$\mu$m pattern definitions and to fabricate 2.5D structures with multiple layers. Moreover, the low quantities required of Au (52 $\mu$g for a single-layer filter with $w$ = 500 nm) and of COC (4 mg for a 13-$\mu$m-thick layer) used in the process, associated to the possibility of using deep-UV lithography, lead to a potential cost effective fabrication. The experimental results are in agreement with the calculations over a broad range of frequencies, in particular it has been observed the ET phenomenon at THz frequencies in the case of a single-layer mesh. The developed process can be applied to a wide variety of structures, even with higher complexity due to the possibility of cascading multiple COC layers regardless the increasing thickness due to the excellent properties of COC as low-loss dielectric.



 

# Bibliography

[1] G. Khanarian and H. Celanese, *Optical properties of cyclic olefin copolymers*, Opt. Eng. **40**, 1024 (2001)

[2] K. Nielsen, H. K. Rasmussen, A. J. L. Adam, P. C. M. Planken, O. Bang, and P. U. Jepsen, *Bendable, low-loss Topas fibers for the terahertz frequency range*, Opt. Exp. **17**, 8592 (2009)

[3] P. D. Cunningham, N. N. Valdes, F. A. Vallejo, L. M. Hayden, B. Polishak, X.-H. Zhou, J. Luo, A. K.-Y. Jen, and J. C. Williams, Robert J. Twieg, *Broadband terahertz characterization of the refractive index and absorption of some important polymeric and organic electro-optic materials*, J. Appl. Phys. **109**, 043505 (2011)

[4] E. Perret, N. Zerounian, S. David, and F. Aniel, *Complex permittivity characterization of benzocyclobutene for terahertz applications*, Microelectron. Eng. **85**, 2276 (2008)

[5] E. Peytavit, C. Donche, S. Lepilliet, G. Ducournau, and J.-F. Lampin, *Thin-film transmission lines using cyclic olefin copolymer for millimetre-wave and terahertz integrated circuits*, Electr. Lett. **47**, 453 (2011)

[6] S. Bothra, M. Kellam, and P. Garrou, *Feasibility of BCB as an interlevel dielectric in integrated circuits*, J. Electron. Mater. **23**, 819 (1994)

[7] Y.-S. Jin, G.-J. Kim, and S.-G. Jeon, *Terahertz dielectric properties of polymer*, J. Korean Phys. Soc. **49**, 513 (2006)

[8] M. Navarro-Cia, S. A. Kuznetsov, M. Aznabet, M. Beruete, F. Falcone, and M. S. Ayza, *Route for bulk millimeter wave and terahertz metamaterial design*, IEEE J. Quantum Electron. **47**, 375 (2011)

[9] W. L. Perry, K. M. Chi, T. Koda, M. Hampden-Smith, and R. Rye, *Direct depostion of patterned copper films on Teflon*, Appl. Surf. Sci. **69**, 94 (1993)

[10] www.topas.com

[11] K. Nielsen, H. K. Rasmussen, P. U. Jepsen, and O. Bang, *Broadband terahertz fiber directional coupler*, Opt. Lett. **35**, 2879 (2010)

[12] L. P. Johnson, W. Yuan, A. Stefani, K. NIelsen, H. K. Rasmussen, L. Khan, D. J. Webb, K. Kalli, and O. Bang, *Optical fibre Bragg grating recorded in TOPAS cyclic olefin copolymer*, Electr. Lett. **47**, 271 (2011)

[13] E. Peytavit, J.-F. Lampin, F. Hindle, C. Yang, G. Mouret, *Wide-band continuous-wave terahertz source with a vertically integrated photomixer*, Appl. Phys. Lett. **95**, 161102 (2009)

[14] S. M. Duffy, S. Verghese, K. A. McIntosh, A. Jackson, A. C. Gossard, and S. Matsuura, *Accurate modeling of dual dipole and slot elements used with photomixers for coherent terahertz output power*, IEEE Trans. Microwave Theory Techniques **49**, 1032 (2001)

[15] T. Ishibashi, Y. Muramoto, T. Yoshimatsu, and H. Ito, *Continuous THz wave generation by photodiodes up to 2.5 THz*, in *Proc. 37th International Conference on Millimeter and Terahertz Waves, 2013 (IRMMW-THz 2013) - to be published* (2013)

[16] D. Morozov, P. D. Mauskopf, P. Ade, M. Ridder, P. Khosropanah, M. Bruijn, J. van der Kuur, H. Hoevers, J.-R. Gao, and D. Griffin, *Ultrasensitive TES Bolometers for Space-Based FIR Astronomy*, IEEE Trans. Appl. Supercond. **21**, 188 (2011)

[17] E. Heinz, T. May, D. Born, G. Zieger, K. Peiselt, A. Brömel, S. Anders, V. Zakosarenko, T. Krause, A. Krüger, M. Schulz, and Hans-Georg Meyer, *Development of passive submillimeter-wave video imaging systems*, in *Proc. SPIE 8715, Passive and Active Millimeter-Wave Imaging XVI* (2012)

[18] F. Sizov and A. Rogalski, *THz detectors*, Progress In Quantum Electronics **34**, 278 (2010)

[19] M. Ravaro, V. Jagtap, G. Santarelli, C. Sirtori, L. H. Li, S. P. Khanna, E. H. Linfield, and S. Barbieri, *Continuous-wave coherent imaging with terahertz quantum cascade lasers using electro-optic harmonic sampling*, Appl. Phys. Lett. **102**, 091107 (2013)

[20] www.mtinstruments.com

[21] Jon Eyvindur Bjarnason, *Terahertz photomixing spectrometer technology*, Ph. D Dissertation - University of California - Santa Barbara (2007)

[22] H. Eisele, M. Naftaly, and John R Fletcher, *A simple interferometer for the characterization of sources at terahertz frequencies*, Meas. Sci. Technol. **18**, 2623 (2007)

[23] www.gentec-eo.com/products/thz-detectors/THZ B

[24] R. Ulrich, *Far-infrared properties of metallic mesh and its complementary structure and its complementary structure*, Infrared Phys. **7**, 37 (1967)

[25] S. Gupta, G. Tuttle, M. Sigalas, and K.-M. Ho, *Infrared filters using metallic photonic band gap structures on flexible substrates*, Appl. Phys. Lett. **71**, 2412 (1997)

[26] S. Yoshida, E. Kato, K. Suizu, Y. Nakagomi, Y. Ogawa, and K. Kawase, *Terahertz sensing of thin poly(ethylene terephthalate) film thickness using a metallic mesh*, Appl. Phys. Express **2**, 012301 (2009)

[27] www.cst.com

[28] F. J. Garcia-Vidal, M. Moreno, T. W. Ebbesen, and L. Kuipers, *Light passing through sub-wavelength apertures*, Rev. Mod. Phys. **82**, 729 (2010)

[29] A. Lüker, O. Sternberg, H. Hein, J. Schulz, K. D. Möller, *Thick capacitive meshes on polyimide substrates*, Infrared Phys. Techn. **45**, 153 (2004)

[30] Neil W. Ashcroft and David N. Mermin, *Solid state physics* (Harcourt college publishers, 1976)

[31] A. R. Djordjevi¸ R. M. Bilji¸ V. D. Likar-Smiljani¸ and T. K. Sarkar, *Wideband frequency-domain characterization of FR-4 and time-domain causality*, IEEE Trans. Electromagn. Compat. **43**, 662 (2001)

[32] S. Preu, *Tunable and continuous-wave Terahertz photomixer sources and applications*, J. Appl. Phys. **109**, 061301 (2011)

[33] J.-B. Brubacha, L. Mancerona, M. Rouzièresa, O. Piralia, D. Balcona, F. K. Tchanaa, V. Boudone, M. Tudorief, T. Huetf, A. Cuisset, and P. Roy, *Performance of the AILES THz-infrared beamline at SOLEIL for High resolution spectroscopy*, in *AIP Conf. Proc. 1214, 81* (2010)

[34] John D. Jackson, *Classical electrodynamics* (Third Edition - Wiley, New Jersey, 1998)

[35] www.synchrotron soleil.fr

# Final conclusions and perspectives

In this work it has been shown that sub-wavelength apertures can be efficiently employed in active and passive devices for THz waves generation and detection. This has been demonstrated by the design, fabrication and characterization of UTC-PDs and metal mesh filters.

In the case of UTC-PDs the top-contact, constituted of an array of slits, has led for a front-side illumination to several advantages compared to previous works. From an electrical point of view, the designed contact has demonstrated good properties due to its large thickness (300 nm), compared to typically used semi-transparent windows (10-20 nm), which leads to a low series resistance and to the thin Pt layer which provides a low specific contact resistance. Such a contact (for the best geometry) has been shown by finite element simulations and by experimental comparison with different geometries to be highly transparent leading to responsivities as high as 75 mA/W. In terms of efficiencies these devices performed better than those fabricated in the previous thesis. This improvement is thought to be associated to the ease of illumination and to the interplay of ET, diffraction and SPPs absorption within the thicker (150 nm instead of 100 nm) absorbing region. Regarding thermal aspects, this contact is poorly optically absorbing (calculated less than 20%) and permits to employ high optical powers and thus to achieve high RF powers. In particular, a 3-$\mu$m-side device has been able to generate an RF power of 400 $\mu$W with a DC photocurrent of 12.8 mA and an optical power of 200 mW at 300 GHz. This is the highest value ever reported by UTC-PDs with no impedance matching and it is quite close to the current state-of-the-art value of 1.2 mW for two coupled UTC-PDs with a matching circuit. Again these devices performed better in terms of RF power compared to the previous work mainly due to the thermal limitation associated to the strongly absorbing Ti/Pt/Au top-contact and to the higher efficiencies. The thermal management can be improved even further thanks to the possibility of placing a heat sink or a cooler like a Peltier element underneath the substrate due to removal of the optical transparent window for back-side illumination. Moreover, this contact design may find application in future resonant structures (under fabrication) due to the possibility of having a Fabry-Pérot cavity within the epitaxial layer to increase the optical absorption. Further studies need to be performed to understand better the role of the thermal heating and how to reduce it by using coolers or heat dissipation elements integrated on the device.



 

The fabrication of these devices is simpler compared to back-side illuminated ones. In fact, even though the top-contact design is more complex than in the previous thesis, the possibility of exploiting e-beam lithography and the fabrication tolerances chosen in the design, make this step relatively easy. On the contrary, no further post-processing of the substrate like polishing, cleaving or deposition of an antireflective coating is required. Moreover, the future integration of standard planar antennas (with a hyperhemispherical Si lens) does not present any problem, differently from back-side configurations for which a process was developed in the previous thesis to monolithically integrate a 3D TEM horn antenna without using a silicon lens.

In terms of characterization, this configuration is much simpler with respect to back or edge-side ones, in particular for "on-wafer" measurements. In fact, within this approach it is possible to test several topologies of top-contacts, accesses, resonant circuits etc. on a single wafer to find the best suited for a certain application. The second practical advantage is related to the possibility of observing at the same time the device, the probe and the fiber, reducing considerably the time spent during the characterization for alignment issues. The next on-going step is to integrate the developed contact with resonant structures to increase further the efficiency, while achieving the same response speed.

In the case of metal mesh filters, sub-wavelength apertures have been adopted since their development in the 60's. However, at THz frequencies several aspects have to be taken into account. The robust process developed in this work by using a highly transparent dielectric (COC) thin film over the entire THz region with several properties suitable for microelectronic processing techniques has led to the realization of high-pass filters with cut-off frequencies (-3 dB) at 1 THz and optimal characteristics in terms of transparency and broadband behavior (transmittance higher than 75% over 5 THz of bandwidth). This type of device can be integrated in RT detectors for free-space THz applications where UTC-PDs are the active elements to filter out the background noise coming from the beating of all the frequency components of the ASE spectrum which are down-converted in UTC-PDs. This issue is particularly critical at higher frequencies due to the low efficiencies of UTC-PDs above 1-1.5 THz. A future step consists in using thicker metal meshes to obtain higher rejection ratios, while still providing good transparency and broadband properties above 1 THz.



 

The demonstrated capability of cascading multiple layers and of achieving high pattern definition (mesh width down to 500 nm) over a thin flexible polymer paves the way for future more complex structures working at THz frequencies like metamaterials or photonic band gap structures which have responses strongly depending on the absorption coefficient of the dielectric materials involved at these frequencies.

# Publications related to the manuscript

F. Pavanello, G. Ducournau, M. Zaknoune, E. Peytavit, M. Vanwolleghem, C. Coinon, X. Wallart, and J.-F Lampin, "*Uni-travelling carrier photodiodes based on sub-wavelength apertures for higher efficiencies*", *Opt. Exp.*, in preparation.

F. Pavanello, F. Garet, M.-B. Kuppam, E. Peytavit, M. Vanwolleghem, F. Vaurette, J.-L. Coutaz, and J.-F. Lampin, "*Broadband ultra-low-loss mesh filters on flexible cyclic olefin copolymer films for THz applications*", *Appl. Phys. Lett.*, **102**, 111114 (2013).

F. Pavanello, M.-B. Kuppam, F. Garet, E. Peytavit, M. Vanwolleghem, F. Vaurette, J.-L. Coutaz, and J.-F. Lampin, "*High-transparency metal mesh filters based on cyclic olefin copolymer films for broadband THz applications*", *38th International Conference On Infrared, Millimiter and THz Waves, IRMMW-THz 2013, Mainz, Germany* (2013) - Oral presentation.

# Other publications

F. Pavanello, G. Ducournau, E. Peytavit, S. Lepilliet and J.-F. Lampin, "*High-gain Yagi-Uda antenna on cyclic olefin copolymer membrane for 300 GHz applications*", *IEEE Ant. Wirel. Propag. Lett.*, **13**, 939 (2014).

G. Ducournau, D. Bacquet, P. Szriftgiser, F. Pavanello, E. Peytavit, M. Zaknoune, A. Beck, and J.-F. Lampin, "*Cascaded Brillouin fibre lasers coupled to unitravelling carrier photodiodes for narrow linewidth terahertz generation*", *Electron. Lett.* **50**, 690 (2014).

G. Ducournau, F. Pavanello, L. Tohme, S. Blin, P. Nouvel, E. Peytavit, M. Zaknoune, P. Szriftgiser, and J.-F. Lampin, "*High-definition television transmission at 600 GHz combining THz photonics hotspot and high-sensitivity heterodyne receiver*", *Electron. Lett.* **50**, 413 (2014).

E. Peytavit, F. Pavanello, G. Ducournau, and J-F. Lampin, "*Highly efficient Terahertz detection by optical mixing in a GaAs photoconductor*", *Appl. Phys. Lett.*



 

**103**, 201107 (2013).

G. Ducournau, P. Szriftgiser, F. Pavanello, P. Latzel, A. Beck, T. Akalin, E. Peytavit, M. Zaknoune, D. Bacquet, and J.-F. Lampin, "*22 Gbps wireless communication system at 0.4 THz*", *38th International Conference On Infrared, Millimiter and THz Waves, IRMMW-THz 2013, Mainz, Germany* (2013) - Invited.

E. Peytavit, P. Latzel, F. Pavanello, G. Ducournau, and J.-F. Lampin, "*Milliwatt output power generated in the J-Band by a GaAs photomixer*", *38th International Conference On Infrared, Millimiter and THz Waves, IRMMW-THz 2013, Mainz, Germany* (2013) - Invited.

E. Peytavit, P. Latzel, F. Pavanello, G. Ducournau, and J.-F Lampin, "*CW source based on photomixing with output power reaching 1.8 mW at 250 GHz*", *IEEE Electron. Dev. Lett.*, accepted.

F. Pavanello and S. Giordano, "*How imperfect interfaces affect the nonlinear transport properties in composite nanomaterials*", *J. Appl. Phys.*, **113**, 154310 (2013).

F. Pavanello, F. Manca, P.L. Palla, and S. Giordano, "*Generalized interface models for transport phenomena: Unusual scale effects in composite nanomaterials*", *J. Appl. Phys.*, **112**, 084306 (2012).

A. Rolland, G. Ducournau, G. Loas, A. Beck, F. Pavanello, E. Peytavit, T. Akalin, M. Zaknoune, J.-F. Lampin, M. Brunel, F. Bondu, M. Vallet, and M. Alouini, "*Narrow linewidth tunable THz signal radiated by 1.55μm photomixing*", *Proc. SPIE 8496, Terahertz Emitters, Receivers and Applications III, San Diego, CA, United States* (2012).

J. Borner, G. Pillet, L. Morvan, D. Dolfi, A. Beck, P. Latzel, F. Pavanello, G. Ducournau, and J.-F. Lampin,"*Stability of signals generated with a dual-frequency laser and a UTC photodiode up to 700 GHz*", *37th International Conference On Infrared, Millimiter and THz Waves, IRMMW-THz 2012, Wollongong, NSW, Australia* (2012).



 

G. Ducournau, A. Rolland, G. Loas, A. Beck, F. Pavanello, E. Peytavit, T. Akalin, M. Zaknoune, J.-F. Lampin, M. Brunel, F. Bondu, M. Vallet, and M. Alouini, "*Narrow linewidth tunable THz signal generation using a unitravelling carrier photodiode and a dual-mode laser*", *37th International Conference On Infrared, Millimiter and THz Waves, IRMMW-THz 2012, Wollongong, NSW, Australia* (2012).

F. Pavanello, I. Turer, T. Akalin, S. Vandenbrouck, E. Peytavit, and J.-F. Lampin, "*Broadband waveguide-to-microstrip transition in W band*", *36th International Conference On Infrared, Millimiter and THz Waves, IRMMW-THz 2011, Houston, TX, United States* (2011) - Oral presentation.